

---

Electronic Thesis and Dissertation Repository

---

10-28-2021 1:45 PM

## Significance of the vehicle front design and gait postures on traumatic brain injuries sustained by different pedestrian populations during car-to-pedestrian collisions (CPCs) - A computational approach

Thava Kalishwara Kumar Gunasekaran, *The University of Western Ontario*

Supervisor: Mao Haojie, *The University of Western Ontario*

A thesis submitted in partial fulfillment of the requirements for the Master of Engineering Science degree in Mechanical and Materials Engineering

© Thava Kalishwara Kumar Gunasekaran 2021

Follow this and additional works at: <https://ir.lib.uwo.ca/etd>



Part of the [Automotive Engineering Commons](#), [Biomechanical Engineering Commons](#), [Computer-Aided Engineering and Design Commons](#), and the [Engineering Mechanics Commons](#)

---

### Recommended Citation

Gunasekaran, Thava Kalishwara Kumar, "Significance of the vehicle front design and gait postures on traumatic brain injuries sustained by different pedestrian populations during car-to-pedestrian collisions (CPCs) - A computational approach" (2021). *Electronic Thesis and Dissertation Repository*. 8218. <https://ir.lib.uwo.ca/etd/8218>

This Dissertation/Thesis is brought to you for free and open access by Scholarship@Western. It has been accepted for inclusion in Electronic Thesis and Dissertation Repository by an authorized administrator of Scholarship@Western. For more information, please contact [wlsadmin@uwo.ca](mailto:wlsadmin@uwo.ca).

# Abstract

With the increasing prevalence of traumatic brain injuries (TBIs) in road traffic accidents (RTAs), it was identified that the shape of the vehicle's front end and pedestrian postures prior to impact significantly influence pedestrian head injuries. However, the effect of vehicle front shape parameters and gait postures on TBIs sustained in car-to-pedestrian collisions (CPCs) has yet to be quantified. This study used a computational approach to analyze the effect of vehicle shape parameters and pedestrian gait postures on pedestrian TBI risks across a diverse pedestrian population with varying body sizes. Our findings indicate that vehicle shape parameter such as BLEH (Bonnet leading edge height), BA (Bonnet angle), and WA (Windshield angle) were statistically significant predictors of pedestrians' TBI risk. Increasing BLEH in sedans and decreasing BLEH in high-leading-edged vehicles reduce the risk of TBIs. Vehicles with high BLEH and low BA were susceptible to AIS (Abbreviated injury scale) 4+ head injuries. In vehicles with a low BLEH, pedestrian height and mass were statistically significant factors affecting pedestrian head rotation. Our results demonstrate that TBI risks were found to be different for gait percentage in the same and different gait types. Walking and emergency gaits dominate linear head kinematics, whereas running gaits dominate head rotation in pedestrians, resulting in substantial brain strain. Linear head kinematics varies significantly between the stance and swing phases of walking and running gait postures, whereas rotational head kinematics and brain strains vary cyclically but to a less extent.

## Keywords

Traumatic brain injuries (TBI), Car-to-pedestrian collisions (CPCs), Bonnet leading edge height (BLEH), bonnet angle (BA), Windshield angle (WA), brain strain, head kinematics, mild TBI

## Summary for Lay Audience

In recent years technological advancements in seat belts and airbags have increased the survivability of vehicle occupants in road traffic accidents (RTAs). In contrast, pedestrians are still vulnerable to severe and fatal injuries in RTAs. Head injuries are leading causes of death and long-term disability. With different types of passenger cars and light trucks on the road, it was determined that the front shape of the car and pedestrian posture prior to the impact significantly influence pedestrian head injury risk. Numerous automakers attempted to optimize the vehicle front shape with soft and less stiff structures. As a result, several head injuries such as skull fracture and focal brain injuries were reduced, but the risk of diffuse brain injuries have become more common and has never been studied due to methodological constraints.

We adopted two novel computational approaches to investigate the impact of vehicle front shapes and pedestrian gait posture on pedestrian TBI risk using a full-scale FE pedestrian model. Our findings show that vehicle bonnet leading edge height (BLEH) has a significant impact on mild TBIs and that vehicles with higher BLEH, such as sports utility vehicles (SUVs) and pickup trucks, are more likely to cause severe head injuries. In addition, BLEH indirectly affects the pedestrian head rotation among different populations. Our findings also revealed that the risk of TBI varies depending on pedestrian pre-impact gait postures. These findings provide a basis for future vehicle design safety for pedestrian injury protection

## Co-Authorship Statement

Chapter 02 (Investigating the influence of vehicle front shapes and pedestrian body size on traumatic brain injuries sustained in car-to-pedestrian collisions using the pedestrian finite element model) was co-authored by Dr Haojie Mao

Chapter 03 (Investigating pedestrian gait postures' influence on dynamic head and intracranial strain response of average 50th percentile males in car-to-pedestrian collisions) was co-authored by Dr Haojie Mao

All manuscripts were drafted by Thava Kalishwara Kumar Gunasekaran and reviewed by Dr Haojie Mao.

## Acknowledgments

I would like to thank my supervisor Dr Haojie Mao for his continuous guidance and support. I thank my advisory committee member Dr Mike Shkrum for his help. I acknowledge Kewei Bian for his assistance with computational modelling.

# Table of Contents

Abstract.....	ii
Summary for Lay Audience.....	iii
Co-Authorship Statement.....	iv
Acknowledgments.....	v
Table of Contents.....	vi
List of Tables.....	x
List of Figures.....	xi
List of Acronyms.....	xvii
Chapter 1.....	1
1 Introduction.....	1
1.1 Brief Research Rationale.....	1
1.2 Anatomy of head and brain.....	1
1.2.1 Skull anatomy.....	1
1.2.2 Brain anatomy.....	2
1.3 Characteristic of pedestrian head injuries in RTAs.....	3
1.4 Computational Human body model (HBM).....	6
1.5 Review of head injury criteria.....	7
1.6 Research outline.....	12
Chapter 2.....	14
2 Investigating the influence of vehicle front shapes and pedestrian body size on traumatic brain injuries sustained in car-to-pedestrian collisions using the pedestrian finite element model.....	14
2.1 Abstract.....	14
2.2 Introduction.....	15
2.3 Methods.....	18

2.3.1	Simulation models .....	18
2.3.2	Development of simplified FE vehicle model .....	21
2.3.3	Validation of simplified FE vehicle model.....	22
2.3.4	Validation of pedestrian head kinematics in CPC .....	25
2.4	Accident reconstruction .....	28
2.5	Results.....	30
2.5.1	Pedestrian Kinematics.....	30
2.5.2	Linear head kinematics .....	34
2.5.3	Rotational head kinematics .....	35
2.5.4	Intracranial strain response of brain tissue.....	38
2.5.5	Correlation between head kinematics and brain strains.....	41
2.5.6	Influence of skull fracture on intracranial strain response of brain tissue	44
2.5.7	Influence of vehicle front shape parameters on intracranial strain response of brain tissue .....	49
2.5.8	Influence of pedestrian body size on head kinematic .....	54
2.6	Discussion.....	56
2.6.1	The effect of vehicle shape parameters, pedestrian height, and weight on pedestrian head rotation and diffuse brain injuries .....	56
2.6.2	The effect of bonnet leading-edge height and bonnet angle on the severity of AIS 4+ head injuries .....	58
2.6.3	Injury severity between SUV and pickup trucks .....	59
2.6.4	Influence of skull fracture on the intracranial strain response of brain tissue .....	61
2.7	Conclusion .....	61
Chapter 3.....		62
3	Investigating pedestrian gait postures' influence on dynamic head and intracranial strain response of average 50th percentile males in car-to-pedestrian collisions (CPCs). .....	62
3.1	Abstract.....	62

3.2	Introduction.....	63
3.3	Methods.....	64
3.3.1	Pedestrian Dummy Finite element model.....	64
3.3.2	Anthropometry of Hybrid III .....	66
3.3.3	Scaling of Hybrid III.....	69
3.3.4	Validation of Scaled Hybrid III pedestrian Dummy.....	74
3.3.5	Development of simplified FE vehicle model .....	78
3.3.6	Validation of simplified FE vehicle model.....	79
3.3.7	Validation of pedestrian head kinematics in CPC .....	80
3.4	Accident Reconstruction.....	82
3.5	Results.....	86
3.5.1	Validation results of head drop test and whole-body kinematics .....	86
3.5.2	Effect of walking, running, emergency gait and posture on the head kinematics and intracranial strain response .....	91
3.5.3	Correlation between head kinematics and brain strains.....	92
3.5.4	Effect of gait percentage on the head kinematics and intracranial strain response.....	94
3.6	Discussion.....	97
3.6.1	Scaling and validation of Hybrid III standing FE dummy for pedestrian pre-impact posture study.....	97
3.6.2	Effect of pedestrian gaits and posture on head and brain response. ....	98
3.7	Conclusion .....	99
	Chapter 4.....	100
4	Conclusion and Future Work .....	100
4.1	Brief Overview.....	100
4.2	Summary .....	100
4.2.1	Effect of vehicle front shape parameters .....	100



4.2.2	Effect of pedestrian pre-impact gait postures .....	100
4.3	Limitations .....	101
4.4	Future work, Novelty, and Significance .....	102
4.4.1	Future work.....	102
4.4.2	Novelty and Significance.....	103
	References.....	104
	Curriculum Vitae .....	116

## List of Tables

Table 1-1 The Abbreviated Injury Scale (AIS) [49, 50] .....	12
Table 2-1 Body mass, stance, and center of gravity (C.G) from the ground of all pedestrian FE model .....	19
Table 2-2 Vehicle front shape parameters measured from all vehicle model.....	21
Table 2-3 Injury threshold values used for head injury criteria.....	29
Table 2-4 Pearson and Spearman correlation analysis between head kinematics and brain strains (N= 48) .....	42
Table 2-5 Pearson and Spearman correlation analysis between vehicle shape parameters and MPS95, MPSmean, CSDM15, CSDM25 A) Male AM50 (N =12) B) Male AM95 (N =12) C) Female AF05 (N =12) A) Child 6YO (N =12) .....	50
Table 3-1 Body mass, stance, and center of gravity (C.G) from the ground of all pedestrian FE model .....	65
Table 3-2 Percentage difference of anthropometric measurements between Hybrid III and ANSUR I & II data. ....	68
Table 3-3 Age, mass and pre-test stature of PMHS test specimen .....	75
Table 3-4 Percentage difference in geometric measurement between the FE test vehicle and PMHS test vehicle.....	76
Table 3-5 Head injury criteria considered in the study.....	85

# List of Figures

Figure 1-1 Anatomy of the skull (Adapted from Wikimedia Commons)..... 2

Figure 1-2 Anatomy of human brain (Adapted from Wikimedia Commons) ..... 3

Figure 1-3 U.S pedestrian fatality rate from 2016 to 2020 based on Governors Highway Safety Association (GHSA)..... 5

Figure 1-4 Annual distribution of all head injuries and TBIs associated with pedestrian from RTA, eCHIRPP (2011-2017)..... 5

Figure 1-5 THUMS (The Total Human Model for Safety) ..... 6

Figure 1-6 The Wayne State Tolerance Curve (WSTC)..... 7

Figure 2-1 A) Child 6YO B) Small Female 5<sup>th</sup> percentile AF05 C) Average Male 50<sup>th</sup> percentile AM50 D) Large Male 95<sup>th</sup> percentile AM95 ..... 19

Figure 2-2 A) Toyota Yaris 2010 B) Toyota Camry 2012 C) Ford Explorer 2002 D) Chevrolet Silverado 2014 ..... 20

Figure 2-3 Vehicle front shape parameter measurements..... 21

Figure 2-4 Simplified vehicle FE model A) Toyota Yaris – Subcompact passenger sedan B) Toyota Camry – Mid-size sedan C) Ford Explorer – Sports Utility Vehicle (SUV) D) Chevrolet Silverado – Pickup truck ..... 22

Figure 2-5 Global deformation pattern of full-frontal crash test a) Toyota Yaris b) Toyota Camry c) Ford Explorer d) Chevrolet – Silverado..... 23

Figure 2-6 a) Yaris engine top X acceleration b) Yaris engine bottom X acceleration c) Camry engine top X acceleration d) Camry engine bottom X acceleration e) Explorer engine top X acceleration f) Explorer engine bottom X acceleration g) Silverado engine top resultant acceleration h) Silverado engine top resultant velocity. .... 24

Figure 2-7 Car-to-pedestrian collision NCAP configuration setup – Simplified car models were accelerated at 40 km/h and impacted the pedestrian FE model at the vehicle centerline (y-axis). A gravitational load of  $9.81\text{m/s}^2$  was applied to all nodes and a 6DOF accelerometer was defined at the CG of the pedestrian head. .... 26

Figure 2-8 Pedestrian kinematics of Average male 50<sup>th</sup> percentile in CPC (Mid-size sedan, 40 km/h) ..... 26

Figure 2-9 a) Yaris CPC head resultant acceleration b) Yaris CPC head resultant velocity c) Camry CPC head resultant acceleration d) Camry CPC head resultant velocity e) Explorer CPC head resultant acceleration f) Explorer CPC head resultant velocity g) Silverado CPC head resultant acceleration h) Silverado CPC head resultant velocity ..... 27

Figure 2-10 Accident reconstruction – three-step pipeline ..... 28

Figure 2-11 Pedestrian Kinematics (Compact sedan – Yaris, 40 km/h) ..... 31

Figure 2-12 Pedestrian Kinematics (Mid-sedan – Camry, 40 km/h) ..... 32

Figure 2-13 Pedestrian Kinematics (SUV – Explorer, 40 km/h) ..... 33

Figure 2-14 Pedestrian Kinematics (Pickup truck – Silverado, 40 km/h) ..... 34

Figure 2-15 a) Head Injury Criterion (HIC15) b) Peak linear acceleration ..... 35

Figure 2-16 a) Brain Injury Criteria (BrIC) b) Peak angular velocity c) Peak angular acceleration ..... 37

Figure 2-17 a) Maximum Principal Strain 95th percentile (MPS95) b) Average Maximum Principal Strain (MPSmean) c) Diffuse axonal multi-axis general evaluation (DAMAGE) . 39

Figure 2-18 Cumulative Strain Damage Measure (CSDM15) b) Cumulative Strain Damage Measure (CSDM25) ..... 40

Figure 2-19 Linear Regression analysis i) Peak angular velocity vs. MPSmean ii) Peak angular acceleration vs. MPSmean iii) DAMAGE vs. MPSmean iv) BrIC vs. MPSmean v) HIC15 vs. MPSmean ..... 43

Figure 2-20 Linear Regression analysis i) Peak angular velocity vs. CSDM25 ii) Peak angular acceleration vs. CSDM25 iii) DAMAGE vs. CSDM25 iv) BrIC vs. CSDM25 v) HIC 15 vs. CSDM25.....	44
Figure 2-21 Peak von mises skull stress .....	45
Figure 2-22 Linear regression analysis a) Skull stress vs MPS95 – AM50 b) Skull stress vs CSDM25 – AM50 c) Skull stress vs MPS95 – AF05 d) Skull stress vs CSDM25 – AF05 ...	46
Figure 2-23 Peak Von-Mises skull stress for female AF05 and child 6YO .....	47
Figure 2-24 Peak Von-Mises skull stress for male AM50 and AM95 .....	48
Figure 2-25 Linear regression analysis between vehicle shape parameters (BLEH, BA, and WA) and brain strain metrics (MPS95, MPSmean, CSDM15, and CSDM25) for males (AM50). .....	53
Figure 2-26 Linear regression analysis between vehicle shape parameter (BLEH, BA, and WA) and brain strain metrics (MPS95, MPSmean, CSDM15, and CSDM25) for males (AM 95).....	54
Figure 2-27 Linear regression analysis BrIC vs pedestrian height and mass – a) Subcompact passenger sedan b) Mid-size sedan c) Sports Utility Vehicle (SUV) d) Pickup truck .....	55
Figure 2-28 Distribution of MPS95 and CSDM 15 for windshield impacts a) MPS95 for male (AM50 and AM95) b) CSDM15 for male (AM50 and AM95) in sedans .....	56
Figure 2-29 Distribution of MPS95 and CSDM 15 for hood impacts a) MPS95 for male (AM50 and AM95) b) CSDM15 for male (AM50 and AM95) in SUV and pick trucks .....	57
Figure 2-30 A) Inner hood structure with hood adhesive pads in pickup truck B) Inner hood structure in SUV .....	60
Figure 2-31 A) 6YO collision with Pickup trucks – head-to-front-grill b) 6YO collision with SUVs– head-to-front-grill.....	60
Figure 3-1 Hybrid III – 50 <sup>th</sup> percentile male pedestrian dummy .....	65

Figure 3-2 Population distribution of stature from a) ANSUR I database b) ANSUR II database.....	66
Figure 3-3 Anthropometric measurements A) Cervical height B) Iliocristale height C) Vertical thumb tip reach down D) Knee height E) Buttock height F) Chest depth G) Head breadth H) Waist breadth I) Bideltoid breadth J) Stature .....	67
Figure 3-4 Comparison of the stature of the pedestrian dummies in the past literature .....	67
Figure 3-5 Comparison of body segment mass between different databases .....	69
Figure 3-6 Scaling of a rigid body with local coordinate parallel to the global coordinate ...	71
Figure 3-7 Scaling of a rigid body with local coordinate non-parallel to the global coordinate .....	73
Figure 3-8 Head drop test set up .....	74
Figure 3-9 Modified FE vehicle with reference to the test vehicle centerline contour dimension.....	76
Figure 3-10 Car to Pedestrian Collision – NCAP protocol used in PMHS test. The test vehicle was accelerated at 40 km/h to laterally hit the pedestrian at the vehicle centerline. A gravitational acceleration load of $9.81\text{m/s}^2$ was applied to all nodes. Nodal displacement trajectories of the head, T1 and pelvis were recorded. ....	77
Figure 3-11 Toyota Camry mid-size passenger sedan (Model year 2012).....	78
Figure 3-12 Simplified vehicle FE model.....	79
Figure 3-13 Global deformation pattern of the simplified FE model during the full-frontal crash test.....	79
Figure 3-14 a) Camry CPC head resultant acceleration b) Camry CPC head resultant velocity .....	80

Figure 3-15 Car-to-Pedestrian Collisions (CPCs) - Simplified mid-sedan car model was accelerated at 40 km/h and impacted the pedestrian FE model at the vehicle centerline (y-axis). A gravitational load of  $9.81\text{m/s}^2$  was applied to all nodes and a 6DOF accelerometer was defined at the CG of the pedestrian head. .... 81

Figure 3-16 Pedestrian kinematics of scaled HIII 50<sup>th</sup> percentile average male in CPC (Sedan, 40 km/h) ..... 81

Figure 3-17 a) Camry CPC – Peak Resultant head acceleration b) Camry CPC – Peak Resultant head angular velocity ..... 82

Figure 3-18 Accident reconstruction – Four-step pipeline ..... 82

Figure 3-19 Walking gaits ..... 83

Figure 3-20 Running gaits ..... 83

Figure 3-21 Emergency gaits ..... 83

Figure 3-22 Isolated THUMS FE head – Prescribed head only prescribed motion ..... 85

Figure 3-23 Resultant head acceleration comparison ..... 86

Figure 3-24 Dummy head, vertebra T1, and pelvis trajectories in CPC plotted in the test vehicle (YZ) coordinate system ..... 88

Figure 3-25 HIII Trajectories compared to PMHS 10% corridor a) Head Trajectory b) T1 Vertebra c) Pelvis Trajectory ..... 89

Figure 3-26 Kinematic trajectories of the head, vertebra T1 and pelvis with reference to the test vehicle front structure ..... 90

Figure 3-27 Pedestrian kinematics compared between the high-speed video images from PMHS test with tall, short, and medium statured specimens and HIII pedestrian simulation 90

Figure 3-28 a) HIC15 b) BrIC c) DAMAGE d) MPSmax e) MPSmean f) CSDM15 ..... 92

Figure 3-29 a) RPLA vs. MPSmax, MPSmean, and CSDM15 a) RPRV vs. MPSmax, MPSmean, and CSDM15 a) RPRA vs. MPSmax, MPSmean, and CSDM15 a) HIC15 vs. MPSmax, MPSmean, and CSDM15 a) BrIC vs. MPSmax, MPSmean, and CSDM15 a) DAMAGE vs. MPSmax, MPSmean, and CSDM15.....	93
Figure 3-30 Walking gaits a) HIC15 b)BrIC c)DAMAGE d)MPSmax e)MPSmean f) CSDM15 .....	95
Figure 3-31 Running gaits a) HIC15 b) BrIC c) DAMAGE d) MPSmax e) MPSmean f) CSDM15 .....	96
Figure 3-32 Emergency gaits a) HIC15 b) BrIC c) DAMAGE d) MPSmax e) MPSmean f) CSDM15 .....	97



## List of Acronyms

BA – Bonnet angle

BED – Bonnet end depth

BLEH – Bonnet leading edge height

BrIC – Brain Injury Criteria

CSDM – Cumulative strain damage measure

DAMAGE – Diffuse axonal multi-axis general evaluation

FE – Finite element

HBM – Human body model

HIC – Head injury criterion

MPS – Maximum principal strain

NCAP – New car assessment program

RTA – Road traffic accidents

SUV – Sports utility vehicle

TBI – Traumatic brain injury

THUMS – Total Human Model for Safety

WA – Windshield angle

# Chapter 1

## 1 Introduction

### 1.1 Brief Research Rationale

WHO (The World Health Organization) reported that nearly 1.35 million people die every year from road traffic accidents (RTAs) [1]. Traumatic brain injuries (TBIs) are the leading cause of death and prolonged disability in road traffic accidents (RTAs) [2-7]. According to eCHIRPP (The Electronic Canadian Hospitals Injury Reporting and Prevention Program) data from 2011 to 2017, TBI accounted for 67.1% of head injuries sustained in RTAs [8]. Accident data showed that vehicle front shape significantly influences pedestrian head injury risk during car-to-pedestrian collisions (CPCs) [9-11]. With softer front structure and better speed control systems in recent cars, Li et al. suggested that AIS 2+ head injuries such as mild TBI/concussion and diffuse axonal injury (DAI) would be the primary concern in the future vehicle safety design [12]. Past literature has created a gap in quantifying the influence of vehicle front shapes on pedestrian TBI risk across the diverse population with varying body sizes during CPCs. In addition, pre-impact pedestrian gait posture also significantly affects head kinematics and TBI outcomes [13-15]. However, prior research on the effect of pedestrian gait postures on pedestrian TBI risk in CPC-related impacts was lacking. This thesis quantitatively investigates the influence of vehicle front shape parameters and gait postures on TBIs sustained by diverse pedestrian populations during CPCs.

### 1.2 Anatomy of head and brain

#### 1.2.1 Skull anatomy

The skull is a bony structure composed of cranial bones that surrounds and protects the brain. The neuro-cranium, sutures, and facial skeleton are the three major parts of the human skull. The temporal bones, two parietal bones, one occipital bone, one sphenoid bone, one ethmoid bone, and one frontal bone make up the neuro-cranium. (Figure 1-1) The brain, meninges, and cerebral vasculature are all protected by the cranium. The facial skeleton, on the other hand, is made up of two zygomatic bones, two lacrimal bones, two

nasal bones, two inferior nasal conchae bones, two Palatine bones, two Maxilla bones, two Vomer bones, and one Mandible bone. Sutures are major fibrous joints that connect the bones of the cranium.

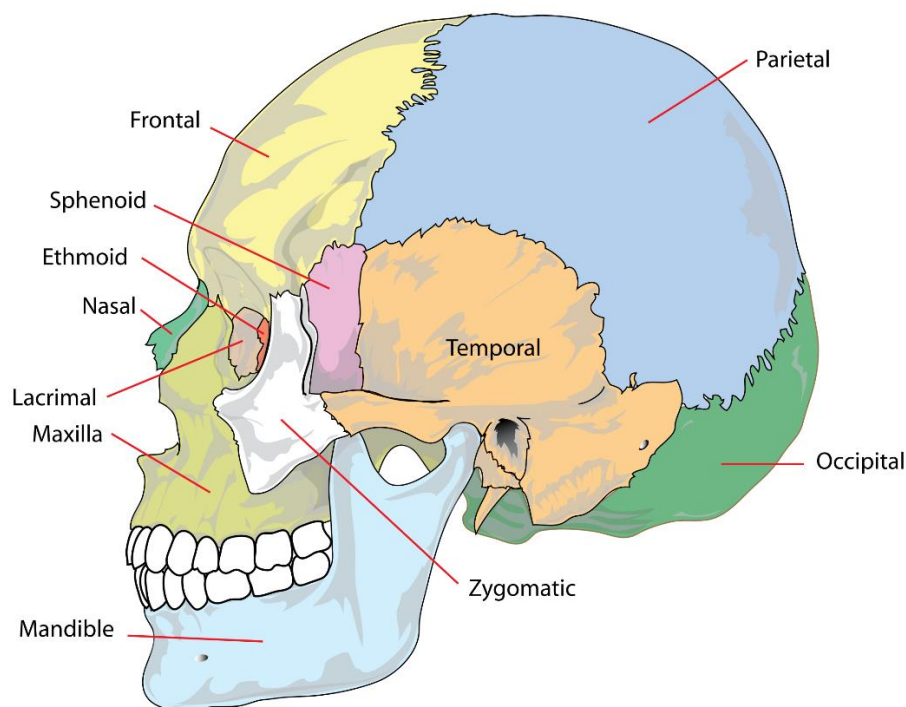


**Figure 1-1 Anatomy of the skull (Adapted from Wikimedia Commons)**

### 1.2.2 Brain anatomy

The human brain has a highly complex anatomical structure. (Figure 1-2) It is enclosed within the skull and is made up of three meningeal connective tissue membranes. Cerebrospinal fluid (CSF) exists between the skull and the brain. The three major components of the human brain are the cerebrum, cerebellum, and brainstem. The cerebrum is the most substantial component, consisting of the cortex, hippocampus, thalamus, basal ganglia, and corpus callosum. The brainstem is made up of the midbrain, pons, and medulla. It connects the cerebrum and spinal cord. The cerebellum is a distinct brain region located at the brain's base and connected to the brainstem.

The central nervous system of the human body is made up of grey and white matter. This structure is composed of nerve cells, glia, capillaries, and neuropil. The white matter comprises myelinated and unmyelinated axons that connect the areas of grey matter (neurons). Moreover, the components of the brain are highly delicate, and even slight deformations can result in TBIs.

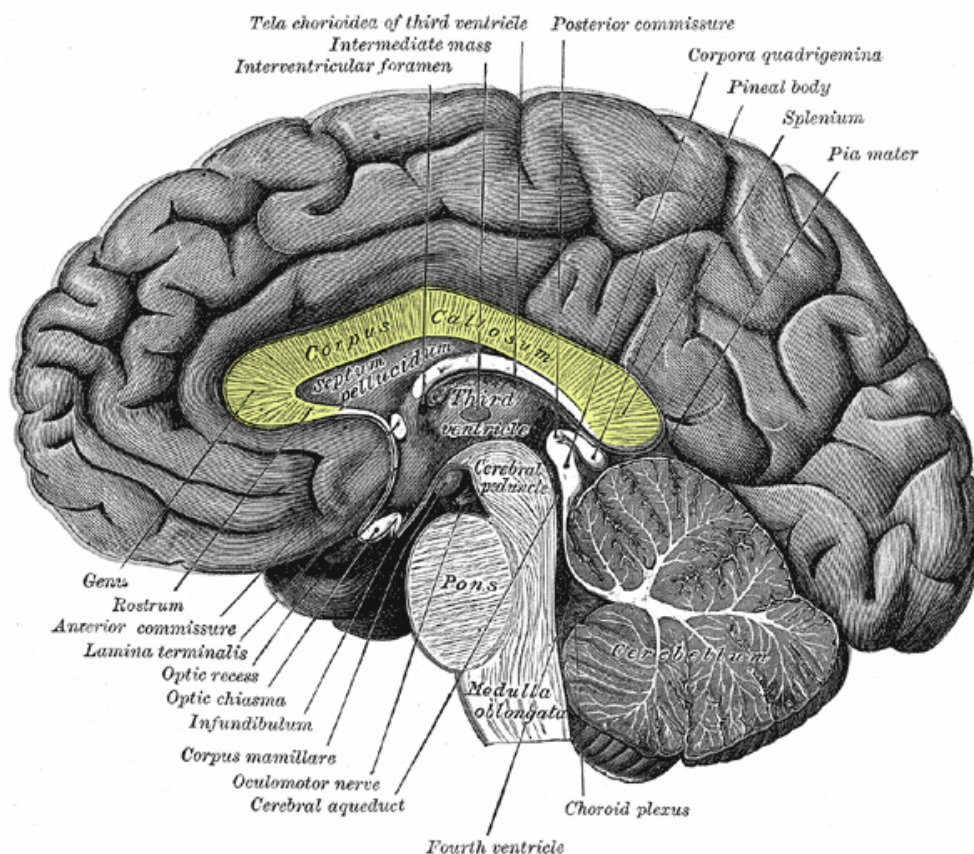


**Figure 1-2 Anatomy of human brain (Adapted from Wikimedia Commons)**

### 1.3 Characteristic of pedestrian head injuries in RTAs

Among vulnerable road users, pedestrians account for a large proportion of fatalities and disabilities in RTA. Road traffic injuries are now the leading cause of death among young adults and children [1]. According to the Governors Highway Safety Association (GHSA), pedestrian fatalities in the United States increased by 5% in 2019 compared to the previous year. Notably, the fatality rate increased by a record 21% in the first half of 2020. Although few people were on the roads due to the COVID-19 pandemic, 2020 had

seen the highest annual increase in pedestrian fatalities since the mid-1970s [16]. (Figure 1-3) Despite advancements in vehicle safety systems over the last decade, pedestrians are still vulnerable to severe and fatal injuries in RTAs.

Head Injuries are the common injuries in CPCs, leading to death or prolonged disability [2-4, 7, 17, 18]. Typical head injuries in CPCs are scalp laceration, skull fracture, and Traumatic Brain Injuries (TBIs), where TBIs are grouped into focal brain injuries (hematoma and contusions) and diffuse brain injuries (Diffuse Axonal Injury (DAI) and Concussion) [5, 6, 9, 19].

RTAs are the leading cause of TBI in the general population [20-23]. A sentinel surveillance [8] on eCHIRPP (The Electronic Canadian Hospitals Injury Reporting and Prevention Program) data from 2011 to 2017 revealed 657 head injury cases among pedestrians struck by motor vehicles on roadways, with 67.1 percent (n = 441) reporting a TBI. (Figure1-4) Previous literature on head injury mechanisms discovered that skull fracture and focal brain injuries are closely related to linear head kinematics (linear acceleration and contact forces). In contrast, diffuse brain injuries are induced by rotational head dynamics [24-28]. Li et al. analyzed the interrelationship between different types of head injuries from the recent GIDAS (German In-Depth-Accident Study) database (2000 -2015) and concluded that skull fracture and focal brain injuries dominate AIS3+ head injuries and concussions dominate AIS2+ head injuries. They claimed that recent cars had softer bonnet structures and better speed control, which reduced skull fracture and focal brain injuries; however, AIS 2+ head injuries, such as concussion, would be the primary concern in future vehicle safety design [12].

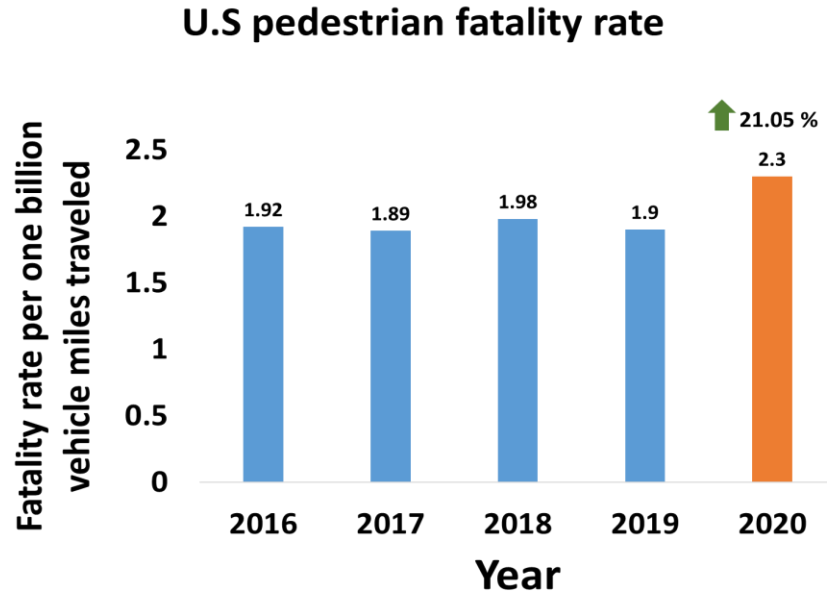


Figure 1-3 U.S pedestrian fatality rate from 2016 to 2020 based on Governors Highway Safety Association (GHSA)

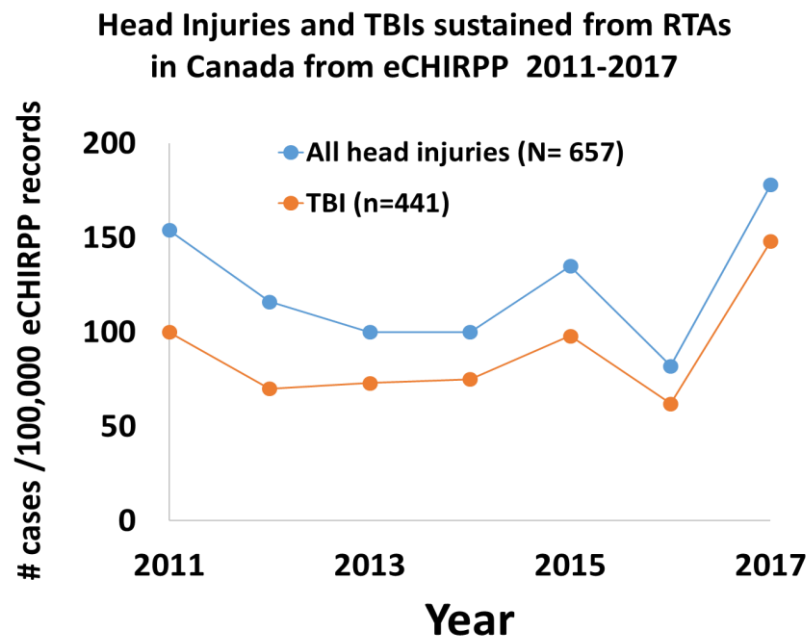
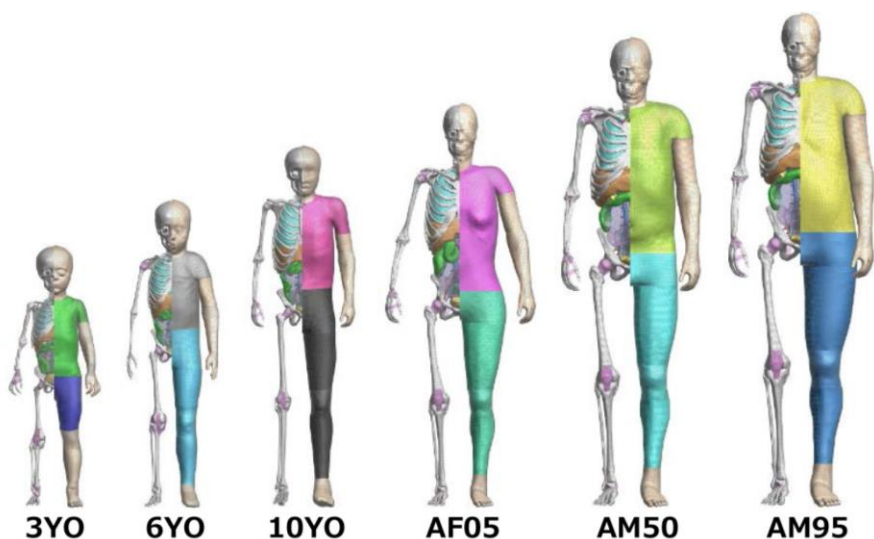


Figure 1-4 Annual distribution of all head injuries and TBIs associated with pedestrian from RTA, eCHIRPP (2011-2017)

## 1.4 Computational Human body model (HBM)

Based on the volunteers' computed tomography (CT) and magnetic resonance imaging (MRI), human body models were developed, and material properties based on literature were assigned [29]. Both component-wise and whole body of the HBM was validated against experimental cadaver data. The Earliest FE head model was developed from Wayne State University (WSC) [30]. Later the model was refined and detailed by modeling white and grey matter [31]. There after many organizations started to develop their model. Mao et al. developed a GHBMC model based on a multi-block approach using high-quality hexahedral brain meshes and validated against 35 cadaver data [32, 33]. Besides the GHBMC, another head and a full-scale pedestrian model commonly used in the automobile industry and academic users is the Total Human Model for Safety, developed by Toyota Central R & R&D Labs, Inc. and Toyota Motor Corporation. (Figure 1-5) In addition, there are other models, including Simulated Injury Monitor (SIMon) FEHM [34], University of Dublin Brain Trauma Model (UCDBTM) [35], Kungliga Tekniska Högskolan (KTH) [36], and Dartmouth Head Injury Model (DHIM) [37].



**Figure 1-5 THUMS (The Total Human Model for Safety)**

## 1.5 Review of head injury criteria

In recent decades, head injury metrics have been calculated using the head's kinematic response to the impact. The Wayne State Tolerance Curve (WSTC) was one of the earliest and widely referred metrics, defined based on the relationship between linear acceleration and duration of impact [38, 39]. (Figure 1-6)

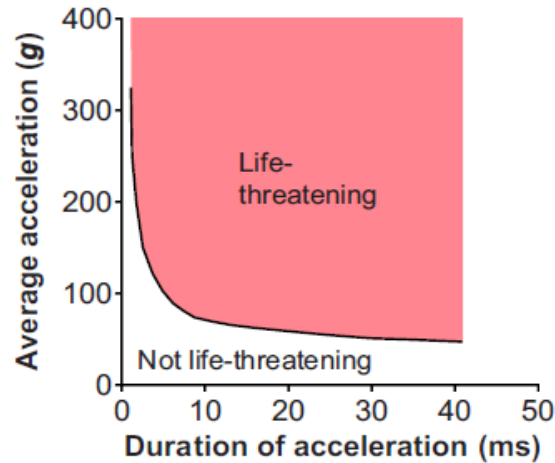


**Figure 1-6 The Wayne State Tolerance Curve (WSTC)**

According to WSTC, the head can tolerate higher peak accelerations for a very brief period. Inversely, head injuries can occur when the duration of the same magnitude of the acceleration is prolonged. Additionally, WSTC data were used to develop many widely used injury metrics, including the Gadd Severity Index (GSI), which is calculated by integrating linear acceleration to the power of 2.5, which can yield idealistic peak values for impacts with longer pulse duration [40, 41]. While GSI effectively quantifies severe skull fractures and brain injuries, it is inefficient at predicting concussion risk [42]. Equation 1 represents the mathematical GSI.

$$GSI = \int a(t)^{2.5} dt \quad (1)$$

Where 'a' is the effective acceleration of the head in terms of g, acceleration due to gravity, and 't' is the time in milliseconds [43].



Furthermore, by focusing on the severity index for the portion of the impact that is expected to be relevant for the risk of brain injury, the Head Injury Criterion (HIC) can be calculated by averaging the integrated curve of the resultant acceleration and time over the time interval containing the maximum HIC value. Equation 2 shows the mathematical expression for HIC.

$$HIC = \max_{t_1, t_2} \left\{ (t_2 - t_1) \left[ \frac{1}{t_2 - t_1} \int_{t_1}^{t_2} a(t) dt \right]^{2.5} \right\} \quad (2)$$

Where ‘ $t_1$ ’ and ‘ $t_2$ ’ referred to any two arbitrary times on the acceleration of the head ‘ $a$ ’ in terms of  $g$  and time ‘ $t$ ’ in milliseconds [44]. In 1972, the National Highway Traffic Safety Administration (NHTSA) narrowed  $t_2$  and  $t_1$  to a maximum of 36 milliseconds (HIC36) and a maximum HIC36 of 1000. Additionally, NHTSA introduced HIC15, which requires that  $t_2$  and  $t_1$  be no more than 15 milliseconds apart and have a maximum value of 700 [45]. For risk prediction, HIC is widely used in a variety of industrial and research fields. HIC is frequently used to quantify traumatic brain injuries (TBIs), but its predictive accuracy has been consistently questioned. HIC has been recognized as a classical metric for predicting head injuries caused by road traffic accidents [46]. However, in a real-world collision, head injury is caused by a combination of linear and angular acceleration, and HIC is a subjective criterion that only considers linear acceleration. As a result, the Generalized Acceleration Model for Brain Injury Threshold (GAMBIT) was proposed, incorporating linear and rotational kinematics. It can be determined by calculating the maximum linear and angular accelerations measured at the head's center of gravity (COG). Mathematically, it is equivalent to Equation 3.

$$GAMBIT = \left[ \left( \frac{a_{max}}{a_{cr}} \right)^2 + \left( \frac{\alpha_{max}}{\alpha_{cr}} \right)^2 \right]^{\frac{1}{2}} \quad (3)$$

Where ‘ $a_{max}$ ’ is the peak linear acceleration of the head in  $g$ , ‘ $\alpha_{max}$ ’ is the maximum angular acceleration in radians per square seconds and ‘ $a_{cr}$ ’ and ‘ $\alpha_{cr}$ ’ are the critical linear and angular acceleration [47]. Using scaled animal models and collaboration with the National Highway Traffic Safety Administration, a rotational brain injury criteria – Brain Injury Criteria (BrIC) – was developed. In contrast to angular acceleration, BrIC

strongly correlates with the angular velocity component, and their critical values are both dependent on and independent of the ATD (Anthropomorphic Test Dummy) used for the measurements [48]. BrIC analysis has become crucial for comprehending vehicle and dummy motion during the development of the restraint system test. BrIC was recently updated by NCAP (New Car Assessment Program) as a new head Injury criteria in automobile oblique impact crash tests. Mathematically, it is equivalent to Equation 4.

$$BrIC = \sqrt{\left(\frac{\omega_x}{\omega_{xc}}\right)^2 + \left(\frac{\omega_y}{\omega_{yc}}\right)^2 + \left(\frac{\omega_z}{\omega_{zc}}\right)^2} \quad (4)$$

Where ' $\omega_x$ ', ' $\omega_y$ ', and ' $\omega_z$ ' are maximum angular velocities in X, Y, and Z-axes respectively, and ' $\omega_{xc}$ ', ' $\omega_{yc}$ ', and ' $\omega_{zc}$ ' are the critical angular velocities in their respective direction [49]. On the hypothesis that the rate of change of linear and rotational kinetic energy, i.e., power, would be a feasible assessment function for mTBI, new criteria called Head Impact Power (HIP) were proposed [50]. Additionally, to provide an estimate associated with mild rather than severe TBI, the Head Impact Telemetry Severity Profile (HITSP) is used, a weighted composite score based on linear, rotational, and duration of the impact [51].

Nevertheless, the head is considered a rigid mass without deformation when the HIC and HIP criteria are computed. Deformation of the skull and internal organs became possible with the development of finite element and computational methods and greatly aided in developing novel injury criteria. Over the last decade, more than ten distinct three-dimensional finite element head models (FEHM) have been developed. By bridging the gap between macro-and micro-level kinematics and injury assessment, FEHM was instrumental in simulating the brain response to external impact [29]. While considering the varying sizes of a human head-on impact, KTH introduced the head size dependence of intracranial stress associated with injury using FEHM from Stockholm Royal Institute [36]. To assess the possibility of TBI in automobile crashes, a new set of criteria known as the Simulated Injury Monitor (SIMon) criteria was developed to predict three distinct types of brain injury using three different injury metrics [34].

- I. **Cumulative Strain Damage Measure (CSDM):** A correlate of Diffuse Axonal Injury (DAI) associated with the cumulative volume of brain tissue undergoing tensile strains above a predefined critical level. By calculating the strain levels in a volume fraction of brain tissue, CSDM predicts DAI [34]. Equation 5 shows the mathematical equation of CSDM15, which calculates the volume fraction of brain tissue undergoing maximum principal strain over 15%.

$$CSDM15 = \frac{\# \text{ of elements Maximum Principal Strain (MPS) over 0.15}}{\text{total no. of elements}} \quad (5)$$

- II. **Dilatational Damage Measure (DDM):** A predictor of the risk of contusions, which are typically counter-coup injuries caused by negative pressure in localized regions of brain tissues as a result of dilatational stress [34].
- III. **Relative Motion Damage Measure (RMDM):** A correlation for acute subdural hematoma (ASDH) in which the injuries are caused by the brain moving relative to the cranium's interior surface [34].

Subsequently, based on volunteer sled tests and professional football reconstruction, injury criteria for FEHM – Global Human Body Model Consortium (GHBMC) were developed. These criteria include a detailed skull, face, and brain structures [33, 52]. Because a second-order mechanical system behaves similarly to the brain's deformation response to angular head motion in the absence of a complete-time history of head impact. Two new brain injury metrics have been developed.

- I. **Universal Brain Injury Criterion (UBrIC)** was developed using the relationship between rotational head kinematics and strain-based injury metrics such as Maximum Principal Strain (MPS), the maximum value of MPS occurring across all brain FE elements throughout the event time history, and CSDM. Mathematically, represented as Equation 6.

$$UBrIC = \left\{ \sum_i \left[ \omega_i^* + (\alpha_i^* - \omega_i^*) e^{\frac{\alpha_i^*}{\omega_i^*}} \right]^r \right\}^{\frac{1}{r}} \quad (6)$$

Where ' $\omega_i^*$ ' and ' $\alpha_i^*$ ' are the directionally dependent ( $i = x, y, z$ ) maximum magnitudes of head angular velocity and angular acceleration each normalized by a critical value ( $cr$ );  $\omega_i^* = \omega_i / \omega_{icr}$  and  $\alpha_i^* = \alpha_i / \alpha_{ic}$  [53, 54].

- II. **Diffuse Axonal Multi-Axis General Evaluation (DAMAGE)** was developed to predict maximum brain strain based on directional dependent angular acceleration time histories from head impacts and used in a wide range of automobile crashes and sports. Mathematically, represented as Equation 7.

$$DAMAGE = \beta \max_t \{ |\vec{\delta}(t)| \} \quad (7)$$

Where ' $\beta$ ' is a scale factor that relates the maximum resultant displacement of the system to the MPS value from the FE brain model [55]. Apart from the tolerance level for brain injury caused by SDH (Subdural Hematoma), a threshold curve called the critical strain curve was proposed. This curve is expressed in terms of peak angular acceleration and change in angular velocity and demonstrates no axonal injury between 5% and 10% critical strain. Above these values, concussions can be expected, as can DAI [5, 56].

Due to the widespread use of FEHM, several physical parameters such as coup, contrecoup pressure, von Mises, and shear stress can be used to predict the risk of brain injury [57]. It is common to use a widely used injury severity scale called The Abbreviated Injury Scale (AIS) to classify and describe specific injuries. The AIS was developed by the Association for the Advancement of Automotive Medicine (AAAM) and ranged from 0 (no injury) to 6 (severe injury) (fatal injury). It was initially used to define MVC epidemiologically but has since been applied to all forms of trauma [58]. Following subsequent revisions, head sections are modified to capture additional information about head injuries, such as the size of the hematoma, to improve the accuracy of coding in concussive head injuries. The most recent revision, AIS – 2015, enhanced brain injury coding to increase its reliability for research [59, 60]. (Table 1-1)

**Table 1-1 The Abbreviated Injury Scale (AIS) [49, 50]**

<b>AIS- Code</b>	<b>Injury</b>
AIS 1	Minor
AIS 2	Moderate
AIS 3	Serious
AIS 4	Severe
AIS 5	Critical
AIS 6	Maximum

## 1.6 Research outline

To better understand the effect of vehicle front shape, pedestrian body size, and pre-impact gait posture on TBI risks of pedestrians during CPCs, the thesis focuses on the following objectives.

1. Quantifying the relationship between vehicle front shape parameters and AIS2+ pedestrian head injury risk by identifying the most significant vehicle shape parameters.
2. Identifying the effect of pedestrian height and body mass on TBI risks when vehicle shape parameters are varied.
3. Investigating the relationship between the injury risks of skull fracture and diffuse brain injuries.
4. Understanding the effect of different pedestrian pre-impact gait postures on dynamic head response and brain strains.
5. Investigating the pedestrian TBI risks for various gait postures in the same and different gait types.

The outline of this thesis is mentioned below:

**Chapter 01** indicates research rationale, head, and brain anatomy, head injury characteristics in RTAs, Finite element model, and injury metrics used to assess pedestrian TBI risk

**Chapter 02** describes the influence of vehicle front shape parameters on pedestrian TBI risk across the diverse pedestrian population with varying body shapes during CPCs

**Chapter 03** illustrates the influence of pedestrian pre-impact gait postures on the dynamic head and intracranial brain strain response during CPCs.

**Chapter04** contains the conclusion and future work of this thesis.

## Chapter 2

### 2 Investigating the influence of vehicle front shapes and pedestrian body size on traumatic brain injuries sustained in car-to-pedestrian collisions using the pedestrian finite element model

This chapter is co-authored by Dr Haojie Mao

#### 2.1 Abstract

*Traumatic brain injuries (TBIs) are the leading cause of death and long-term disability in road traffic accidents (RTAs). Over the last decade, studies have examined the effect of vehicle front shape and pedestrian body size on the risk of pedestrian head injury. The relationship between vehicle front shape parameters and pedestrian TBI risks during vehicle impacts, on the other hand, has never been quantified in previous numerical studies involving a diverse population with varying body sizes. Thus, the purpose of this study is to comprehensively study the effect of vehicle front shape parameters and variable pedestrian body size on the dynamic response of the head and the risk of TBIs during primary (vehicle) impact. At three different collision speeds (30, 40, 50 km/h), 48 car-to-pedestrian collisions (CPCs) were reconstructed using four different vehicle types (Subcompact, Mid-Sedan, Sports Utility Vehicle (SUV), and Pickup truck) and four distinct THUMS pedestrian FE models (AF05, AM50, AM95, and 6YO). We used head kinematic and intracranial strain-based head injury criteria to assess the risk of TBIs. Our findings indicate that vehicle shape parameters such as BLEH (Bonnet leading edge height), BA (Bonnet angle), and WA (Windshield angle) are significant predictors of pedestrians' TBI risk in CPCs. The prevalence of skull fractures increases the risk of diffuse brain injuries. For pedestrian head rotation in low BLEH vehicles, pedestrian height and body mass are statistically significant factors. Vehicles with a high BLEH and a low BA were more likely to cause AIS4+ focal and diffuse brain injuries. Furthermore, increasing BLEH in head-to-windshield impact and decreasing BLEH in head-to-bonnet impact reduce the risk of mild TBIs.*

## 2.2 Introduction

Road traffic injuries (RTAs) are now the leading cause of death for young adults and children [20-23]. Pedestrians account for a large proportion of fatalities and disabilities among highly vulnerable road users (VRUs). Global status report on road traffic accidents released by WHO (World Health Organization) indicated that nearly 1.35 million people die every year from road traffic accidents [1]. According to GHSA (Governors Highway Safety Association), pedestrian fatalities in the U.S increased by 5% in 2019 over the previous year. Notably, in the first half of 2020, the fatality rate surged by a record 21 percent. Even few people were on the road due to the COVID-19 pandemic, the largest ever annual increase in pedestrian fatalities per mile driven was recorded in 2020 since mid-1970 [16]. Through advancements in vehicle safety and autonomous technology have improved the survivability of vehicle occupants in crashes, pedestrians are still vulnerable to severe and fatal injuries in RTAs.

Previous studies found that head injuries are the most common injuries in CPCs, often resulting in death or permanent disability [2-4, 7, 17, 18]. Typical pedestrian head injuries include scalp laceration, skull fracture, and traumatic brain injuries (TBIs), which are further grouped into focal brain injuries (hematoma and contusions), and diffuse brain injuries, such as diffuse axonal injury (DAI), diffuse vascular injury (DVI) and concussion, are the most common pedestrian head injuries sustained in traffic collisions [5, 6, 9, 19]. RTAs are the leading cause of TBI in the general population [20-23]. Dawodu et al. found that RTAs account for approximately 50% of all TBIs in the United States [61]. On a detailed analysis of 10,341 pedestrian accident cases from eight European nations, Arregui- Dalmases et al. found that TBIs are significantly higher than skull fracture [62]. Subsequently, sentinel surveillance on eCHIRPP (The Electronic Canadian Hospitals Injury Reporting and Prevention Program) data from 2011 to 2017 revealed 657 head injury cases among pedestrians struck by motor vehicles on roadways, with 67.1 percent (n = 441) reporting a TBI [8]. Watanabe et al. performed a comprehensive numerical study with the THUMS pedestrian model and claimed that skull fracture and DAI were not closely associated [63]. At the same time, Li et al. analyzed the interrelationship between different types of head injuries from the recent



GIDAS (German In-Depth-Accident Study) database (2000 -2015). They concluded that skull fracture and focal brain injuries dominate AIS3+ head injuries and concussions dominate AIS2+ head injuries. He concluded that AIS 2+ head injuries such as concussion would be the primary concern in future vehicle safety design [12].

Numerous studies have examined the source of head injury, with a particular emphasis on car-to-pedestrian collisions (CPCs) [64-67]. Based on a detailed review of 205 in-depth accidents, Badea et al. claimed that, though head impacts with the road outnumbered vehicle impacts, vehicle impacts accounted for a more significant proportion of more serious (AIS2+ and AIS3+) head injuries. According to an on-the-spot pedestrian accident study in the United Kingdom, vehicle impacts were the leading source of skull fracture and intracranial injuries that do not result in isolated loss of consciousness than ground impacts [68].

The influence of age on different types of head injury remains controversial, considering inconsistent remarks from the previous literature [69-72]. Harruff et al. studied 217 pedestrian accidents. They found that young adults were more likely than older adults to sustain head injuries, with TBIs like contusion and brain stem injury accounted for more than half of all head injuries [73]. However, as people get older, the volume of grey matter in the brain decreases while the volume of cerebrospinal fluid increases [74]. Viano et al. discovered that the proportion of patients with a poor neurological outcome increases with age, implying that older patients have a lower TBI injury tolerance [75]. Richard et al. found that pedestrian age is significant for TBIs than skull fractures based on the clinical record from England [72].

Previous research stated that the risk of pedestrian head injury increases as the pedestrian's height and weight increase [76]. However, Lui et al. discovered that short pedestrians encountered a greater risk of head injury than tall pedestrians [77]. Changes in pedestrian height have an effect on the locations of head contacts [78]. Moreover, very few studies have analyzed the head injury risk of child pedestrians [79].

While vehicle impact speed is the most critical factor [63, 80, 81], the front design of the vehicle has a significant impact on pedestrian head injuries [9, 80, 82]. Several studies

examined the effect of vehicle front design on pedestrian head injuries using whole-body postmortem human subjects (PMHS) [83], in-depth accident data analysis [9, 12, 84], and numerical simulations [11, 66, 79, 85]. According to previous research, SUVs and light truck vehicles (LTV) caused more severe head injuries than pedestrians struck by a passenger car [86-90]. Li et al. discovered that vehicles with a longer bonnet have a higher rate of head injuries when compared to passenger cars and minivans [11]. While another study found that shorter bonnets result in more head impacts with the vehicle's windscreen than long bonnets, resulting in more severe head injuries [3]. Otte et al. discovered that increasing the windscreen angle increases the severity of head injuries [91]. These studies, however, are based on a limited number of collision scenarios and a specific population of pedestrians.

Bonnet leading edge height (BLEH) was the most dominating factor in pedestrian head injury risk. According to a recent study, BLEH had the most significant impact on HIC values, while bonnet angle had the most significant effect on head angular acceleration [78]. Guibing et al. used multibody simulation to examine pedestrian head injury in a wide range of impact scenarios and found that increasing BLEH increases head injury risk in adults [11]. Another study found that none of the vehicle's shape parameters are statistically significant for AIS 3+ head injuries [9]. Li et al. examined the GIDAS (German In-Depth-Accident Study) database and concluded that none of the vehicle parameters is significant for AIS 3+ head injuries like skull fracture and focal brain injuries. BLEH, on the other hand, had statistical significance with AIS 2+ head injuries like concussion. He also claimed that increasing BLEH by 1 cm reduced the risk of concussion in sedans by 17% during windshield impact [12].

As a result, the influence of vehicle shape parameters on pedestrian AIS2+ injuries like concussion and DAI have not been studied across a wide range of pedestrian populations in the past literature. Most of the findings were based on in-depth analysis of accident data and multibody numerical reconstruction studies. Furthermore, the effect of vehicle shape parameters on the risk of pedestrian TBI during a vehicle collision has never been studied using a full-scale human body model (HBM).

The primary objective of this study was to investigate the relationship between vehicle shape parameters and the risk of pedestrian AIS2+ head injury during vehicle impact across a diverse population of pedestrians, including children. To accomplish this, four distinct full-scale FE human body models and four distinct vehicle models were used to reconstruct car-to-pedestrian collisions (CPC). Additionally, the risk of AIS4+ head injuries and the effect of skull fracture on diffuse brain injuries (DBIs) were evaluated using kinematic and intracranial tissue level strain-based head injury criteria calculated from the accident reconstruction simulation results.

## 2.3 Methods

### 2.3.1 Simulation models

#### **Pedestrian FE model**

THUMS (The Total Human Model for Safety) version 4 & 4.02 pedestrian FE models developed by Toyota Central R&D Labs, Inc. and Toyota Motor Corporation were used in this study. Four different body sizes, such as (A) Child (6YO), (B) Small size female (AF05), (C) Average size male (AM50), and (D) large size male (AM95), in a mid-stance walking posture, was considered to represent a wide variety of population. (Figure 2-1) All models have been tested against PMHS (Post-Mortem Human Subject) data in the literature at both the component and whole-body levels [85]. In addition, trajectories of the model in the car to pedestrian collisions (CPC) were validated against the corridors defined in Euro NCAP technical bulletin TBO24 [92, 93]. Table 2-1 shows the body mass, stance, and center of gravity (C.G) from the ground of the four different sized THUMS models.

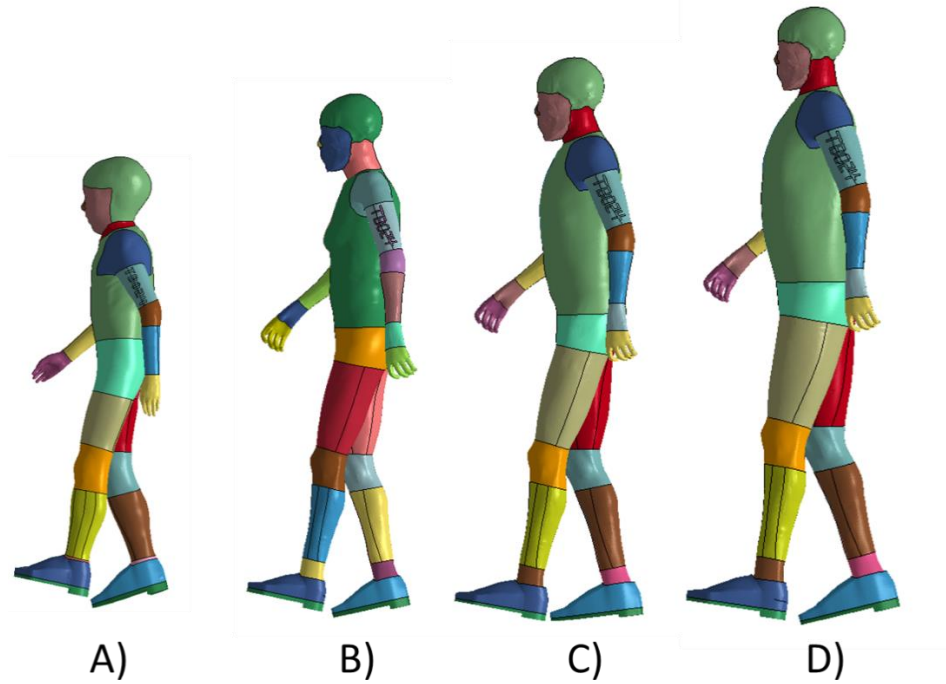


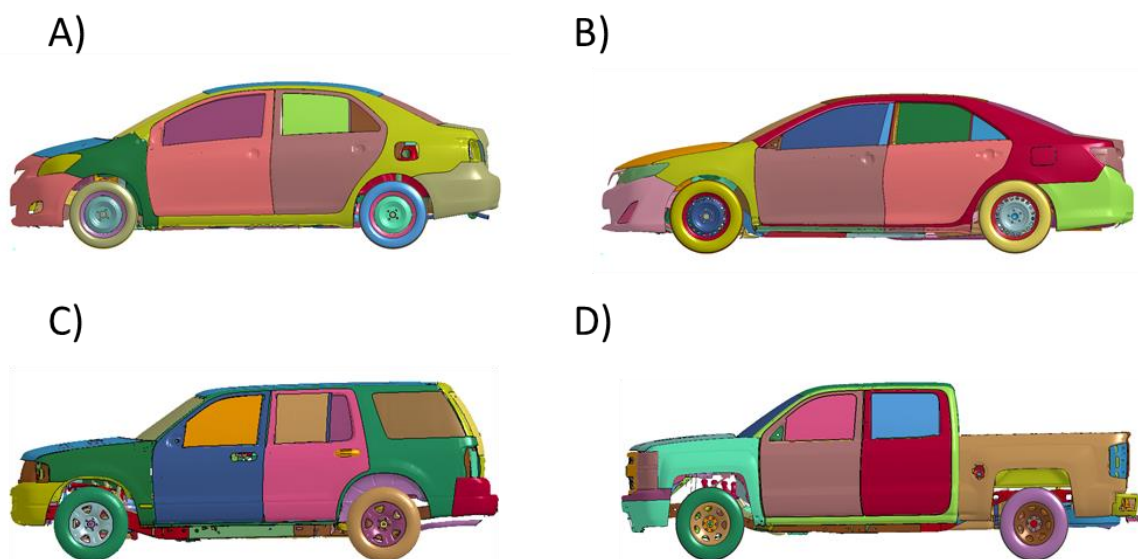
**Figure 2-1 A) Child 6YO B) Small Female 5<sup>th</sup> percentile AF05 C) Average Male 50<sup>th</sup> percentile AM50 D) Large Male 95<sup>th</sup> percentile AM95**

**Table 2-1 Body mass, stance, and center of gravity (C.G) from the ground of all pedestrian FE model**

	<b>Body Mass (kg)</b>	<b>Stance (mm)</b>	<b>C.G (mm)</b>
<b>A) Child (6YO)</b>	25	1204	683
<b>B) Small female (AF05)</b>	49	1563	893
<b>C) Average male (AM50)</b>	78	1785	1033
<b>D) Large male (AM95)</b>	106	1946	1113

## Vehicle FE model

Four vehicle models (subcompact, midsize sedan, Sports Utility Vehicle (SUV), and pickup truck) with distinct front-end shapes (Figure 2-2) were chosen, all of which were commonly involved in road traffic accidents. The NCAC (National Crash Analysis Center) Toyota Yaris (model year 2010) [94] and Ford Explorer (model year 2002) [95] models were selected as the subcompact and SUV cars, respectively. Besides, Toyota Camry (year 2012) FE model [96] produced by CCSA (Center for Collision Safety and Analysis, George Mason University(Fairfax, VA) and Chevrolet Silverado (model year 2014) FE model created by EDAG Inc (Troy, MI). were used as the midsize car and pickup truck, respectively. All numerical car models have been developed through a reverse engineering approach and validated against many full-scale crash test data.

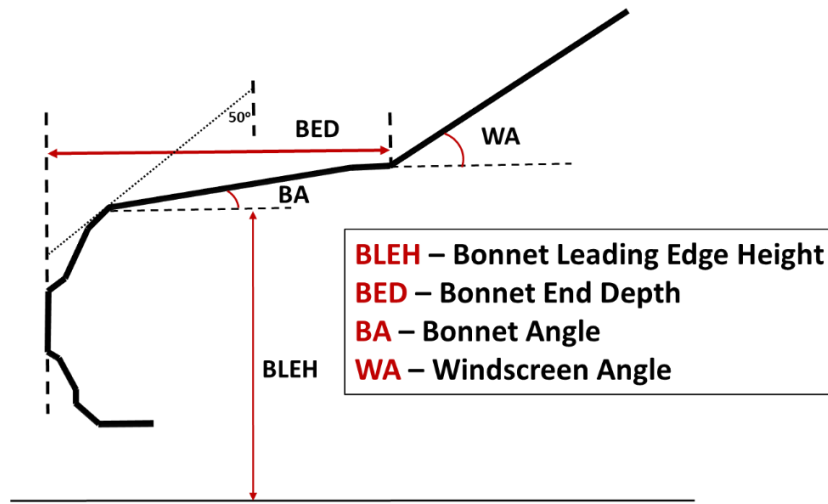


**Figure 2-2 A) Toyota Yaris 2010 B) Toyota Camry 2012 C) Ford Explorer 2002 D) Chevrolet Silverado 2014**

Vehicle front shape parameters such as Bonnet Leading Edge Height (BLEH), Bonnet End Depth (BED), Bonnet Angle (BA), and Windshield Angle (WA) were measured for all the vehicle models based on the previous studies [9, 84] (Figure 2-3) and the European Enhanced Vehicle Safety Committee –Working Group report (EEVC WG17) protocol [97], as shown in Table 2-2.

**Table 2-2 Vehicle front shape parameters measured from all vehicle model**

	Vehicle type	BLEH (mm)	BED (mm)	BA (deg)	WA (deg)
A) Toyota Yaris 2010	Subcompact	754.52	904.17	26.23	30.19
B) Toyota Camry 2012	Mid-sedan	771.09	1150.29	26.204	30.66
C) Ford Explorer 2002	SUV	1070.54	1063.99	18.69	38.95
D) Chevrolet Silverado 2014	Pickup truck	1188.88	1299.91	15.38	34.85

**Figure 2-3 Vehicle front shape parameter measurements**

### 2.3.2 Development of simplified FE vehicle model

All vehicle FE models were developed to evaluate frontal crashworthiness as well as active and passive occupant safety. Further, a full-scale vehicle model in the pedestrian crash simulation would result in a greater computing cost and numerical complexity. As a result, these models have to be modified to perform CPC simulations [80, 98]. All frontal structures up to the B pillar were extracted from the original model using Hypermesh (Altair, Troy, MI USA). Both doors were also removed. All the engine components below the hood remained in situ. All vehicle contact, material definitions were

unchanged. Nodal mass elements from the original car model were not deleted, and mass values have remained unchanged. Trimmed edge of the FE nodes and nodal mass elements are constrained to the nodal mass element at the C.G location as in the original model. Extra masses were added to the C.G nodal mass to obtain the same mass as the original car model. Accelerometer definitions in the front structure of the vehicle were not deleted. A similar front structure trimming protocol was followed for all vehicle models. All trimmed vehicle models are shown in Figure 2-4.

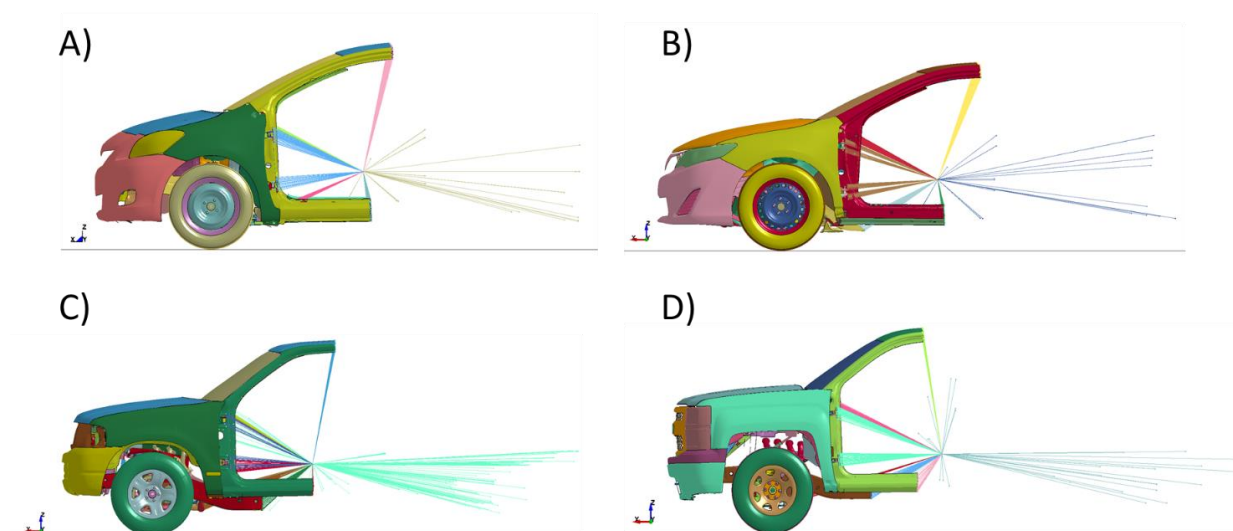


**Figure 2-4 Simplified vehicle FE model A) Toyota Yaris – Subcompact passenger sedan B) Toyota Camry – Mid-size sedan C) Ford Explorer – Sports Utility Vehicle (SUV) D) Chevrolet Silverado – Pickup truck**

### 2.3.3 Validation of simplified FE vehicle model

According to the New Car Assessment Program (NCAP), the simplified vehicle model was validated by conducting a full-frontal wall impact test according to the New Car Assessment Programme (NCAP). The results were compared to the whole car model and actual NHTSA experimental test results. The FE Simulation was performed in LS-DYNA (Ver. SMP s R9.2.0, LSTC). The simplified car models were set to impact the rigid wall at 50 km/h. The gravitational load was applied to the entire model setup. Static/dynamic contact friction coefficient was defined as 0.2 and 0.1 between the vehicle and rigid wall [94, 99]. Contact friction between the tires and ground surface was defined as 0.9 [94,

99]. All contact and boundary conditions were defined as per the NCAP test. Accelerometers were positioned in the exact location of the whole car model and NCAP. The overall global deformation pattern of the crash and global acceleration response from the engine top and bottom were compared in Figures 2-5 and 2-6. Deformation patterns were found to be quite similar, and reasonable agreement was found from the acceleration response for the simplified vehicle.

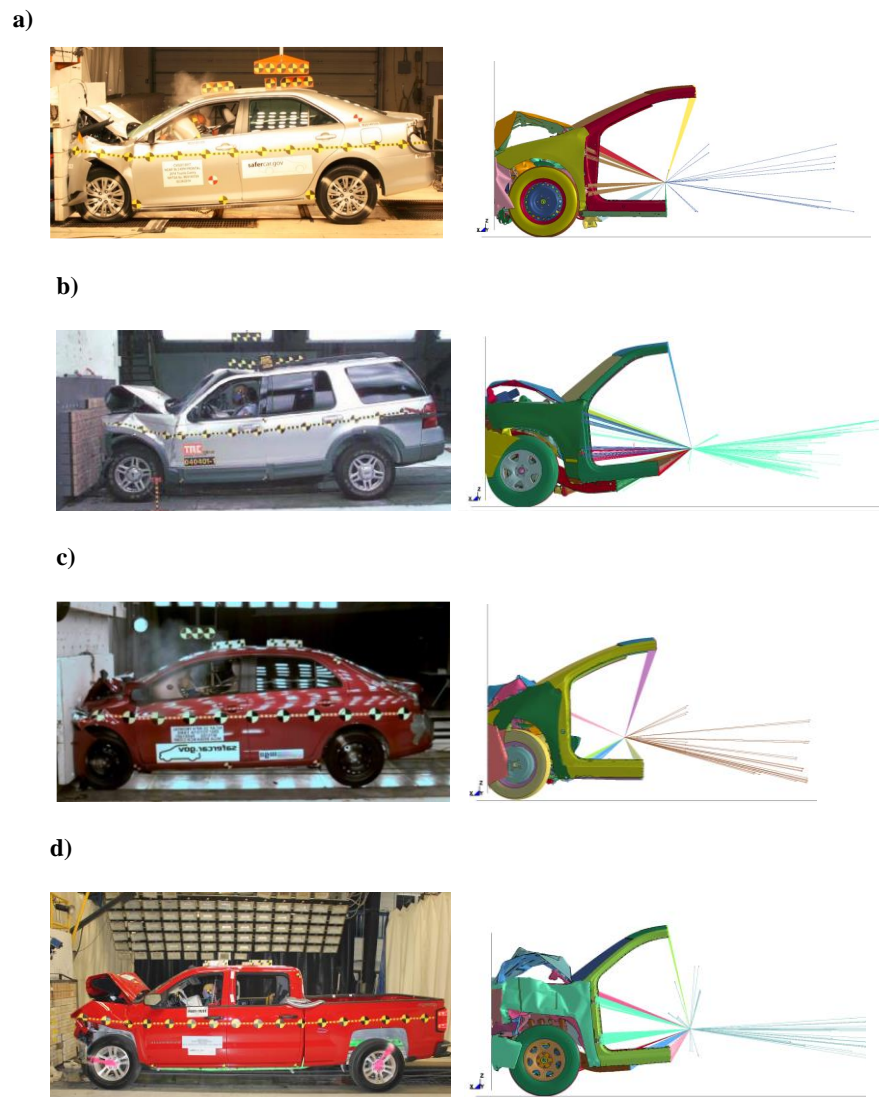


**Figure 2-5 Global deformation pattern of full-frontal crash test a) Toyota Yaris b) Toyota Camry c) Ford Explorer d) Chevrolet – Silverado**



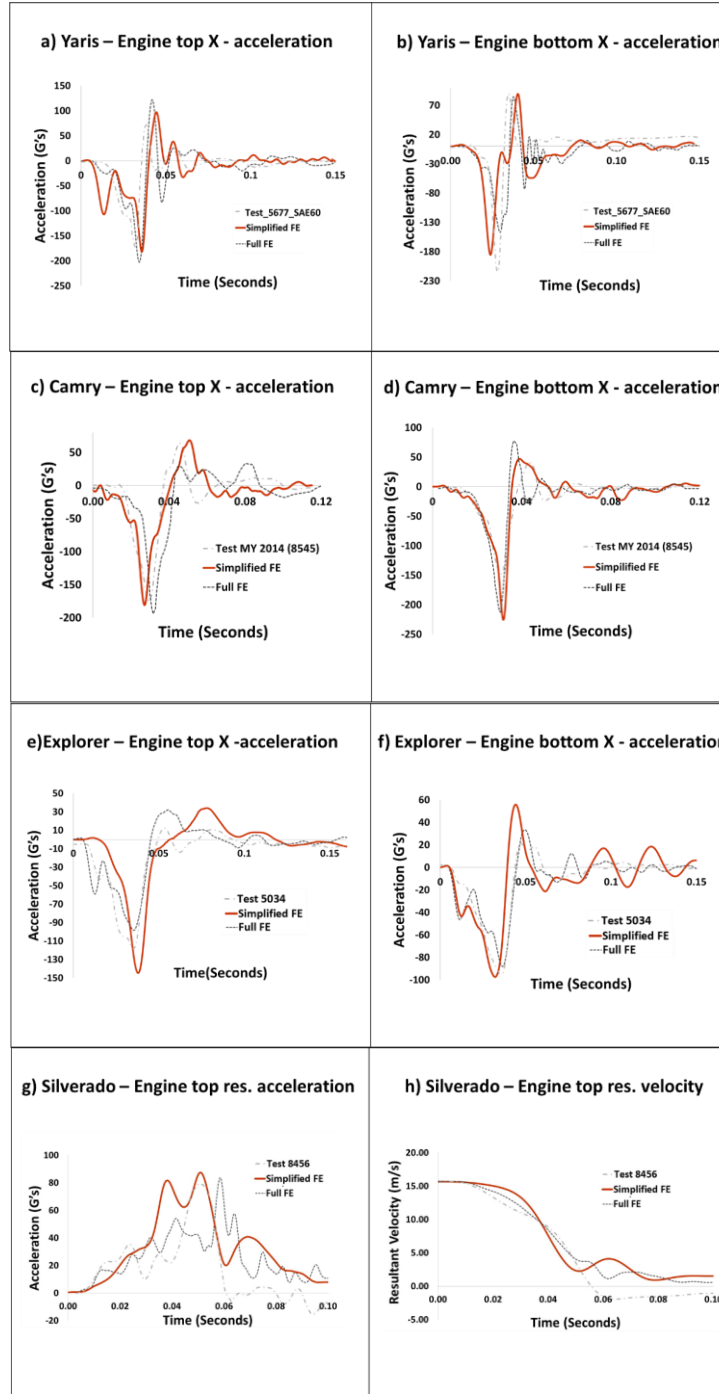


**Figure 2-6 a) Yaris engine top X acceleration b) Yaris engine bottom X acceleration c) Camry engine top X acceleration d) Camry engine bottom X acceleration e) Explorer engine top X acceleration f) Explorer engine bottom X acceleration g) Silverado engine top resultant acceleration h) Silverado engine top resultant velocity.**

### 2.3.4 Validation of pedestrian head kinematics in CPC

Car to pedestrian collision (CPC) was simulated, and the dynamic head responses between the full and simplified model were compared to the simplified model for pedestrian injury studies. THUMS average male 50<sup>th</sup> percentile (AM50) pedestrian model was used. Initially, the pedestrian model in midstance walking posture was positioned laterally at the vehicle centerline. Simulation configuration set up adopted by pedestrian testing protocol of Euro NCAP [100] was employed as shown in Figure 2-7. The vehicle was accelerated at 40 km/h and laterally impacted the pedestrian model at the vehicle centerline. Head CG of the pedestrian model was positioned in line with the vehicle centerline ( $y=0$  in the global coordinate system). The contact friction coefficient of 0.65 was defined between the vehicle and pedestrian model while between pedestrian shoe and ground was defined as 0.7 based on the literature [80]. The gravitational load was applied to the entire model setup. 6DOF accelerometer was defined at the CG of the pedestrian head to measure the velocity and acceleration responses in the head local coordinate system. All the acceleration and velocity pulses were filtered by CFC 180 [76]. Head linear acceleration and rotational velocity responses were compared between the simplified and full-scale vehicle models. Figure 2-8 illustrates the overall kinematic response during CPC between baseline and simplified midsize sedan model. Good agreement was noted from the dynamic head responses from all simplified models, as shown in Figure 2-9.

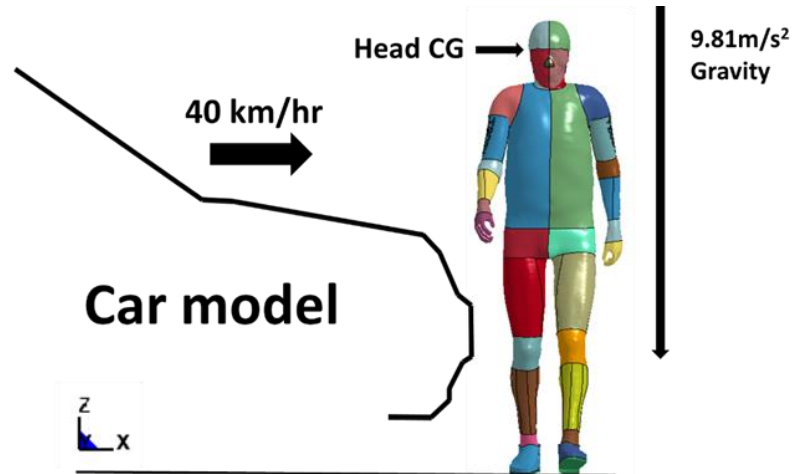


Figure 2-7 Car-to-pedestrian collision NCAP configuration setup – Simplified car models were accelerated at 40 km/h and impacted the pedestrian FE model at the vehicle centerline (y-axis). A gravitational load of  $9.81\text{m/s}^2$  was applied to all nodes and a 6DOF accelerometer was defined at the CG of the pedestrian head.

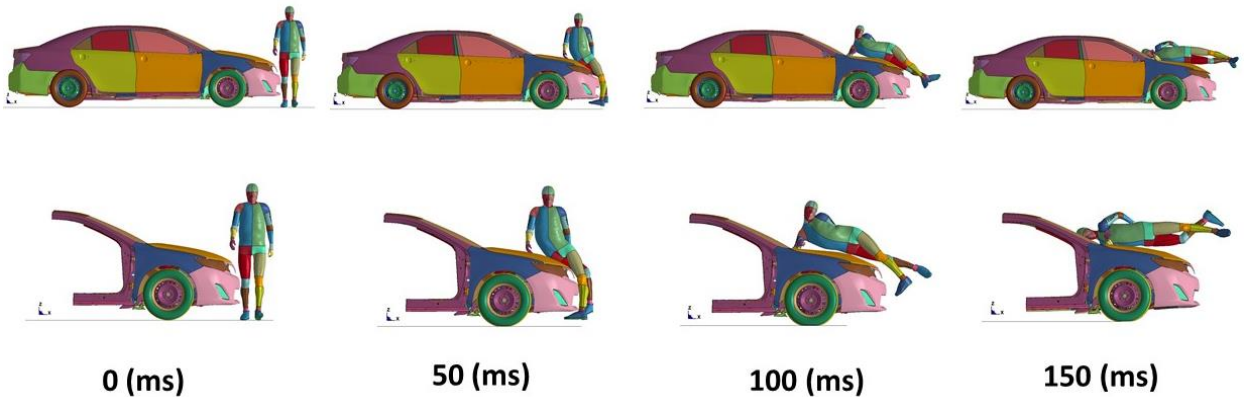
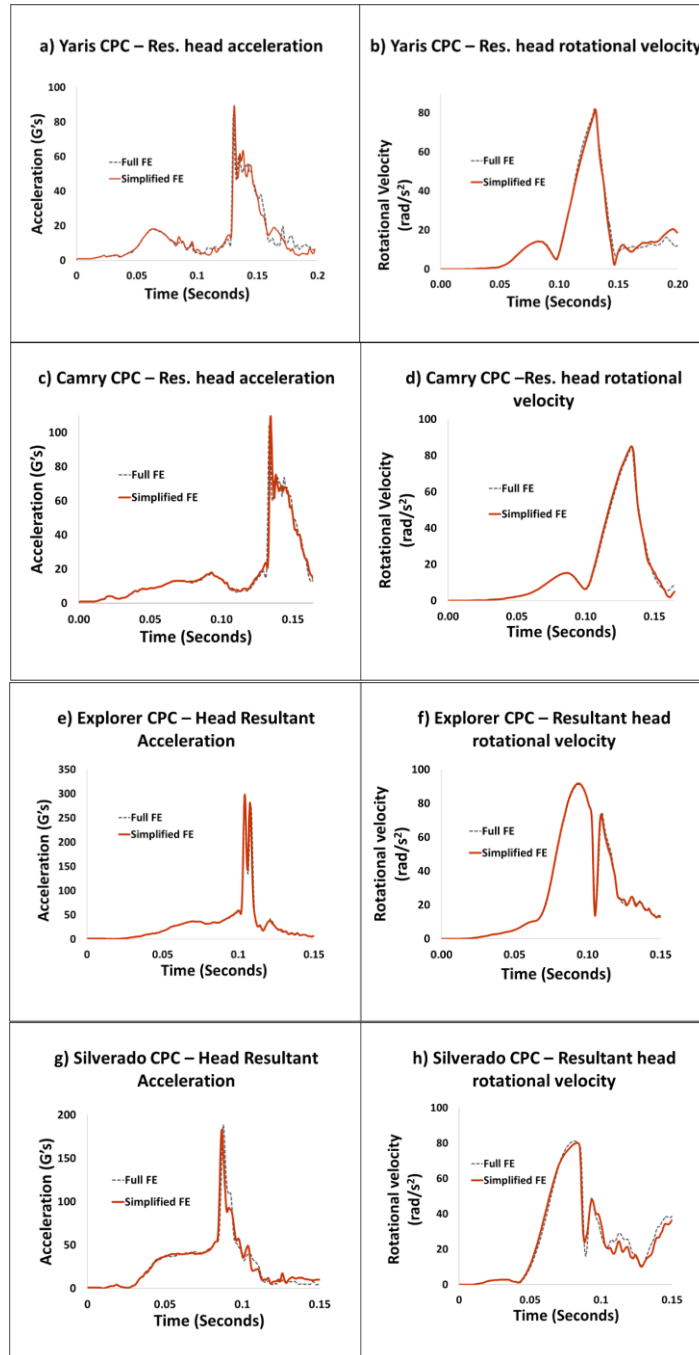


Figure 2-8 Pedestrian kinematics of Average male 50<sup>th</sup> percentile in CPC (Mid-size sedan, 40 km/h)



**Figure 2-9 a) Yaris CPC head resultant acceleration b) Yaris CPC head resultant velocity c) Camry CPC head resultant acceleration d) Camry CPC head resultant velocity e) Explorer CPC head resultant acceleration f) Explorer CPC head resultant velocity g) Silverado CPC head resultant acceleration h) Silverado CPC head resultant velocity**

## 2.4 Accident reconstruction

The accident reconstruction workflow involves three steps pipeline, as shown in Figure 2-10.

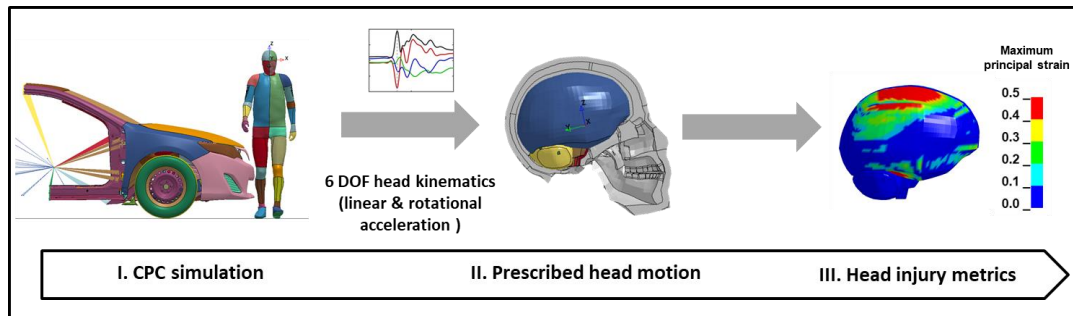


**Figure 2-10 Accident reconstruction – three-step pipeline**

### I. CPC simulation

Full-scale pedestrian kinematics in road traffic accidents are reconstructed using four simplified vehicle and THUMS FE models in LS-DYNA code (Ver. SMP s R9.2.0, LSTC) to get the head kinematics. Boundary conditions outlined in the Euro NCAP pedestrian HBM testing protocol [100] have been used. Initially, the HBM model (without walking speed) was positioned laterally in front of the vehicle with the right side of HBM as struck side. Simplified vehicle models were accelerated at three different collision speeds (30, 40, and 50 km/h) and impacted the pedestrian model at the vehicle centerline [63]. The head COG of the HBM was positioned in line with the vehicle centerline. A gravitational load of  $9.8\text{m/s}^2$  was applied to the entire simulation. The coefficient of contact friction between the pedestrian model and the vehicle was 0.65, while the coefficient of contact friction between the shoes and the ground was 0.7 [80]. The accelerometer was defined at the CG of the pedestrian head to measure the acceleration responses in the head local coordinate system. All the linear and rotational acceleration curves were filtered by CFC 180 [85]. A total of 48 CPCs were simulated.

## II. Prescribed head motion

Head-to-car impacts were reconstructed by performing a prescribed head motion using an isolated THUMS FE head model in LS-DYNA code (Ver. SMP s R9.2.0, LSTC). Six Degree of Freedom (DOF) head kinematics (three linear and three rotational acceleration) from CPC simulation were prescribed to the isolated head model to analyze strain-based intracranial response for all simulated cases.

## III. Head injury metrics

Twelve head injury criteria were calculated for all simulated cases using MATLAB code. The head kinematics in the local coordinate system was used to calculate the kinematics-based injury metrics and intracranial responses to estimate the strain-based tissue injury criteria. Table 2-3 describes the 50% risk of AIS4+ level injuries threshold for estimated head injury metrics.

**Table 2-3 Injury threshold values used for head injury criteria**

	<b>Head Injury metric</b>	<b>Threshold for 50% AIS4+ head injury</b>
<b>Kinematic based metrics</b>	Peak linear acceleration [45] [101]	200 -250g
	Peak angular acceleration [102]	10,000 rad/s <sup>2</sup>
	Peak angular velocity [56]	46.5 rad/s
	Head Injury Criterion (HIC <sub>15</sub> ) [45]	700g
	Brain Injury Criterion (BrIC) [48]	1.06
	Diffuse Axonal Multi-Axis General Evaluation (DAMAGE)	NA
<b>Skull Fracture</b>	Skull von-mises stress [103, 104]	96.53 MPa
	Maximum principal strain (MPS) [48]	0.9

<b>Intracranial strain-based metrics</b>	Average Maximum principal strain (MPS mean)	NA
	Top 5% Maximum principal strain (MPS 95 <sup>th</sup> percentile)	NA
	Cumulative Strain Damage Measure (CSDM15) [34]	0.55
	Cumulative Strain Damage Measure (CSDM25) [34]	0.25

## 2.5 Results

### 2.5.1 Pedestrian Kinematics

#### **Collision with subcompact sedan**

The impact kinematics of all pedestrian models in a 40 km/h collision with a sub-compact passenger sedan are shown in Figure 2-11. AM50 and AM95 exhibited the following kinematics. The bumper initially collided with the knee. The femur then made contact with the front grill, rotating the upper body. The pelvis made contact with the hood's front end, and the upper body shifted toward it. The elbow and shoulder collided with the underside of the windshield or frame. Finally, the head made contact with the windshield glass. In AM50, the head collided with the center of the windscreen, whereas in AM95, the head and shoulder collided almost simultaneously with the top windshield area.

In AF05, the vehicle's leading-edge collided with the femur and pelvis, resulting in upper body rotation. The elbow made contact with the hood in a short duration, and the head impacted the lower windshield or frame. In 6YO, the bumper and leading edge collided with the mid-body region, and the shoulder contacted the front end of the hood. The head swivelled laterally around the shoulder and impacted the hood.

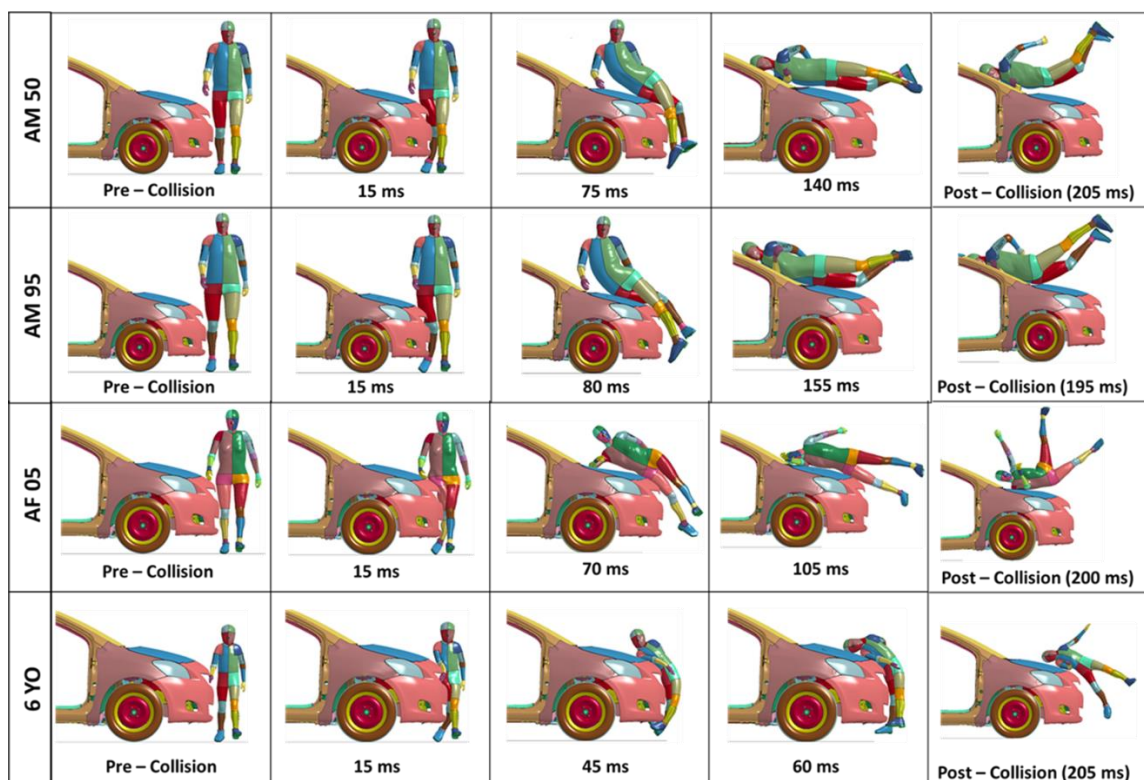


**Figure 2-11 Pedestrian Kinematics (Compact sedan – Yaris, 40 km/h)**

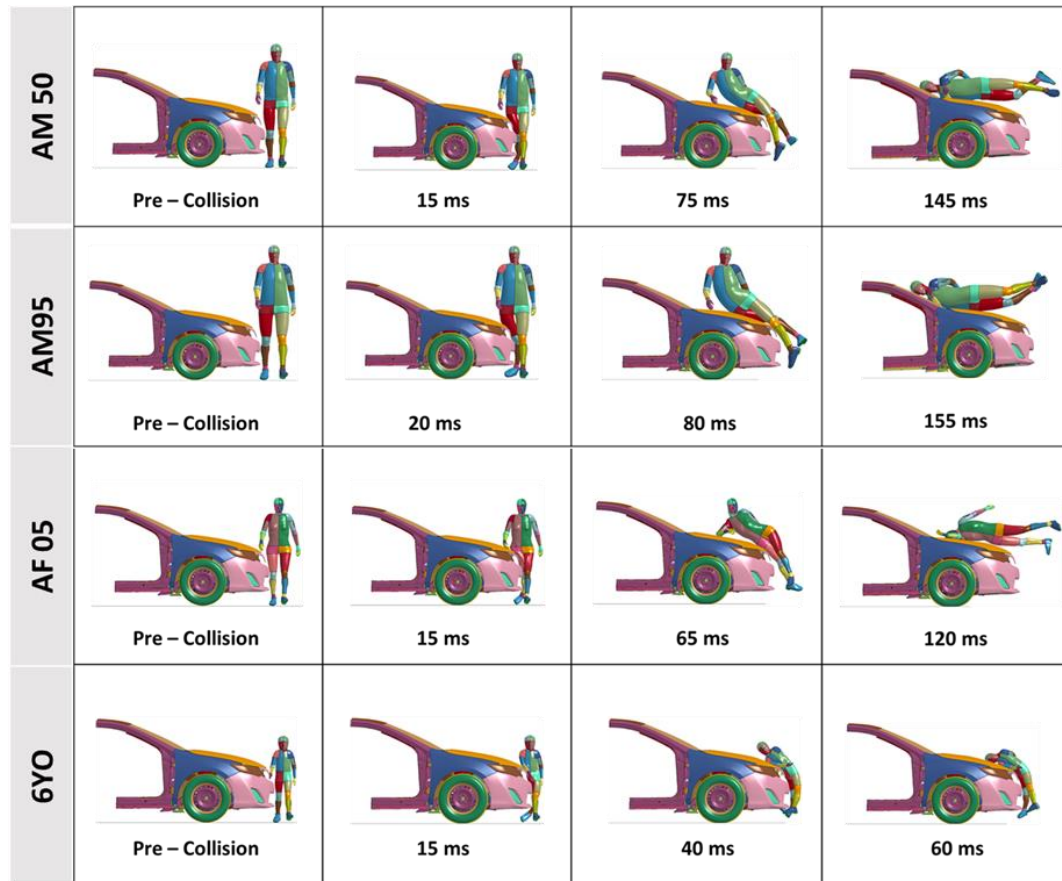
### Collision with mid-size sedan

Figure 2-12 depicts the impact kinematics of all pedestrian models in collision with a mid-size sedan at 40km/h. In general, pedestrian kinematics for all models were comparable to that of a subcompact sedan. Due to the increased Bonnet End Depth (BED), however, the impact location of the arm and head were different. In the AM50, the elbow contacted the cowl panel, and the head impacted the lower windshield. In contrast, in the AM95, the elbow made contact with the lower windshield, and both the head and shoulder impacted the windshield almost simultaneously.

In AF05, the head impacted the hood surface rather than the windshield, and in 6YO, the head and shoulder made contact in the same location as in the compact sedan.



**Figure 2-12 Pedestrian Kinematics (Mid-sedan – Camry, 40 km/h)**



### **Collision with sports utility vehicle (SUV)**

Figure 2-13 shows the impact kinematics of all pedestrians in collision with SUV at 40 km/h. Typical pedestrian kinematics were observed in all adult (AM50, AM95, and AF95) pedestrian models. At first, the bumper impacted the knee, then the femur made contact with the grill next, and the pelvis contacted the leading edge of the vehicle almost simultaneously. The upper body rotated, moving towards the hood, and the chest reached the hood, followed by the shoulder. The head finally impacted the hood. In AM50, the head impacted the center of the hood, whereas, in AM95, the head impacted the rear end of the hood. In AF05, lateral upper rotation was higher than AM50 and AM95.

In 6YO, the bumper contacted the mid-body region first, and the shoulder made contact with the grill. The head then finally impacted the leading edge of the hood.

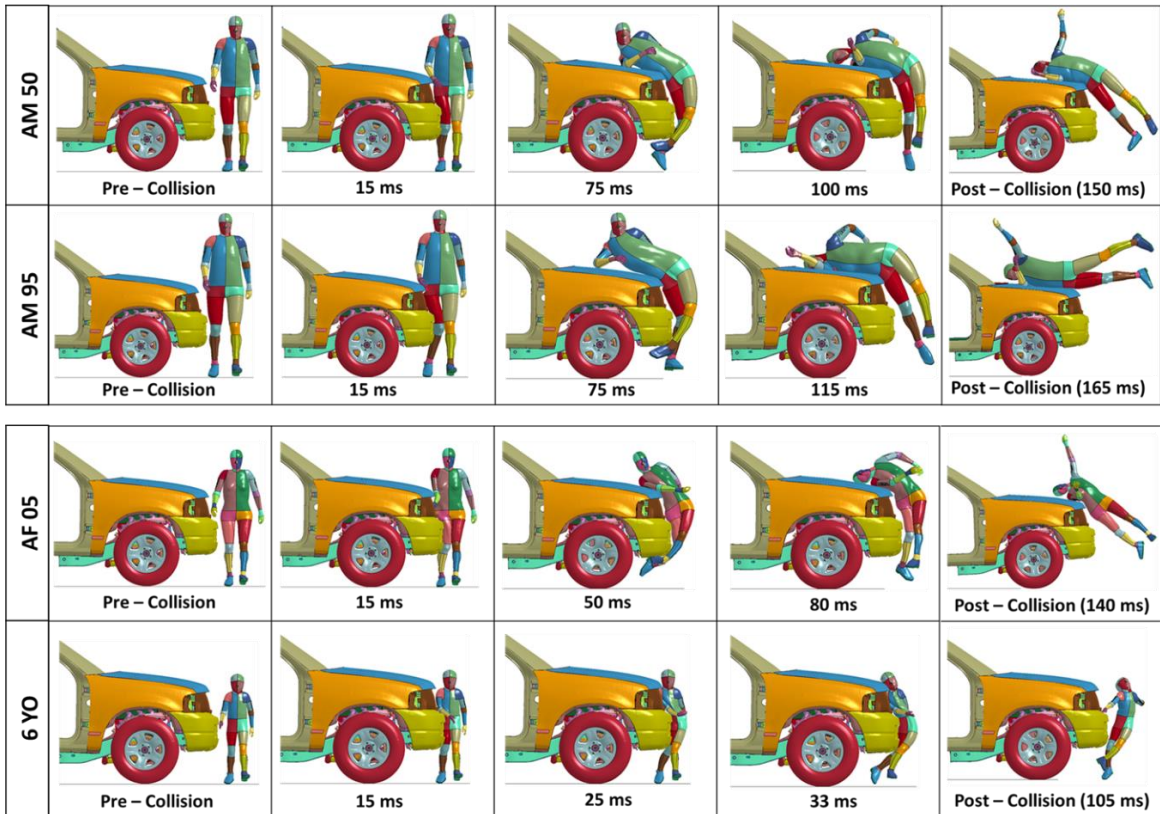


**Figure 2-13 Pedestrian Kinematics (SUV – Explorer, 40 km/h)**

### Collision with pickup trucks

Figure 2-14 depicts the impact kinematics of all pedestrian models in collision with a pickup truck at 40 km/h. All pedestrian kinematics for all models were comparable to that of an SUV.

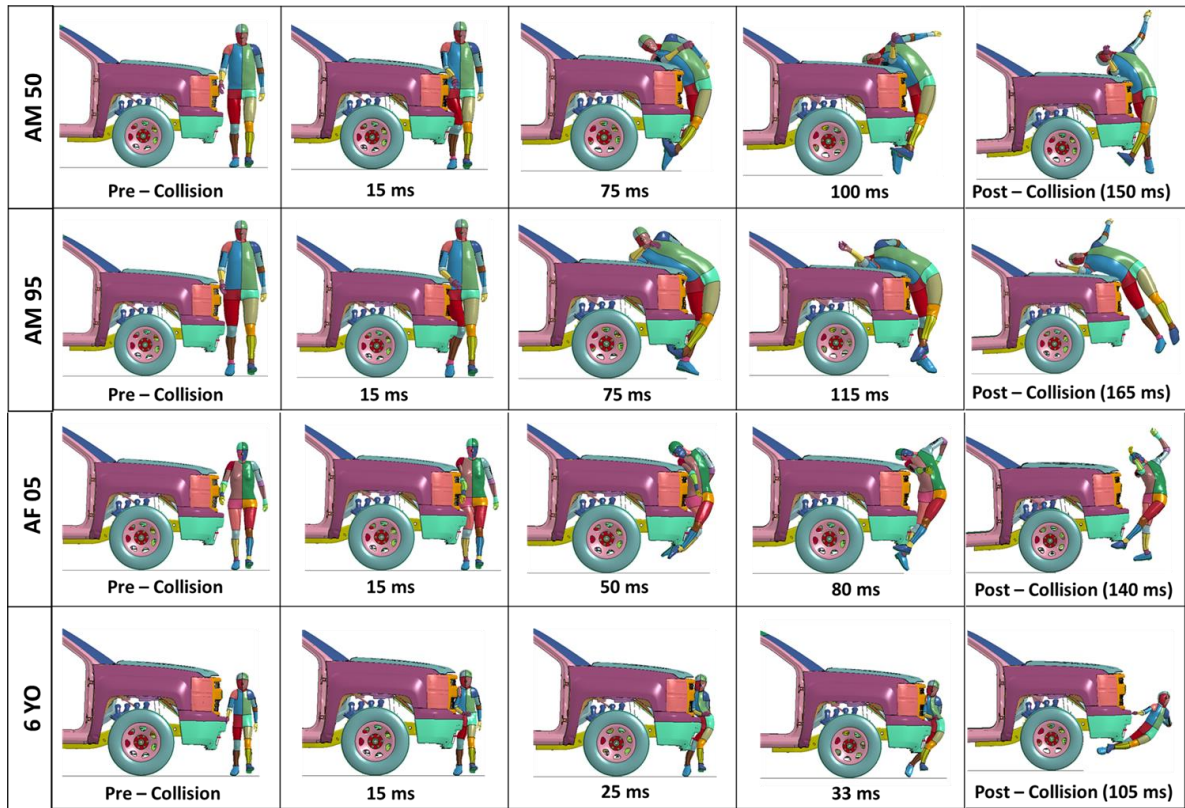


**Figure 2-14 Pedestrian Kinematics (Pickup truck – Silverado, 40 km/h)**

## 2.5.2 Linear head kinematics

The distribution of linear head injury metrics such as peak linear acceleration and HIC15 for different vehicle front shapes and pedestrian body sizes were compared to the AIS4+ thresholds of the respective metrics in Figure 2-15. All HIC15 mean values exceeded the AIS 4+ threshold except for the mid sedan, while all vehicle types' average peak linear acceleration falls within the AIS 4+ threshold. All pedestrian types except 6YO have average peak acceleration below the threshold, whereas HIC values of all body sizes exceed the threshold.

SUVs were the most susceptible to AIS4+ focal head injuries, with an average HIC of 1917 and peak acceleration of 210g. In contrast, mid sedans were the least vulnerable, with an average HIC of 547 and peak acceleration of 111g, respectively. Box plot indicates that SUVs' HIC values were normally distributed for different speeds and pedestrian types but positively skewed for a mid-sedan with the minor variability. Pickup

trucks were at second, with an average HIC of 1588 and the highest peak acceleration (228g), as well as more dispersion and positively skewed HIC values. In contrast to the mid sedan, the passenger sedan had a mean HIC value of 1210, higher than the AIS 4+ threshold.

The 6YO pedestrian type was the most susceptible to AIS 4+ focal head injuries, with an average HIC and linear acceleration of 1528 and 241g, respectively. In contrast, the AF05 pedestrian type was the least susceptible, with an average HIC and linear acceleration of 1104 and 175g, respectively. AM50 was the second vulnerable pedestrian type, with similar average HIC (1327) and peak acceleration (156g) values to AM95. The distribution of HIC values was positively skewed for all pedestrian types, with a lower degree of variation for AF05.

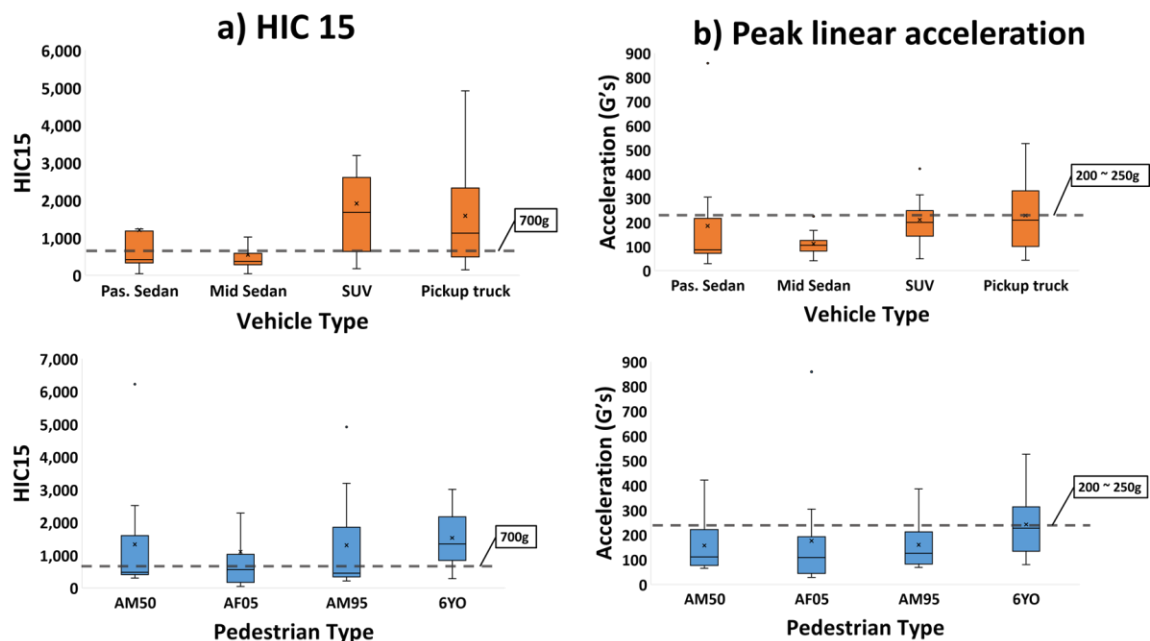


**Figure 2-15 a) Head Injury Criterion (HIC15) b) Peak linear acceleration**

### 2.5.3 Rotational head kinematics

For all vehicle types and pedestrian sizes, rotational kinematic-based head injury metrics such as peak angular acceleration, peak angular velocity, and brain injury criteria (BrIC) were studied and compared to the threshold values for AIS 4+ head injuries. (Figure 2-

16). All vehicle types' rotational metrics exceeded the AIS 4+ threshold, whereas, except for the AM95's BrIC value, all other pedestrian types had predicted values greater than the AIS 4+ threshold.

Our results indicate that SUVs had the highest mean BrIC value of 1.35, with a mean peak angular velocity of 82 rad/s and a mean peak angular acceleration of 28,581 rad/s<sup>2</sup>. Interestingly, pickup trucks had the lowest mean BrIC and high angular velocity of 1.06 and 65.25 rad/s, respectively. In contrast, mid sedans predicted the lowest mean angular acceleration of 13,874 rad/s<sup>2</sup> and a lower degree of variability. Passenger sedans were second with a mean BrIC of 1.33 and mean angular acceleration and velocity of 74.34 rad/s and 18,199 rad/s<sup>2</sup>, respectively. According to the distribution of BrIC values, passenger sedans and pickup trucks were negatively skewed, while SUVs and mid sedans exhibited a symmetric distribution for varying speeds and pedestrian types. According to the distribution of BrIC values, passenger sedans and pickup trucks were negatively skewed, whereas SUVs were positively skewed, and mid sedans exhibited a symmetric distribution across a range of speeds and pedestrian types.

The most vulnerable pedestrian for AIS 4+ rotational head injuries was 6YO with a mean BrIC value of 1.5 and peak angular velocity and acceleration of 90 rad/s and 29,331 rad/s<sup>2</sup>, respectively. AM95 was the least susceptible, with a mean BrIC value of 0.97 less than the AIS 4+ threshold. However, AF05 was the least vulnerable based on peak angular velocity and angular acceleration, with a BrIC value of 1.05 closer to the threshold. AM50 was ranked second with a BrIC value of 1.11 and mean peak angular velocity and acceleration of 77 rad/s and 20,875 rad/s<sup>2</sup>, respectively. The distribution of BrIC values for AF05 was found to be negatively skewed, whereas the distributions for all other pedestrian types were found to be positively skewed.

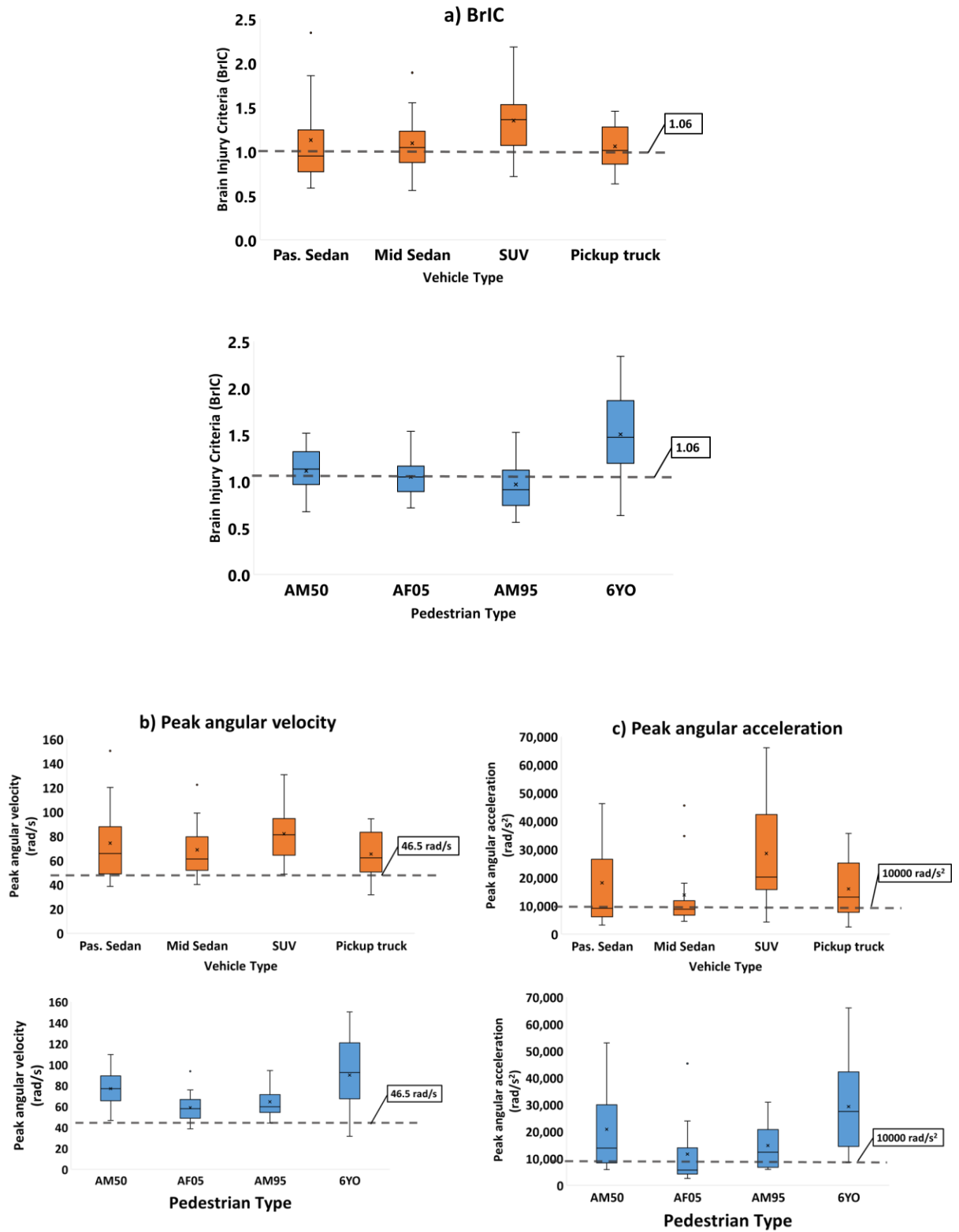


**Figure 2-16 a) Brain Injury Criteria (BrIC) b) Peak angular velocity c) Peak angular acceleration**

## 2.5.4 Intracranial strain response of brain tissue

### **Maximum principal strain (MPS)**

Figure 2-17 compares the distribution of strain-based injury metrics at the brain tissue level, such as DAMAGE, the MPS95th percentile, and the MPSmean, against various vehicle front shapes and pedestrian body sizes,

Mid-sized sedans have the lowest MPS95 value of 0.4 and average MPSmean and DAMAGE values of 0.22 and 0.7, respectively. SUVs have the highest MPS95 value of 0.6 and average MPSmean and DAMAGE values of 0.33 and 0.99, respectively. With an MPS value of 0.53 and the highest degree of variability, pickup trucks were at second. Passenger sedans were third highest with a mean MPS of 0.48, an average MPSmean of 0.28, and an average MPSmean and DAMAGE value of 0.88, respectively. SUVs had a negatively skewed distribution of MPS95 values, whereas all other vehicle types had a positively skewed distribution.

Box plot indicates that AM50 has the highest mean MPS95 of 0.63, as well as the most increased average MPSmean (0.34) and DAMAGE score (1.13), whereas AF50 predicted the lowest MPS value of 0.32, as well as the lowest average MPSmean and DAMAGE score of 0.19 and 0.60, respectively. With mean MPS values of 0.57 and 0.50, 6YO and AM95 were ranked second and third, respectively. Except for AM50, all other pedestrian types had a positively skewed distribution of MPS across a range of speeds and vehicle types.

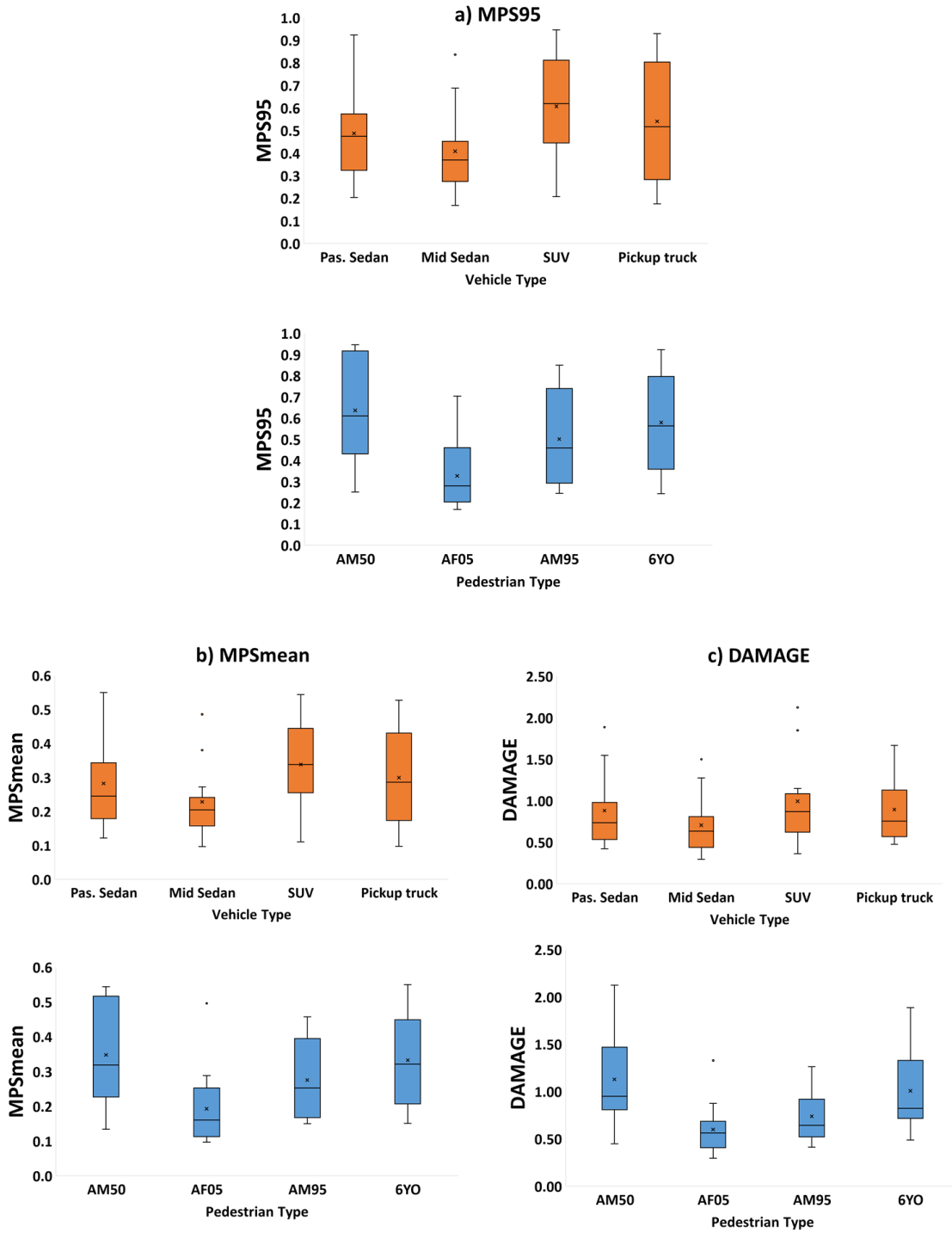


**Figure 2-17 a) Maximum Principal Strain 95th percentile (MPS95) b) Average Maximum Principal Strain (MPSmean) c) Diffuse axonal multi-axis general evaluation (DAMAGE)**



**Cumulative strain damage measure**

Figure 2-18 compares the CSDM15 and CSDM25 distributions for all vehicle types and pedestrian models to the AIS 4+ threshold value. The CSDM15 and CSDM25 values for all vehicles are greater than the threshold values. SUVs had the highest average CSDM15 and CSDM25 values of 0.84 and 0.59, respectively, whereas mid-sedans had the lowest average CSDM15 (0.69) and CSDM25 (0.32). Pickup truck and passenger sedan were ranked at second and third position respectively.

Except for CSDM15 of AF05, all pedestrians had predicted CSDM values greater than the cutoff value. 6YO was found to be the most vulnerable to AIS 3+ diffuse brain injuries when CSDM15 (0.86) and CSDM25 (0.58) values were less than the threshold value, whereas AF05 was found to be the least vulnerable to diffuse brain injuries with CSDM15 (0.54) values were less than the threshold value. AM50 and AM95 were ranked at second and third positions, respectively.

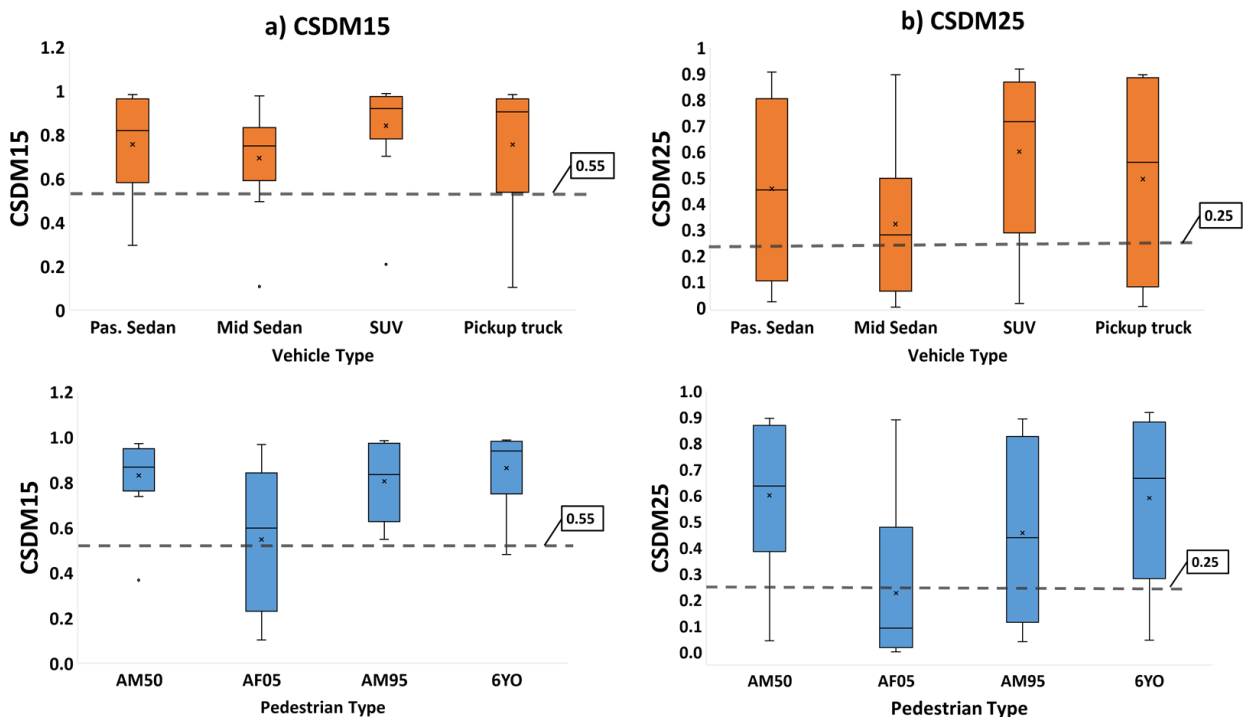


**Figure 2-18 Cumulative Strain Damage Measure (CSDM15) b) Cumulative Strain Damage Measure (CSDM25)**

### 2.5.5 Correlation between head kinematics and brain strains

From all 48 reconstructed cases, the relationship between all impact peak kinematics (such as Resultant Peak Linear Acceleration (RPLA), Resultant Peak Rotational Acceleration (RPRA), Resultant Peak Rotational Velocity (RPRV)) and tissue level strain-based criterion (such as MPS 95<sup>th</sup> percentile, MPS<sub>mean</sub>, CSDM15 and CSDM25) was compared and quantified by performing Pearson and Spearman correlation analysis as illustrated in Table 2-4. In addition, kinematic-based injury criteria such as HIC15, BrIC, and DAMAGE were included in the analysis to better understand the correlation between different strain metrics. Pearson correlation evaluates the linear relationship between two continuous variables, whereas Spearman evaluates the monotonic relationship based on ranked value rather than raw data. The analysis was done using IBM SPSS statistical software. Bivariate correlation coefficient ( $r$ ) and two-tailed test of significance ( $p$ ) were calculated for both correlation studies. However, there was no significant difference between the two coefficients, as Spearman's coefficients were greater than Pearson's.

While both rotational kinematics (RPRA and RPRV) correlate with strain metrics more than peak linear acceleration (RPLA), RPRA has a higher correlation than RPRV. DAMAGE, a strain-based metric calculated from a second-order system and directly dependent on angular acceleration, was heavily correlated with all brain strain metrics. Interestingly, HIC15 has a moderate correlation with all strain metrics, which is comparable to the correlation of BrIC.

Correlation analysis reveals that MPS mean and CSDM25 have a stronger correlation with head kinematics than other strain metrics. Additionally, we used linear regression to compare the MPS mean and CSDM25 to highly correlated head kinematics (RPRA, RPRV, HIC15, BrIC, and DAMAGE). (Figures 2-19 and 2-20) MPS<sub>mean</sub> correlated heavily with DAMAGE ( $R^2 = 0.87$ ,  $P < 0.01$ ), a comparable strain metric, and a stronger correlation with RPRA ( $R^2 = 0.77$ ,  $P < 0.01$ ) than with RPRV ( $R^2 = 0.54$ ,  $P < 0.01$ ). Surprisingly, BrIC was less correlated with MPS<sub>mean</sub> ( $R^2 = 0.49$ ,  $P < 0.01$ ) than HIC15 ( $R^2 = 0.53$ ,  $P < 0.01$ ). Similarly, CSDM25 had a strong correlation with DAMAGE ( $R^2 = 0.71$ ,  $P < 0.01$ ), while RPRA ( $R^2 = 0.66$ ,  $P < 0.01$ ) had a stronger correlation than RPRV

( $R^2 = 0.49$ ,  $P < 0.01$ ). Compared to MPS mean, HIC15( $R^2 = 0.43$ ,  $P < 0.01$ ) was less correlated to CSDM25 than BrIC ( $R^2 = 0.46$ ,  $P < 0.01$ ).

**Table 2-4 Pearson and Spearman correlation analysis between head kinematics and brain strains (N= 48)**

		MPS95	MPSmean	CSDM15	CSDM25
<b>RPLA</b>	Pearson Correlation (r)	0.470	0.551	0.457	0.512
	Sig. 2-tailed (p)	0.001	0.000	0.001	0.000
	Spearman Correlation (r)	0.663	0.706	0.659	0.697
	Sig. 2-tailed (p)	0.000	0.000	0.000	0.000
<b>RPRV</b>	Pearson Correlation (r)	0.737	0.735	0.588	0.705
	Sig. 2-tailed (p)	0.000	0.000	0.000	0.000
	Spearman Correlation (r)	0.741	0.728	0.700	0.747
	Sig. 2-tailed (p)	0.000	0.000	0.000	0.000
<b>RPRA</b>	Pearson Correlation (r)	0.825	0.865	0.656	0.816
	Sig. 2-tailed (p)	0.000	0.000	0.000	0.000
	Spearman Correlation (r)	0.884	0.912	0.866	0.899
	Sig. 2-tailed (p)	0.000	0.000	0.000	0.000
<b>HIC 15</b>	Pearson Correlation (r)	0.680	0.733	0.499	0.658
	Sig. 2-tailed (p)	0.000	0.000	0.000	0.000
	Spearman Correlation (r)	0.781	0.807	0.743	0.808
	Sig. 2-tailed (p)	0.000	0.000	0.000	0.000
<b>BrIC</b>	Pearson Correlation (r)	0.694	0.703	0.551	0.681
	Sig. 2-tailed (p)	0.000	0.000	0.000	0.000
	Spearman Correlation (r)	0.681	0.681	0.673	0.707
	Sig. 2-tailed (p)	0.000	0.000	0.000	0.000
<b>DAMAGE</b>	Pearson Correlation (r)	0.927	0.938	0.660	0.848
	Sig. 2-tailed (p)	0.000	0.000	0.000	0.000
	Spearman Correlation (r)	0.948	0.943	0.828	0.928
	Sig. 2-tailed (p)	0.000	0.000	0.000	0.000

***RPLA –Resultant Peak Linear Acceleration; RPRV–Resultant Peak Rotational Velocity; RPRA- Resultant Peak Rotational Acceleration***

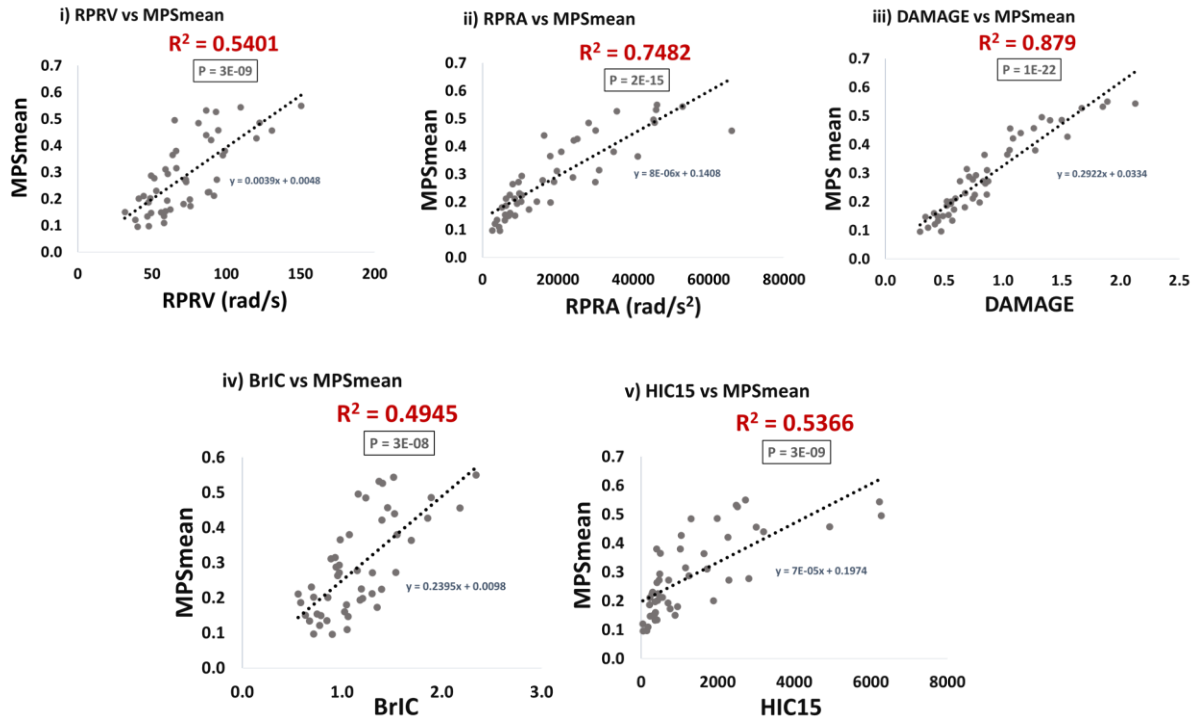


**Figure 2-19 Linear Regression analysis i) Peak angular velocity vs. MPSmean ii) Peak angular acceleration vs. MPSmean iii) DAMAGE vs. MPSmean iv) BrIC vs. MPSmean v) HIC15 vs. MPSmean**

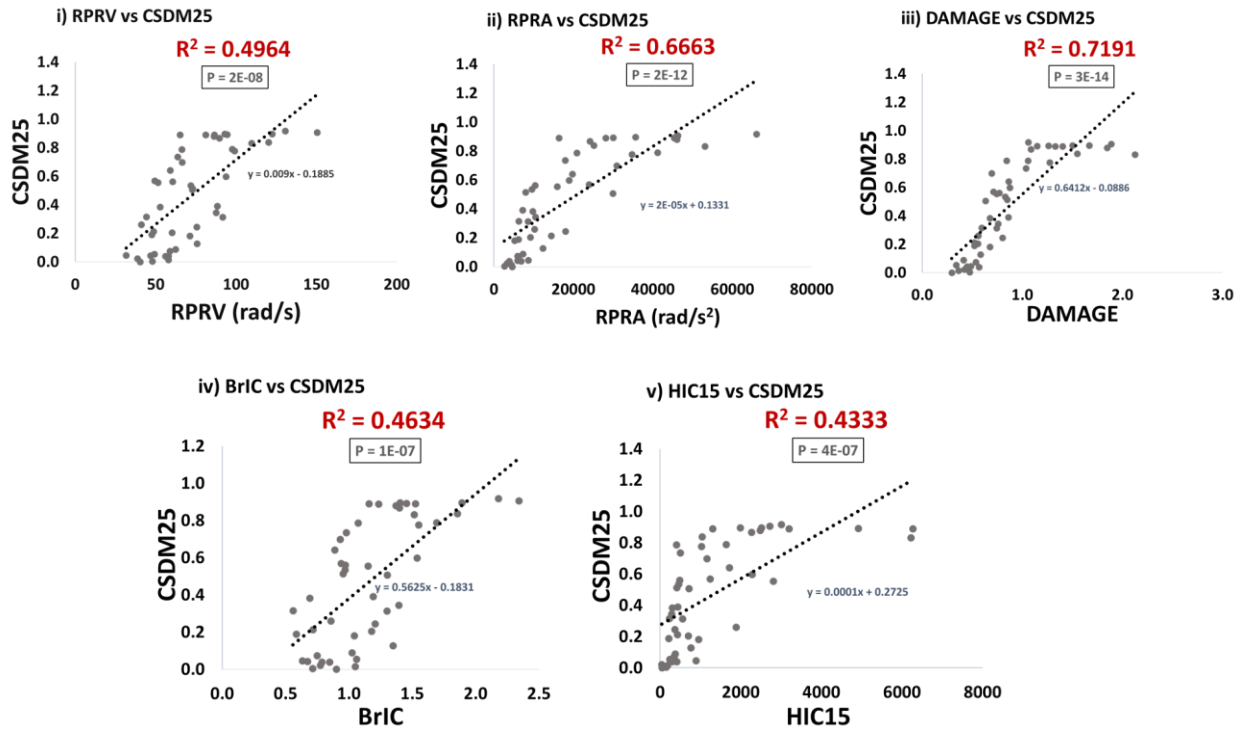


**Figure 2-20 Linear Regression analysis i) Peak angular velocity vs. CSDM25 ii) Peak angular acceleration vs. CSDM25 iii) DAMAGE vs. CSDM25 iv) BrIC vs. CSDM25 v) HIC 15 vs. CSDM25**

### 2.5.6 Influence of skull fracture on intracranial strain response of brain tissue

We investigated the incidence of skull fracture in this section by comparing the Von-Mises stress on the skulls of all pedestrian models at the time of impact to a cut-off value derived from the literature (Figure 2-21). Except for the SUV, all vehicles were within the threshold limit. SUVs induced the highest average skull stress of 102.5 MPa, while mid-sedans had the lowest average skull stress of 73.8 MPa. The pickup truck and the passenger sedan were ranked second and third, respectively.

All models except AF05 had average skull stress greater than the threshold values. 6YO was found to be the most vulnerable pedestrian type with skull stress of 106.2 MPa, while AF05 was found to be the least susceptible with skull stress of 51.5 MPa. The AM50 and AM95 were ranked second and third, respectively.

Additionally, we investigated the relationship between the injury risks associated with a skull fracture and diffuse brain injuries (Figure 2-22). The average male (AM50) and female (AF05) skull stress levels strongly correlated with MPS95 and CSDM25. Figures 2-23 and 2-24 illustrate the contour plot of peak von Mises skull stress in all 48 reconstructed cases.

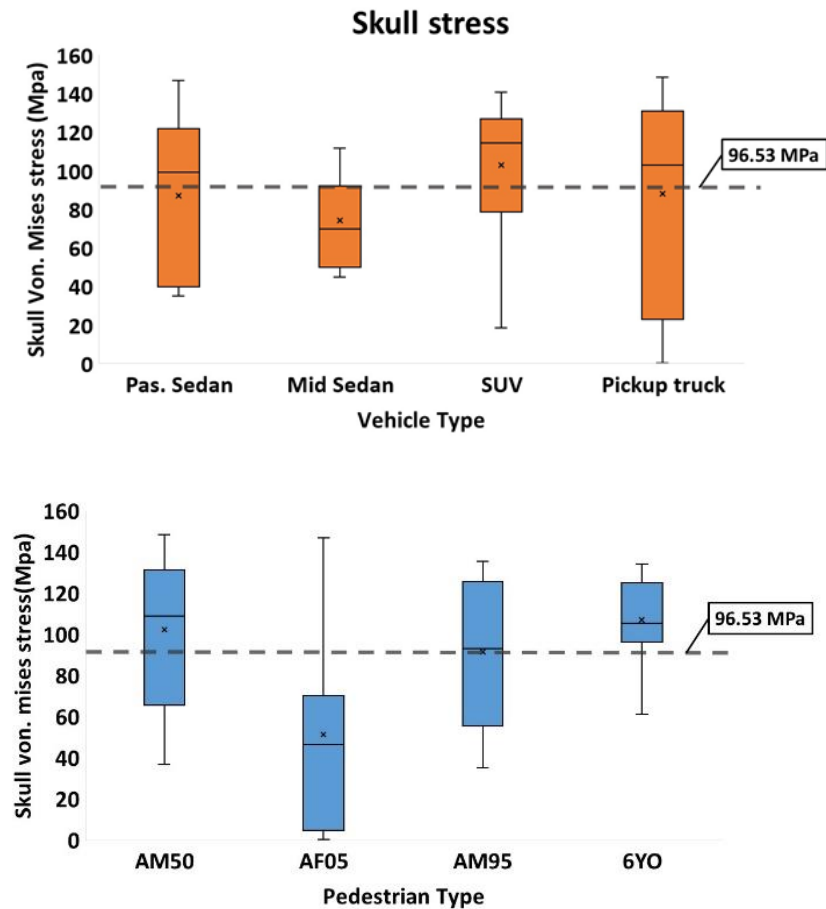


**Figure 2-21 Peak von mises skull stress**

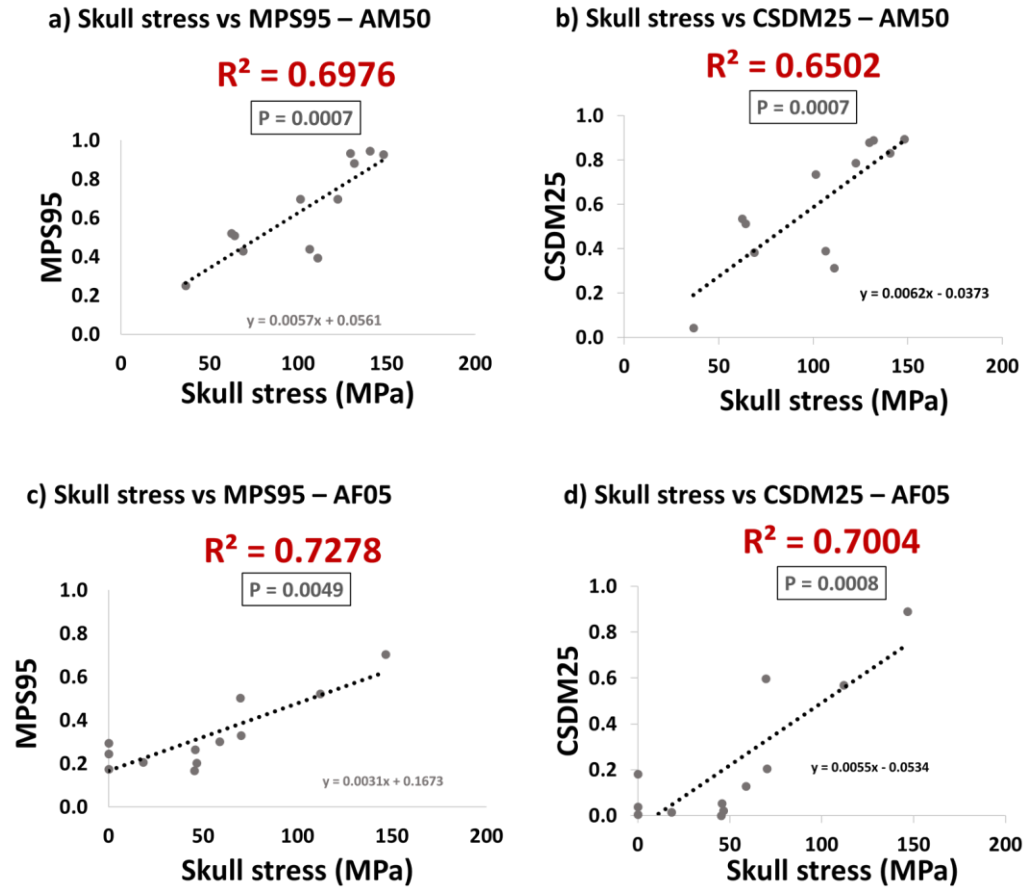


**Figure 2-22 Linear regression analysis a) Skull stress vs MPS95 – AM50 b) Skull stress vs CSDM25 – AM50 c) Skull stress vs MPS95 – AF05 d) Skull stress vs CSDM25 – AF05**

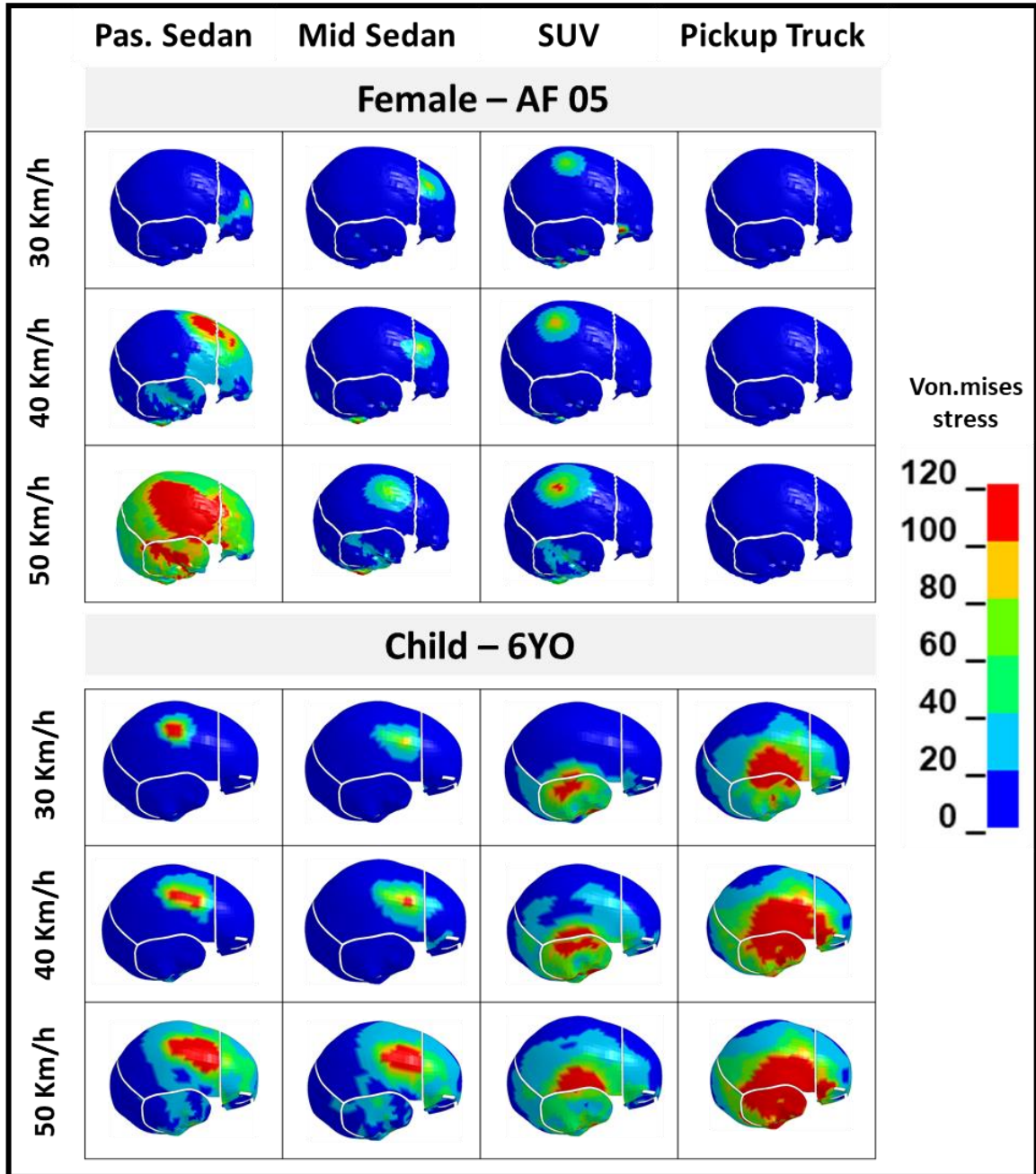


Figure 2-23 Peak Von-Mises skull stress for female AF05 and child 6YO



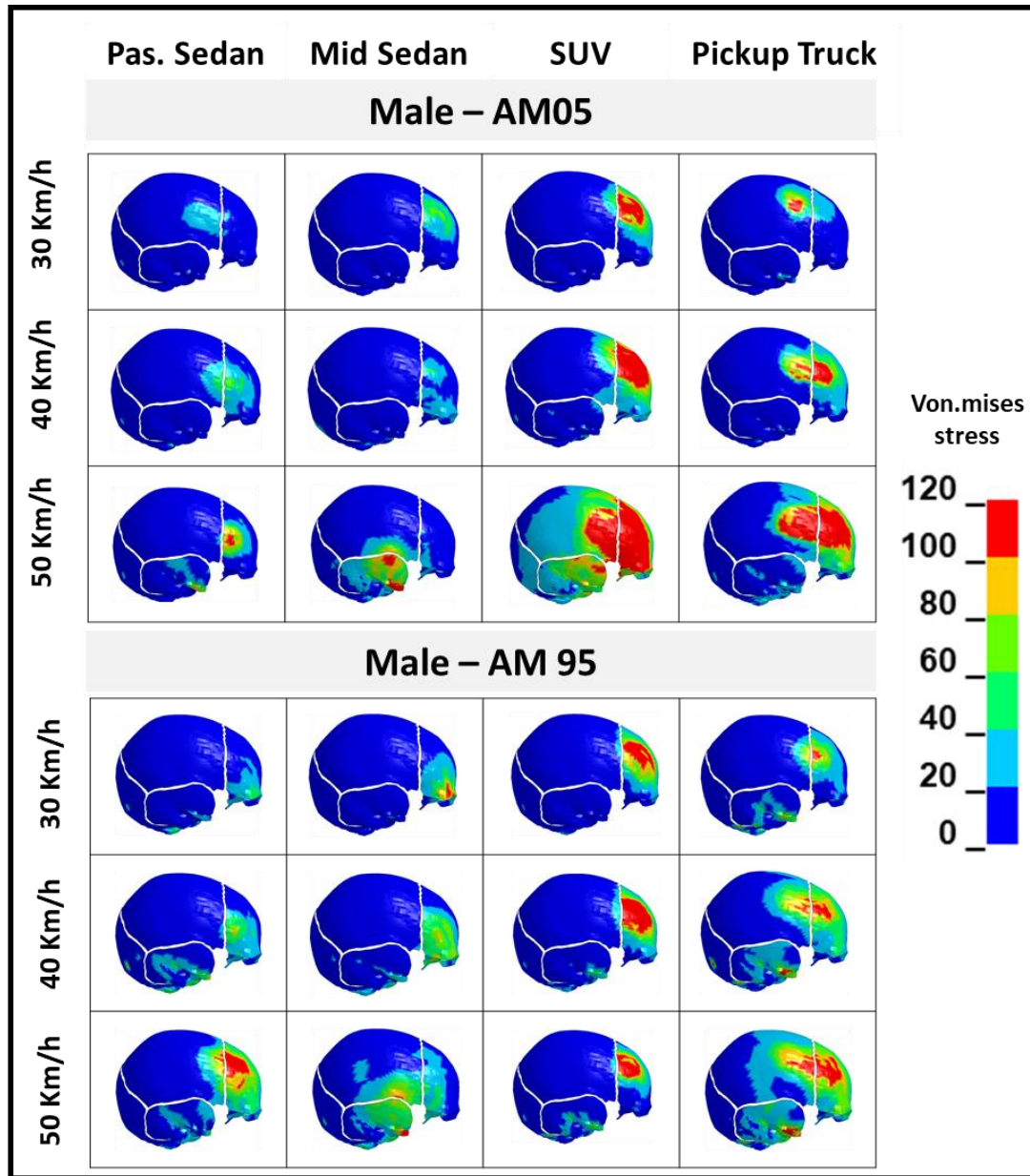


Figure 2-24 Peak Von-Mises skull stress for male AM50 and AM95

## 2.5.7 Influence of vehicle front shape parameters on intracranial strain response of brain tissue

This section studied the relationship between vehicle front shape parameters and intracranial strain response by performing a correlation analysis between vehicle shape parameters (BLEH, BED, BA, and WA) and strain-based injury metrics (MPS95, MPSmean, CSDM15, and CSDM25). Bivariate Pearson and Spearman correlations analysis were performed based on each pedestrian type and varying vehicle front shape using SPSS statistical software. Table 2-5 shows the correlation coefficient ( $r$ ) and two-tailed significance ( $p$ ) of each correlation between shape parameters and strain metrics.

Correlation analysis (Figures 2-25 and 2-26) revealed that for male AM50 and AM95, most of the vehicle shape parameters showed a good correlation. For female and child models, none of the shape parameters showed a significance for intracranial brain strain response. Parameters such as BLEH, WA showed a positive correlation for all strain metrics while BA showed a negative correlation, and BED was found to be least significant for all strain metrics.

For male AM50 and AM95, we performed a linear regression analysis for significant vehicle shape parameters. For average males, BLEH ( $R^2 = 0.77 \pm 0.02$ ,  $P < 0.01$ ) and WA ( $R^2 = 0.71 \pm 0.06$ ,  $P < 0.01$ ) have a strong positive correlation whereas BA ( $R^2 = 0.75 \pm 0.01$ ,  $P < 0.01$ ) shows a strong negative correlation with MPS95 and CSDM25. For large male, BLEH ( $R^2 = 0.58 \pm 0.07$ ,  $P < 0.01$ ) have a moderate positive correlation whereas BA ( $R^2 = 0.59 \pm 0.08$ ,  $P < 0.01$ ) shows a strong negative correlation with MPS95 and CSDM25. In AM95, WA ( $R^2 = 0.32 \pm 0.01$ ,  $P > 0.052$ ) have no significance on MPS95 while low correlation for CSDM25 ( $R^2 = 0.59 \pm 0.08$ ,  $P < 0.01$ ).

**Table 2-5 Pearson and Spearman correlation analysis between vehicle shape parameters and MPS95, MPSmean, CSDM15, CSDM25 A) Male AM50 (N =12) B) Male AM95 (N =12) C) Female AF05 (N =12) A) Child 6YO (N =12)**

**A) Male AM 50 (N=12)**

		<b>MPS95</b>	<b>MPSmean</b>	<b>CSDM15</b>	<b>CSDM25</b>
<b>BLEH</b>	Pearson Correlation (r)	0.878	0.864	0.693	0.872
	Sig. 2-tailed (p)	0.000	0.000	0.012	0.000
	Spearman Correlation (r)	0.734	0.756	0.864	0.820
	Sig. 2-tailed (p)	0.007	0.004	0.000	0.001
<b>BED</b>	Pearson Correlation (r)	0.513	0.494	0.608	0.562
	Sig. 2-tailed (p)	0.088	0.103	0.036	0.057
	Spearman Correlation (r)	0.302	0.345	0.561	0.475
	Sig. 2-tailed (p)	0.340	0.271	0.058	0.119
<b>BA</b>	Pearson Correlation (r)	-0.869	-0.855	-0.681	-0.863
	Sig. 2-tailed (p)	0.000	0.000	0.015	0.000
	Spearman Correlation (r)	-0.734	-0.756	-0.864	-0.820
	Sig. 2-tailed (p)	0.007	0.004	0.000	0.001
<b>WA</b>	Pearson Correlation (r)	0.844	0.851	0.620	0.812
	Sig. 2-tailed (p)	0.001	0.000	0.031	0.001
	Spearman Correlation (r)	0.842	0.864	0.799	0.756
	Sig. 2-tailed (p)	0.001	0.000	0.002	0.004

**B) Male AM 95 (N=12)**

		<b>MPS95</b>	<b>MPSmean</b>	<b>CSDM15</b>	<b>CSDM25</b>
<b>BLEH</b>	Pearson Correlation (r)	0.766	0.746	0.724	0.708
	Sig. 2-tailed (p)	0.004	0.005	0.008	0.010
	Spearman Correlation (r)	0.713	0.605	0.669	0.605
	Sig. 2-tailed (p)	0.009	0.037	0.017	0.037
<b>BED</b>	Pearson Correlation (r)	0.455	0.436	0.368	0.378
	Sig. 2-tailed (p)	0.137	0.156	0.240	0.226
	Spearman Correlation (r)	0.389	0.302	0.367	0.302
	Sig. 2-tailed (p)	0.212	0.340	0.241	0.340
<b>BA</b>	Pearson Correlation (r)	-0.772	-0.752	-0.730	-0.715
	Sig. 2-tailed (p)	0.003	0.005	0.007	0.009
	Spearman Correlation (r)	-0.713	-0.605	-0.669	-0.605
	Sig. 2-tailed (p)	0.009	0.037	0.017	0.037

<b>WA</b>	Pearson Correlation (r)	0.572	0.551	0.572	0.530
	Sig. 2-tailed (p)	0.052	0.064	0.052	0.076
	Spearman Correlation (r)	0.605	0.497	0.540	0.497
	Sig. 2-tailed (p)	0.037	0.101	0.070	0.101

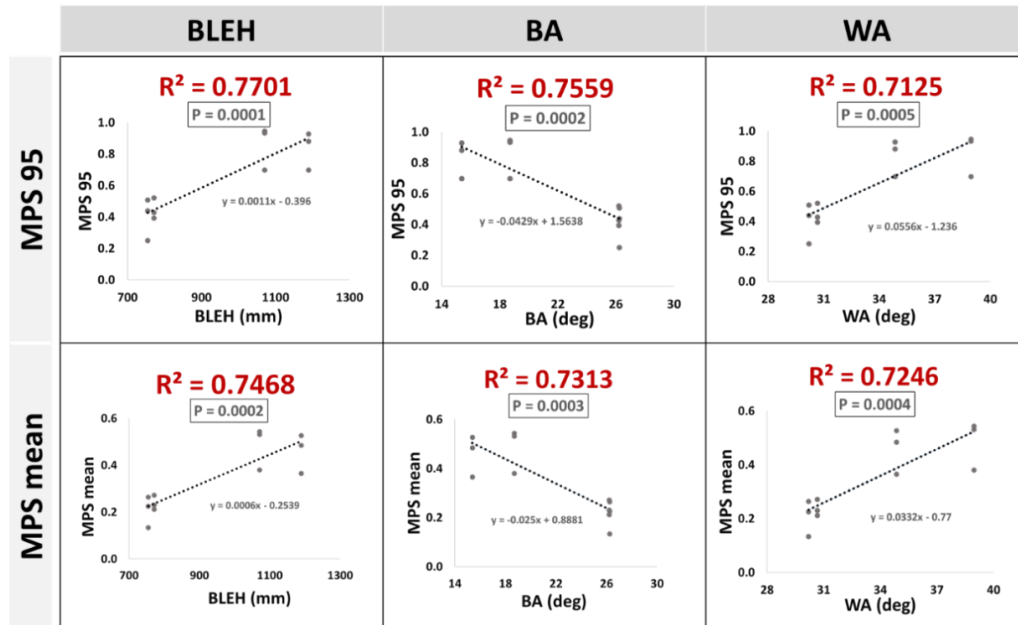
### C) Female AF 05 (N=12)

		<b>MPS95</b>	<b>MPSmean</b>	<b>CSDM15</b>	<b>CSDM25</b>
<b>BLEH</b>	Pearson Correlation (r)	-0.304	-0.327	-0.212	-0.286
	Sig. 2-tailed (p)	0.337	0.299	0.508	0.368
	Spearman Correlation (r)	-0.324	-0.345	-0.389	-0.302
	Sig. 2-tailed (p)	0.304	0.271	0.212	0.340
<b>BED</b>	Pearson Correlation (r)	-0.562	-0.549	-0.397	-0.558
	Sig. 2-tailed (p)	0.057	0.064	0.201	0.060
	Spearman Correlation (r)	-0.453	-0.432	-0.453	-0.410
	Sig. 2-tailed (p)	0.139	0.161	0.139	0.185
<b>BA</b>	Pearson Correlation (r)	0.294	0.315	0.207	0.275
	Sig. 2-tailed (p)	0.354	0.319	0.518	0.387
	Spearman Correlation (r)	0.324	0.345	0.389	0.302
	Sig. 2-tailed (p)	0.304	0.271	0.212	0.340
<b>WA</b>	Pearson Correlation (r)	-0.157	-0.220	-0.074	-0.144
	Sig. 2-tailed (p)	0.625	0.491	0.820	0.656
	Spearman Correlation (r)	-0.151	-0.238	-0.259	-0.173
	Sig. 2-tailed (p)	0.639	0.457	0.416	0.591

### D) Child 6YO (N=12)

		<b>MPS95</b>	<b>MPSmean</b>	<b>CSDM15</b>	<b>CSDM25</b>
<b>BLEH</b>	Pearson Correlation (r)	-0.462	-0.458	-0.330	-0.382
	Sig. 2-tailed (p)	0.131	0.135	0.295	0.221
	Spearman Correlation (r)	-0.518	-0.475	-0.324	-0.389
	Sig. 2-tailed (p)	0.084	0.119	0.304	0.212
<b>BED</b>	Pearson Correlation (r)	-0.532	-0.532	-0.525	-0.502
	Sig. 2-tailed (p)	0.075	0.075	0.080	0.096
	Spearman Correlation (r)	-0.518	-0.497	-0.518	-0.518
	Sig. 2-tailed (p)	0.084	0.101	0.084	0.084
<b>BA</b>	Pearson Correlation (r)	0.468	0.463	0.341	0.392
	Sig. 2-tailed (p)	0.125	0.130	0.278	0.208

	Spearman Correlation (r)	0.518	0.475	0.324	0.389
	Sig. 2-tailed (p)	0.084	0.119	0.304	0.212
WA	Pearson Correlation (r)	-0.147	-0.160	0.063	-0.023
	Sig. 2-tailed (p)	0.648	0.620	0.846	0.944
	Spearman Correlation (r)	-0.238	-0.216	0.086	-0.065
	Sig. 2-tailed (p)	0.457	0.500	0.790	0.841



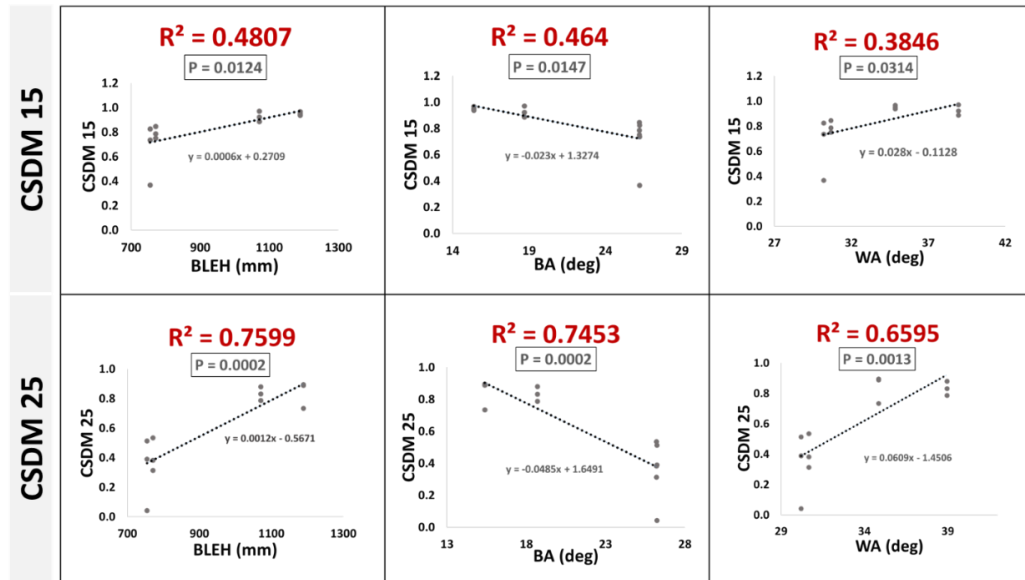
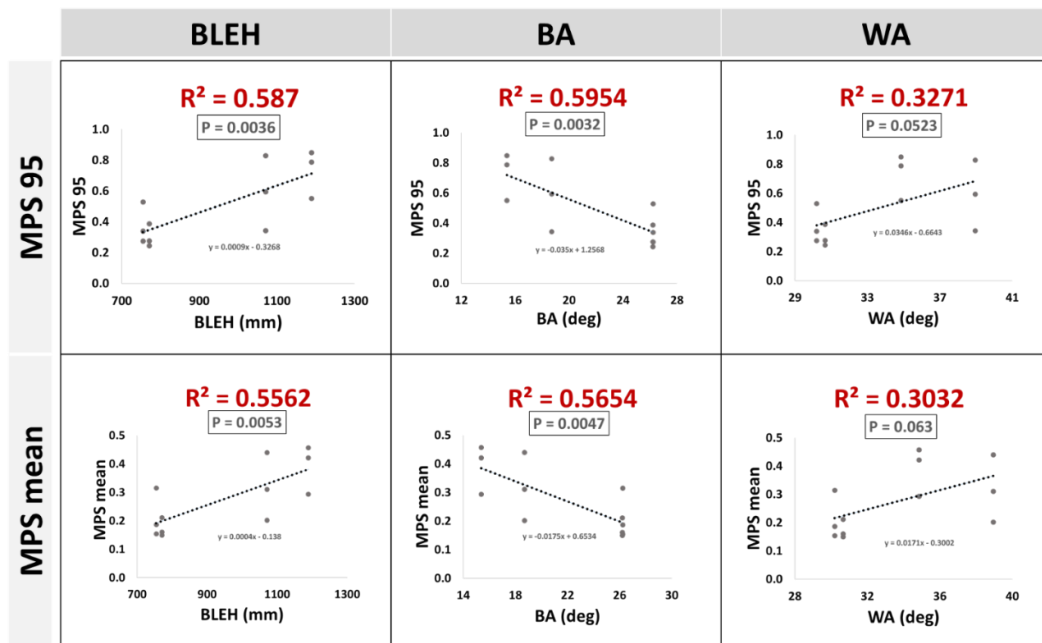
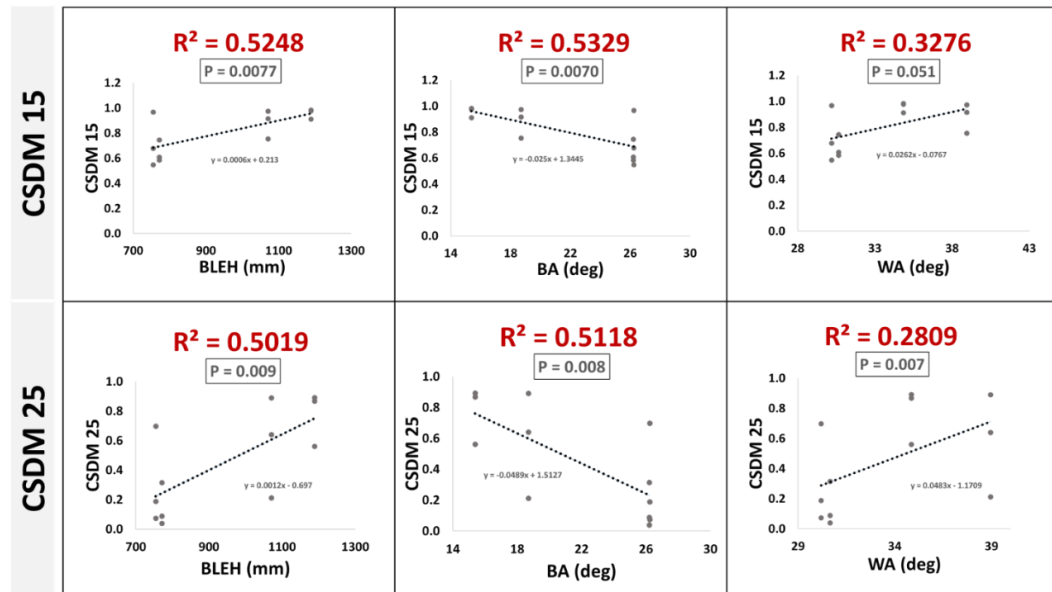


Figure 2-25 Linear regression analysis between vehicle shape parameters (BLEH, BA, and WA) and brain strain metrics (MPS95, MPSmean, CSDM15, and CSDM25) for males (AM50).



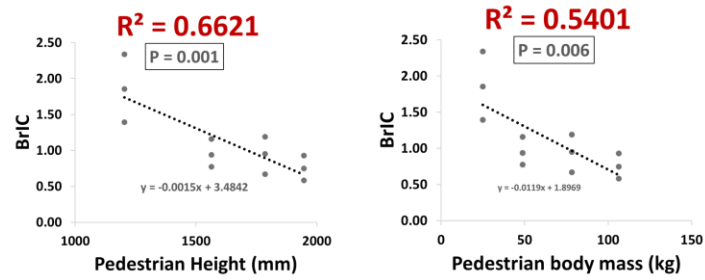


**Figure 2-26 Linear regression analysis between vehicle shape parameter (BLEH, BA, and WA) and brain strain metrics (MPS95, MPSmean, CSDM15, and CSDM25) for males (AM 95)**

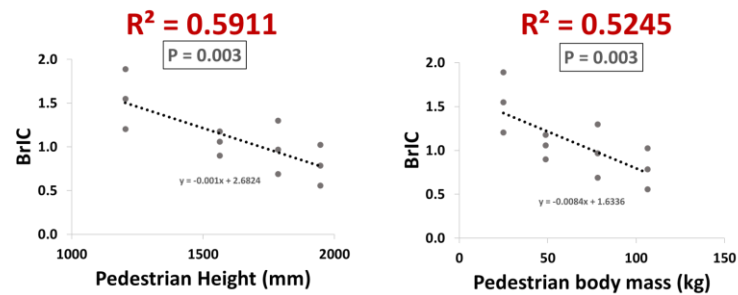
### 2.5.8 Influence of pedestrian body size on head kinematic

The relationship of pedestrian body mass and height with head kinematics and brain strain response based on vehicle types was investigated in this section. Only BrIC was found to be correlated with pedestrian height and body mass (Figure 2-27). Height and body size have a better correlation with BrIC in subcompact passenger sedans than other vehicles. We found that sedans have a better correlation than SUVs and pickup trucks. Furthermore, in pick trucks, pedestrian height has shown no correlation with BrIC.

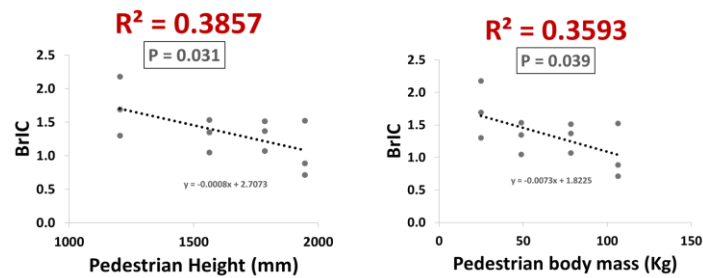
## a) Sub compact passenger sedan



## b) Mid-size sedan



## c) SUV



## d) Pickup truck

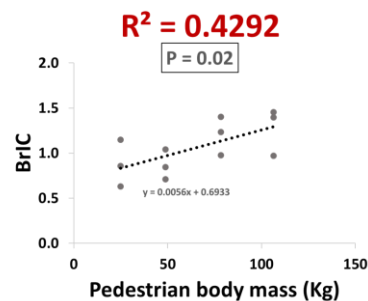


Figure 2-27 Linear regression analysis BrIC vs pedestrian height and mass – a) Subcompact passenger sedan b) Mid-size sedan c) Sports Utility Vehicle (SUV) d) Pickup truck



## 2.6 Discussion

### 2.6.1 The effect of vehicle shape parameters, pedestrian height, and weight on pedestrian head rotation and diffuse brain injuries

Our results indicate those vehicle shape parameters such as BLEH, BA, and WA were significant for TBI risks. The correlation and regression analysis (Section 2.5.7) found that BLEH and WA correlated positively and BA negatively with MPS and CSDM for average males. Large males (AM95) have also demonstrated a middling correlation of BLEH and BA in a similar trend but with a lower significance of WA. In contrast to other head injuries, Li et al. found that concussions occur independently and statistically significantly with BLEH. When limiting the primary head contact location within the windshield area, they hypothesized that increasing BLEH by 1cm reduces 17% of the risk of concussion [12]. Though this contradicts our finding, it is most likely because a higher BLEH reduces upper body and head rotation [5, 6, 24, 26, 27]. Hence, the effect of BLEH on the risk of concussion from windshield impact in males was first investigated in this study.

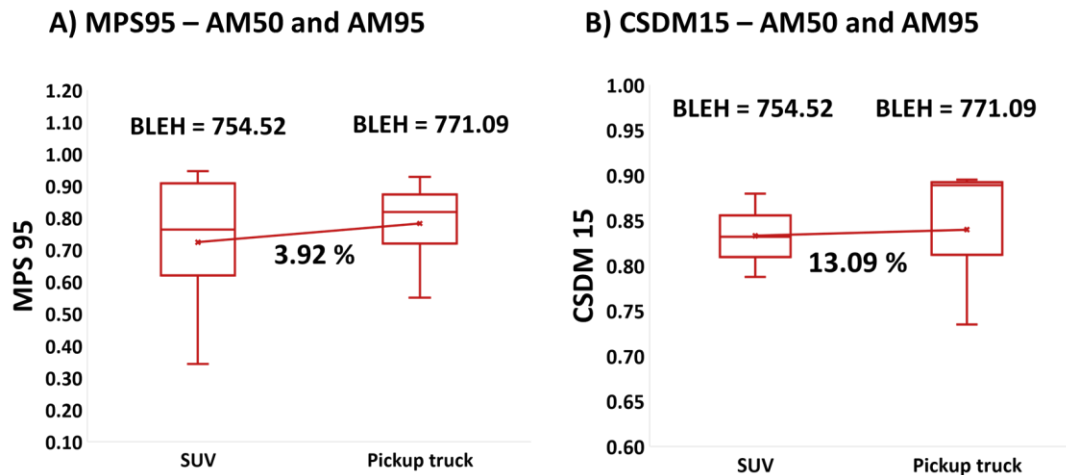


**Figure 2-28 Distribution of MPS95 and CSDM 15 for windshield impacts a) MPS95 for male (AM50 and AM95) b) CSDM15 for male (AM50 and AM95) in sedans**

Our findings (Figure 2-28) indicate that increasing the BLEH by 16 mm decreased the average MPS95 by 3.92 percent and the CSDM15 by 13.09 percent in males (AM50 and

AM95). As a result, increasing BLEH reduces the risk of concussion during a windshield impact in a sedan.

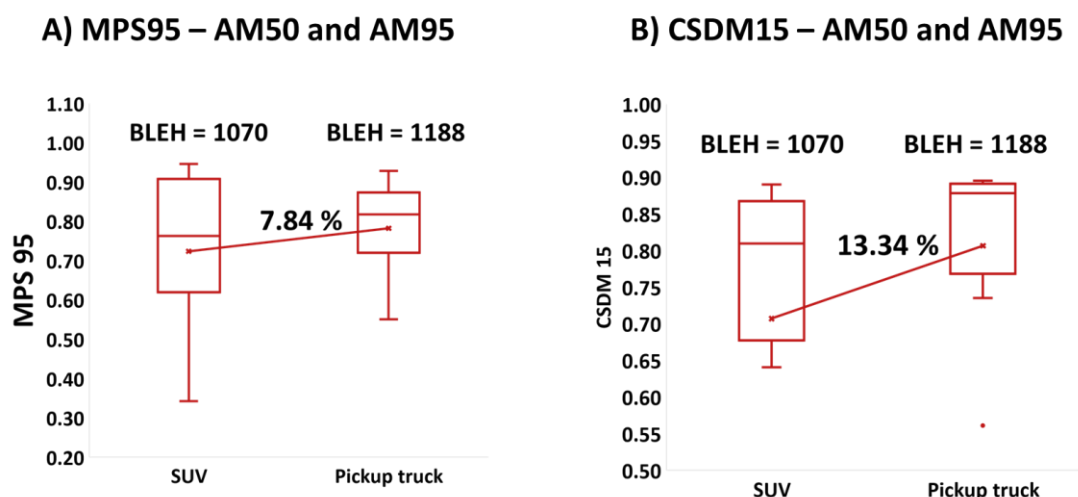


**Figure 2-29 Distribution of MPS95 and CSDM 15 for hood impacts a) MPS95 for male (AM50 and AM95) b) CSDM15 for male (AM50 and AM95) in SUV and pickup trucks**

Alternatively, a difference of 118 mm increase in BLEH between SUVs and pickup trucks increased the average MPS95 (7.85%) and CSDM15 (13.34%) values for males in hood impacts (Figure 2-29). Thus, increasing BLEH does not mitigate the risk of concussion in hood impacts with a high leading edge.

Peak angular acceleration strongly correlated with average MPS and CSDM25 than peak angular velocity. Moreover, consistent with previous studies [9, 12], none of the vehicle shape parameters significantly influenced pedestrian linear and rotational head kinematics.

While pedestrian height and body mass negatively correlated with BrIC. (Section 2.5.8) Previous studies [76, 77, 105] have also shown that increasing pedestrian height decreases head injuries. Surprisingly, as the BLEH increase, the level of correlation between BrIC and body mass and height decreases. Another study has found that when the pedestrian's shoulder collides with the stiffer hood of a vehicle (SUV and Pickup trucks) of high BLEH, the head's translational motion is significantly transformed into

angular motion a high angular velocity [63]. As a result, the shoulder contact force in high-leading-edged vehicles is more significant on head rotation than pedestrian body size. However, upper body rotation during the impact with the leading bonnet edge in sedans plays a vital role in the head rotation. Our finding implies that as BLEH increases, the influence of pedestrian body size on head rotation decreases.

## 2.6.2 The effect of bonnet leading-edge height and bonnet angle on the severity of AIS 4+ head injuries

Vehicles with high BLEH and low BA were most susceptible to AIS 4+ head injury, both in terms of focal and diffuse brain injuries. This was found to be consistent with previous findings [86-90], which found that pedestrians of all ages struck by SUVs and light trucks suffered more severe head injuries than pedestrians struck by passenger vehicles. Guibing et al. also suggested that a higher BLEH resulted in a higher risk of head injury for adults [11]. The primary difference in pedestrian kinematics can be attributed to this in general. According to Section 2.5.1, in high BLEH vehicles (SUVs and Pickup trucks), the adult pedestrian's mid-body region was directly struck, engaging the body more fully with stiff structure and allowing less upper body rotation. As a result, the pedestrian's linear momentum increases, allowing the shoulder to collide with the hood before the head [106]. In a sedan, however, the pedestrian's upper body was rotated and wrapped around the bonnet. The head impacted the windshield or the rear hood end, depending on the pedestrian's height. In children, the shoulder was firmly pressed against the front grills and the head collided with the leading edge of the vehicle in SUVs and pickup trucks, resulting in a concentrated force to the side of the head; in sedans, comparable to adults, the upper body wraps around the leading edge of the vehicle, and the head impacted the top surface of the hood [79]. As a result of the short duration of the impact, the lack of upper body rotation, and the inability to wrap around the bonnet, pedestrians of all ages are at risk of severe head injuries. Thus, due to the short duration of the impact, the lack of upper body rotation, and the inability to wrap around the bonnet, vehicles with high BLEH are vulnerable to severe head injury risk for pedestrians of all age groups.

Our results (Sections 2.52, 2.53 and 2.54) indicate that average HIC (>1500), BrIC (> 1), and MPS (> 0.82) values were significantly high, leading to the AIS 4+ focal and diffuse

head injuries for SUV and pickup trucks. A recent study revealed that BLEH had the most significant effect on HIC values, while bonnet angle had a significant effect on head angular acceleration [78]. However, contact force with a stiffer hood could be a factor; neck tension is important in the linear head kinematics of an adult pedestrian in a high BLEH vehicle collision [83]. A previous study found that HIC values are higher for SUV and pickup trucks due to high neck tension than high contact forces with the hood [107]. According to Section 2.5.6, the incidence of skull fracture was more increased in 6YO due to the high concentrated linear force resulting from impact with the vehicle's leading edge. Besides, bonnet angle and high BLEH influence shoulder contact force, which played a significant role in intracranial brain strain generation for both adults and children. Previous research identified that when an adult's shoulder collides with the hood surface, translational movement of the head converts to angular motion, resulting in the generation of tensile forces near the spinal cord, which increases the head's angular velocity and principal strain generation in the brain [63]. While for children, the shoulder was pressed against the bumper grill, causing rapid head rotation, resulting in higher angular acceleration and brain strains than adults [79].

### 2.6.3 Injury severity between SUV and pickup trucks

Even though pickup trucks have a higher bonnet leading edge, greater mass, and pedestrian kinematics similar to SUVs, head injury severity was higher in SUVs than in pickup trucks. This was found to be inconsistent with the previous studies. According to Sections 2.5.3 and 2.5.4, pickup trucks predicted lower BrIC, MPS95, and CSDM values than SUVs due to the inner hood structure's difference in design and shape. Previous studies have found that adding a hollow space between the hood support and the skin and reinforcing a flexible and ductile structure under the hood significantly reduces pedestrian head injuries [108-110]. Hood adhesive pads in pickup trucks (Figure 2-30) created a uniform extra hollow space between the bonnet and inner hood, which aided in better energy absorption during shoulder and head impact. As a result of the reduced shoulder contact force, angular head motion and intracranial brain strains were reduced in pickup trucks [63]. Besides, for the 6YO model, both the head and shoulder impacts the vehicle's soft front grill rather than the vehicle's stiffer leading hood edge (Figure 2-31),

reducing the risk of skull fracture and rotational head injuries [79]. Thus, future research should examine the effect of the hood structure and front bumper on pedestrian head injuries for vehicles with a higher BLEH.



**Figure 2-30 A) Inner hood structure with hood adhesive pads in pickup truck B) Inner hood structure in SUV**

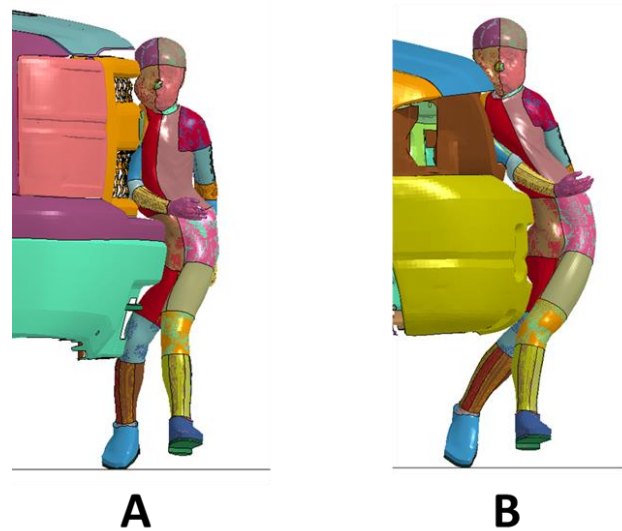


**Figure 2-31 A) 6YO collision with Pickup trucks – head-to-front-grill b) 6YO collision with SUVs– head-to-front-grill**

#### 2.6.4 Influence of skull fracture on the intracranial strain response of brain tissue

In this study, the interrelationship between the incidence of skull fracture and diffuse brain injuries such as DAI and concussion was quantified. Our results (Section 2.5.6) indicate that average male (AM50) and small female (AF05) peak skull stresses had a good correlation with the MPS95 and CSDM25. This implies that skull fracture significantly increases the risk of diffuse brain injuries. Using three different (AM50, AM95, and AF05) THUMS pedestrian models and three distinct vehicle front shapes, Watanabe et al. have concluded that the injury risk of skull fracture and DAI do not correlate with each other [85]. This was found to be not in line with our results. However, they have considered two-vehicle impact locations (Centre and Corner) and four impact speeds, including 20 km/h. A recent study on blunt head impact found that the risk of DAI significantly rises after skull fracture at higher head impact velocity [111]. Additionally, during a collision with a pickup truck, the female model's head did not contact the vehicle. (Figure 2-23). Thus, the relationship between skull fracture and diffuse brain injuries during vehicle contact remains debatable and needs further investigation across different impact scenarios and low impact speed.

### 2.7 Conclusion

We comprehensively analyzed the effect of vehicle front shape parameters and pedestrian body sizes on the risk of TBIs across a broad population. Parameters such as BLEH, BA, and WA were statistically significant for pedestrians' TBI risk. Injury risk of skull fracture and AIS2+ diffuse brain injuries were related to each other. Vehicles with a high BLEH and a low BA were at an increased risk of AIS 4+ head injuries. The height and weight of the pedestrian have a significant effect on the pedestrian's head rotation. Increased BLEH decreases the risk of mild TBIs involved in windshield collisions. Increased BLEH in SUVs and pickup trucks, on the other hand, increases the risk of severe AIS 4+ head injuries. Thus, BLEH is a significant risk factor for pedestrian TBI and should be appropriately evaluated when optimizing vehicle front design for pedestrian protection.

## Chapter 3

### 3 Investigating pedestrian gait postures' influence on dynamic head and intracranial strain response of average 50th percentile males in car-to-pedestrian collisions (CPCs).

This chapter is co-authored by Dr Haojie Mao

#### 3.1 Abstract

*In real-world collisions, the pedestrian's pre-impact initial conditions are highly variable. The influence of pedestrian gait posture on pedestrian head impact kinematics in car-to-pedestrian collisions (CPC) has been studied in the past. The effect of pre-impact gaits on dynamic head response and brain strain, on the other hand, has yet to be investigated. The purpose of this study was to use a computational approach to understand the dynamic head and intracranial strain response based on different pre-impact gait postures. The upper body kinematics of the Hybrid III average 50th male pedestrian FE dummy were validated using seven mid sedan vehicle-to-PMHS test data. A total of 90 CPC cases were reconstructed using a mid-sedan vehicle model and a Hybrid III dummy in 30 different gait postures in three different gaits (walking, running, and emergency) and three different impact speeds (20, 30, and 40 km/h). Then, head-to-vehicle impacts were reconstructed by prescribed head-only motion using isolated THUMS (Ver. 4.02) FE head. For all simulation results from all reconstructed cases, six head injury criteria were calculated. Our findings show that the risk of pedestrian head injuries varies depending on gait percentage in both the same and different gait types. Walking and emergency gait postures dominate linear head kinematics with a high HIC score, whereas running gait posture dominates for pedestrian head rotation, resulting in higher brain strains. Peak rotational head velocity ( $R^2 = 0.65 \pm 0.05$ ,  $P < 0.01$ ), rather than peak rotational head acceleration ( $R^2 = 0.56 \pm 0.04$ ,  $P < 0.01$ ), was strongly correlated with brain strain. Linear head kinematics varies significantly between the stance and swing phase in walking and running gaits whereas rotational head kinematics and brain strains vary cyclically across gait percentages in all three gaits.*

## 3.2 Introduction

Nearly 1.35 million people die every year from road traffic accidents (RTAs) [1]. According to the Governors Highway Safety Association, pedestrian fatalities in the United States increased by 5% in 2019 over the previous year. Notably, the fatality rate increased by a record 21 percent in the first half of 2020. Although few people were on the road due to the COVID-19 pandemic, 2020 saw the most significant annual increase in pedestrian fatalities per mile driven since the mid-1970s [16]. To ensure effective countermeasures, a thorough understanding of the complex interaction between the pedestrian and the vehicle is required.

In road traffic accidents (RTAs), head injuries are the most common cause of death and disability for a long time [2-4, 7, 17, 18]. The effect of pedestrian pre-impact kinematics on post-impact kinematics has been demonstrated in previous studies [67, 112], and kinematics of a collision are known to be affected by the pedestrian's stance at the time of impact. Moreover, the severity of head injuries may also be influenced by pedestrian orientation [67].

The initial posture of the pedestrian has a significant impact on pedestrian kinematics and injury outcomes [113, 114]. The kinematics of the pedestrian head is determined by the initial contact between the vehicle's front end and the pedestrian legs. Furthermore, the pedestrian gait significantly impacts head impact orientation at the time of contact with the vehicle [115]. This is because the pedestrian's center of gravity changes as their gait posture changes, resulting in different stress points on the pedestrian's head [116].

Several studies [10, 117-119] have found that pedestrian gaits significantly affect pedestrian injury, with almost all studies based on 10 walking gaits reported by Untaroiu et al. [120]. As a result, because there is a distinct difference between running and walking gaits, running gaits were developed based on child pedestrians [121]. Both walking and running gaits have a character of symmetry [120]. Furthermore, Zou et al. claimed that pedestrians would consciously do something to avoid the collision and proposed emergency gaits after analyzing over 1000 vehicle-to-pedestrian collision



videos. They also observed that the proportions of walking, running, and emergency for sedan impact were 45 %, 26 %, and 29 %, respectively [13].

Multi-body pedestrian models have been used in several studies to analyze the effects of pedestrian stance on a pedestrian head injury during vehicle-pedestrian collisions.

Anderson et al. used the MADYMO pedestrian model and revealed that the pedestrian stance affects the HIC and peak head acceleration [114]. Another study used PC-Crash to claim that the risk of pedestrian injury varies depending on gait posture in the same and different gait serials [13]. The effect of pedestrian speed, gait, and transverse translation of the pedestrian's head and head rotation was studied quantitatively by Elliot et al. [117]. As a result, most research has focused on the risk of pedestrian head injury based on head kinematic response. However, no previous study has examined how pedestrian gait affects dynamic head response and intracranial brain strain response.

Furthermore, all numerical reconstruction studies [94, 111] [117] used multi-body pedestrian models in the past literature. One study has used a FE pedestrian model to analyze pedestrian gait and posture. Using the full-scale Global Human Body Models Consortium (GHBMC) male (AM50) pedestrian model, Pak et al. found that pedestrian pre-impact walking postures have a significant impact on head impact regions, resulting in different stress points on the head [14]. Despite this, no previous research has looked into the brain response and tissue level deformation using the FE pedestrian model. Therefore, the main objective of this study was to understand the effect of different pedestrian pre-impact gait postures on dynamic head and brain strain responses during vehicle impacts in car-to-pedestrian collisions (CPCs) using kinematic and tissue-level strain-based head injury criteria.

## 3.3 Methods

### 3.3.1 Pedestrian Dummy Finite element model

Hybrid III – 50th percentile male standing FE model developed by Livermore Software Technology Corporation (LSTC) was used in this study [122]. (Figure 3-1) This model was developed based on the LSTC Hybrid III 50th percentile occupant rigid FE model. Most of the model components were rigid, and only body parts such as head, arms, leg,

chest, and ribs were modeled as deformable. Unlike the human body FE model, all dummy parts were connected using FE joint (translational, revolute, and spherical) definitions, thus facilitating better posture and gait adjustment. However, this model was not validated due to the lack of test data; only a preliminary version was released for experimental purposes [123]. Table 3-1 illustrates the body mass, stance, and center of gravity (C.G) from the ground of the released Hybrid III pedestrian dummy by LSTC.



**Figure 3-1 Hybrid III – 50<sup>th</sup> percentile male pedestrian dummy**

**Table 3-1 Body mass, stance, and center of gravity (C.G) from the ground of all pedestrian FE model**

Body Mass (kg)	78.04
Stature (mm)	1682
Center of Gravity (mm)	920

### 3.3.2 Anthropometry of Hybrid III

The anthropometry of the Hybrid III dummy was validated against different anthropometric databases and model data from past literature. On comparing the stature of the Hybrid III dummy against the ANSUR (The Anthropometric survey of US personnel) data [124, 125], the HIII dummy model was found to be shorter (~ 75 mm) than the stature of the average 50th percentile male. Figure 3-2 illustrates the comparison of the stature of HIII against the overall distribution of male stature in percentiles from ANSUR I and ANSUR II measurement data.

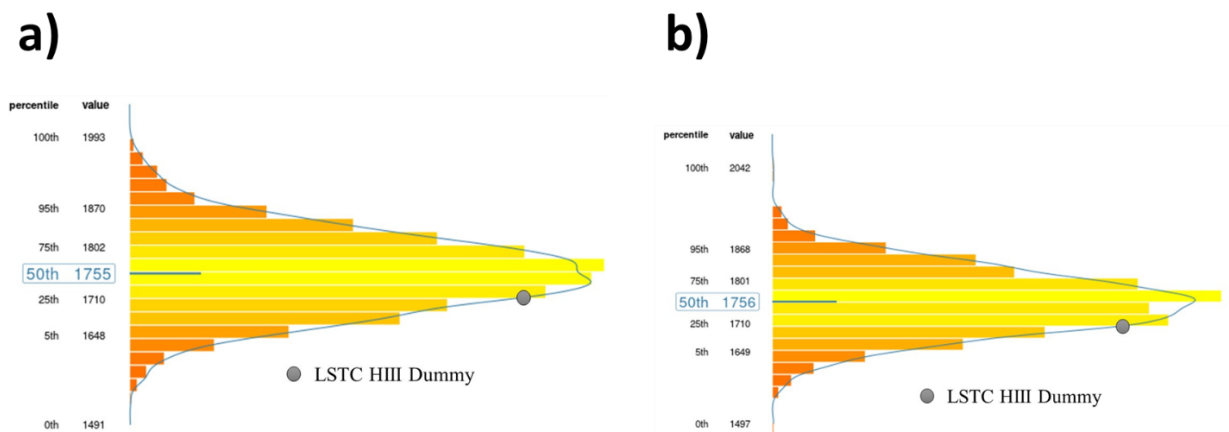


**Figure 3-2 Population distribution of stature from a) ANSUR I database b) ANSUR II database**

To encounter this difference in stature, anthropometric dimensions of the LSTC HIII dummy in specific anatomical directions were needed to be examined with corresponding ANSUR data. Anthropometric measures such as cervical height A, Iliocristale height B, Vertical thumb tip reach down C, Knee height D, Buttock depth E, Chest depth F, Head breadth G, Waist breadth H, Bideltoid breadth I, and stature J were considered [126]. (Figure 3-3). Table 3-2 describes the percentage difference of different anthropometric measures of HIII from ANSUR I and II data. Most of the measures were found to be less than a 5% deviation. Cervical height A, Knee height D, and Waist breadth H measures were more than 5% difference from the ANSUR data. In addition, the stature of HIII was shorter when compared with pedestrian dummies (Polar II [127], Army Mannequin

ProV8 software [124]) from past literature and current databases such as NHANES (The National Health and Nutrition Examination Survey) [128, 129]). (Figure 3-4) As a result, the HIII dummy requires scaling to match the anthropometric measures of the male 50<sup>th</sup> percentile.

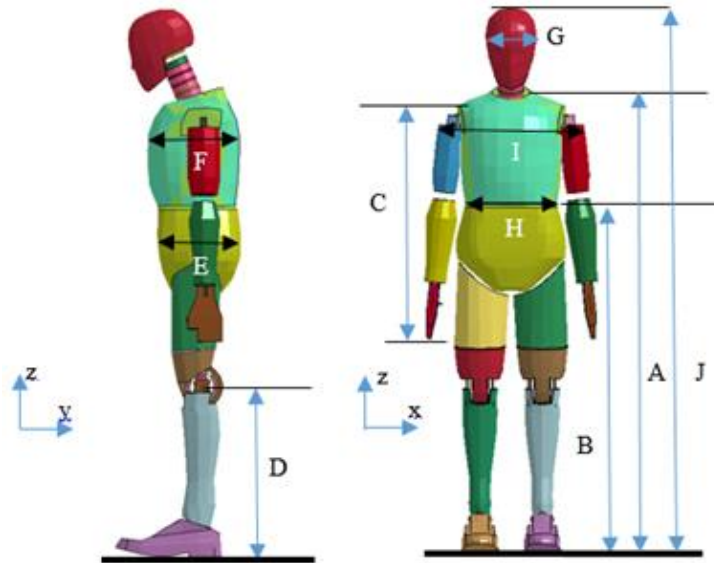


**Figure 3-3 Anthropometric measurements A) Cervical height B) Iliocristale height C) Vertical thumb tip reach down D) Knee height E) Buttock height F) Chest depth G) Head breadth H) Waist breadth I) Bideltoid breadth J) Stature**

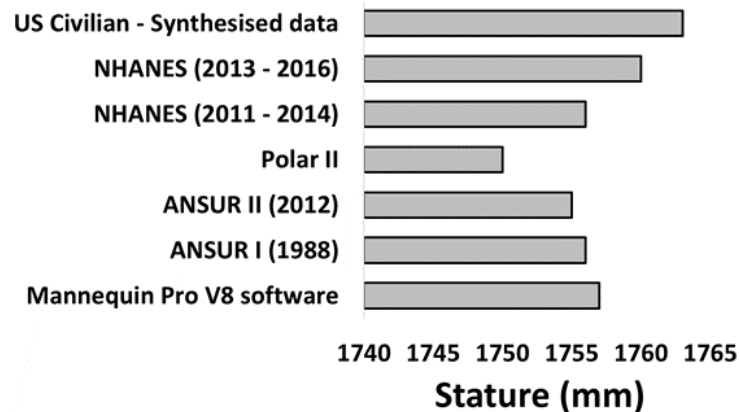


**Figure 3-4 Comparison of the stature of the pedestrian dummies in the past literature**

**Table 3-2 Percentage difference of anthropometric measurements between Hybrid III and ANSUR I & II data.**

<b>Anthropometric Dimensions</b>	<b>LSTC (mm)</b>	<b>ANSUR I (mm)</b>	<b>% difference</b>	<b>ANSUR II (mm)</b>	<b>% difference</b>
Cervical Height A	1414	1518	6.851	1517	6.790
Iliocristale Height B	1066	1072	0.560	1061	-0.471
Thumb tip reach down C	803	800	-0.375	811	0.986
Knee height D	524	557	5.925	553	5.244
Buttock depth E	255	248	-2.823	246	-3.659
Chest depth F	263	252	-4.365	253	-3.953
Head breadth G	157	152	-3.289	154	-1.948
Waist breadth H	289	307	5.863	325	11.077
Bideltoid breadth I	476	491	3.055	509	6.483
Stature J	1682	1757	4.269	1755	4.160

Besides, the overall mass and mass distribution of each body segment of the HIII dummy was also examined. Databases such as AMVO [130], Army Mannequin Pro V8 [124] software and model data from DTIC (Defense Technical Information Center) Hybrid III standing manikin [131], Hybrid III occupant model data from NHTSA, pedestrian crash dummies from leading manufacturers such as Humanetics, JASTI & ESAC.inc were taken as reference. Figure 3-5 illustrates the mass distribution of different databases and model data with LSTC HIII FE Dummy. There is a slight difference in the mass distribution of the upper and lower torso due to the variation in the mass calculation of lumber joints in different databases. Overall, there is no deviation in the body mass and mass distribution of all body segments of the HIII dummy.

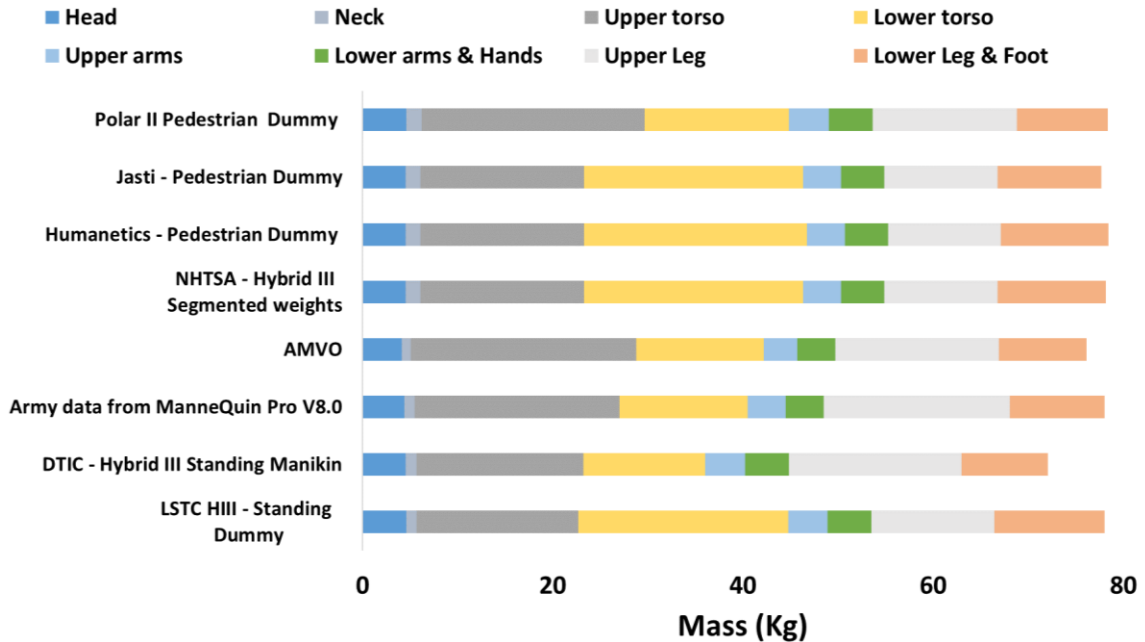


**Figure 3-5 Comparison of body segment mass between different databases**

### 3.3.3 Scaling of Hybrid III

Non-proportional variations in all anatomical directions of the body measurements were found in the ANSUR data [126]. In the case of the HIII dummy, we could also see a deviation in the anthropometric measures in the transverse (x-y) plane (Waist breadth). A complex scaling technique called combination forecasting kriging methods can be adopted with specific scaling factors for each body segment. However, connecting the scaled body parts into a whole scaled dummy will be challenging due to the lack of the joint properties data. Previous studies with global scaling techniques based on mass and height had shown relatively good results and easy implementation [126, 132]. Thus, a similar global scaling technique was adopted to scale the HIII dummy to match with the stature of the average 50<sup>th</sup> percentile male.

The scaling of the HIII model involves three steps.

#### A) Scaling of Geometry

Geometric scaling of the Hybrid III dummy corresponding to the target height was performed in two steps.

- a) Scaling in the vertical direction (z-axis) to match the target stature of 1757mm.

$$\lambda_{z, \text{scaled}} = \frac{H_{\text{target}}}{H_{\text{HIII dummy}}} = \frac{1757}{1682} = 1.044 \quad (1)$$

- b) Scaling in the transverse plane (x-y plane) to match the target mass.

$$\lambda_{x, \text{scaled}} = \lambda_{y, \text{scaled}} = \sqrt{\frac{m_{\text{target}}}{m_{\text{HIII dummy}} \lambda_{z, \text{scaled}}}} = 0.978 \quad (2)$$

Where  $m_{\text{target}} = m_{\text{HIII dummy}}$ , since there is no deviation in the body mass of HIII dummy.

## B) Scaling of Inertial Properties

The components of Hybrid III were modeled as both rigid and deformable. As the mass densities of the deformable parts remain constant between the actual and scaled dummy, inertial properties (such as mass and inertial tensor components) were calculated from their meshes. In contrast, rigid bodies with simplified mesh have inertial properties usually defined based on the measurement data in the input file. Thus, an algorithm for calculating the mass and inertial tensor components corresponding to the new center of gravity of the scaled model was applied [126]. Scaling factors estimated in the geometric scaling were used for scaling the inertial properties of rigid parts.

Consider a rigid body with a mass  $m$  and the components of the mass moment of inertia tensor  $I$  with respect to a local coordinate system  $o_{xyz}$  parallel to the global axes and  $o(x, y, z)$  - the center of gravity as its origin as shown in Figure 3-6.

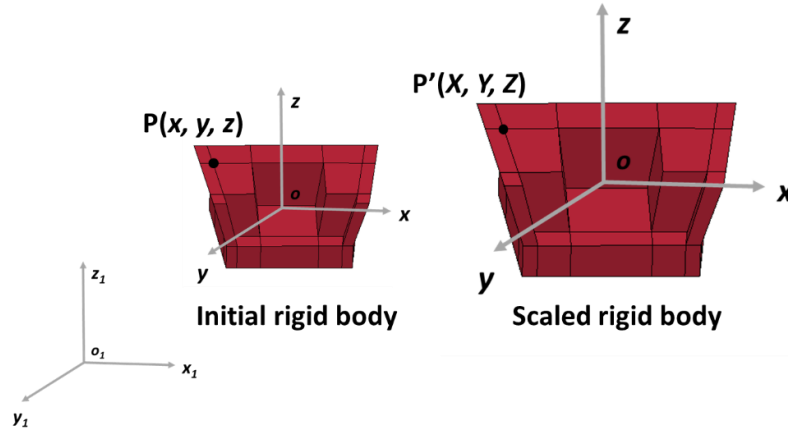


**Figure 3-6 Scaling of a rigid body with local coordinate parallel to the global coordinate**

$$I = \begin{bmatrix} I_{XX} & I_{XY} & I_{XZ} \\ I_{YX} & I_{YY} & I_{YZ} \\ I_{ZX} & I_{ZY} & I_{ZZ} \end{bmatrix} \quad (3)$$

Let us assume a linear transformation (scaling) with respect to the global coordinate system  $O_1 x_1 y_1 z_1$  with the respective scaling factor  $\lambda_x \lambda_y \lambda_z$  and constant mass densities between the models. Mass of the scaled model will be

$$M = m \lambda_x \lambda_y \lambda_z \quad (4)$$

Linear scaling with respect to the global system  $O_1 x_1 y_1 z_1$  will move each P point of the original body which has a coordinate  $(x, y, z)$  with respect to the system  $oxyz$  and coordinate  $(x_1 y_1 z_1)$  with respect to the system  $O_1 x_1 y_1 z_1$  into the point P' of the scaled body which has coordinate  $(X, Y, Z)$  with respect to the system  $OXYZ$  and coordinate  $(X_1 Y_1 Z_1)$  with respect to the system  $O_1 x_1 y_1 z_1$

$$X_1 = \lambda_x x_1 = \lambda_x x + \lambda_x x_{o1} = X + X_{O1}$$

Thus  $X = \lambda_x x$ . Similarly  $Y = \lambda_y y$ ,  $Z = \lambda_z z$

The scaled diagonal component of the inertia tensor will be



$$I_{XX} = \int_{\Omega} (Y^2 + Z^2) \rho dV = \int_{\Omega} (\lambda_y^2 y^2 + \lambda_z^2 z^2) \rho \lambda_x \lambda_y \lambda_z$$

$$dv = \lambda_x \lambda_y \lambda_z (\lambda_y^2 J_y + \lambda_z^2 J_z)$$

Thus, the component of the inertial tensor with respect to the new local coordinate system  $O(\lambda_x \cdot x_0, \lambda_y \cdot y_0, \lambda_z \cdot z_0)$  will be

$$I_{XX} = \lambda_x \lambda_y \lambda_z (\lambda_y^2 J_y + \lambda_z^2 J_z)$$

$$I_{YY} = \lambda_x \lambda_y \lambda_z (\lambda_x^2 J_x + \lambda_z^2 J_z) \quad (5)$$

$$I_{ZZ} = \lambda_x \lambda_y \lambda_z (\lambda_x^2 J_x + \lambda_y^2 J_y)$$

where

$$J_x = (I_{ZZ} + I_{yy} - I_{xx}) / 2$$

$$J_y = (I_{ZZ} + I_{xx} - I_{yy}) / 2 \quad (6)$$

$$J_z = (I_{yy} + I_{xx} - I_{zz}) / 2$$

The scaled off-diagonal components of the inertia tensor will be

$$I_{XY} = \int_{\Omega} YZ \rho dV = \int_{\Omega} \lambda_x \lambda_y \cdot xy \rho \lambda_x \lambda_y \lambda_z dv = \lambda_x^2 \lambda_y^2 \lambda_z^2 I_{xy}$$

Similarly,

$$I_{XY} = \lambda_x^2 \lambda_y^2 \lambda_z^2 I_{xy}$$

$$I_{YZ} = \lambda_x^2 \lambda_y^2 \lambda_z^2 I_{xz} \quad (7)$$

$$I_{YZ} = \lambda_x^2 \lambda_y^2 \lambda_z^2 I_{xz}$$

When the axes of the local coordinate system are not parallel to corresponding axes of the global system, as shown in Figure 3-7, the components of mass inertia tensor in the new local coordinate rigid body  $OXYZ$  can be determined by the following steps

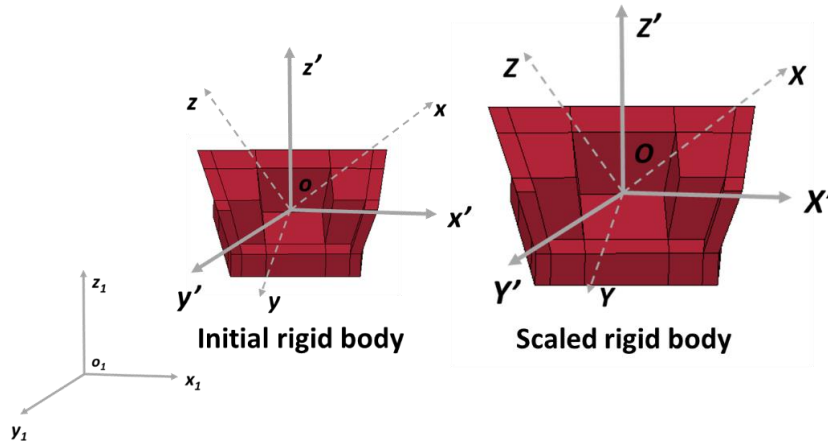


**Figure 3-7 Scaling of a rigid body with local coordinate non-parallel to the global coordinate**

- a) Obtain the inertial tensor  $i'$  with respect to a system  $ox'y'z'$  with the axes parallel to the global coordinate system  $O_I x_I y_I z_I$  from the initial coordinate system  $oxyz$ . The inertia tensor  $i'$  will be

$$i' = Q \cdot i \cdot Q^T \quad (8)$$

where  $Q$  is the transformation matrix (orthogonal matrix) between  $oxyz$  and  $ox'y'z'$ .

- b) Obtain the inertia tensor  $I'$  of the scaled rigid body with respect to a system  $OX'Y'Z'$  with the axes parallel to the global system using Equations 5 and 7.
- c) Obtain the inertia tensor  $I'$  with respect to a system  $OXYZ$  with axes parallel to the initial local coordinate system  $oxyz$ . Thus, the inertia tensor  $I$  will be

$$I = Q^T \cdot I' \cdot Q \quad (9)$$

### **C) Scaling of joint properties**

Joints connected all the components of the dummy with the moment-angle curve defining the stiffness characteristics. Based on the principles of dimensional analysis, the moment of the scaled body can be expressed as the function of the length-scale factors [133-135].

$$M_{scaled} = \lambda_x \lambda_y \lambda_z M_{Hybrid III} \quad (10)$$

Thus, all the moment-angle curves of the scaled dummy were scaled by the above Equation 10.

### 3.3.4 Validation of Scaled Hybrid III pedestrian Dummy

#### Head drop test

Hybrid III dummy head was validated to the standard head drop certification test recommended in the Code of Federal Regulation under the title 49, Part 572 subpart E [136]. A FE simulation based on the test set-up was conducted using LS-DYNA. (Figure 3-8 ) The HIII – head assembly was allowed to drop freely and impact a rigid plate surface from initial velocities corresponding to a drop height of 376 mm. Head acceleration was measured at the head Center of Gravity (C.G) from the tri-axial accelerometer block and filtered at SAE filter class 1000.

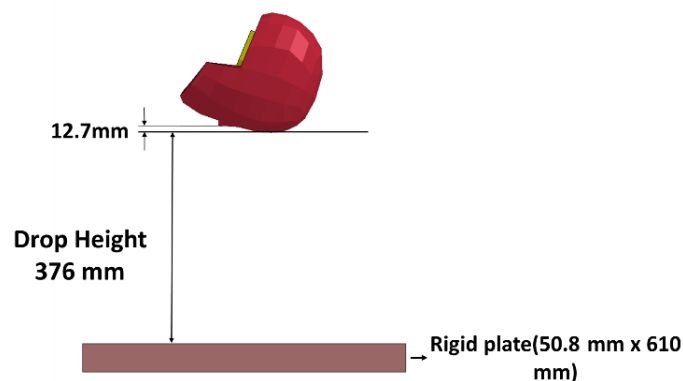


**Figure 3-8 Head drop test set up**

## Validation at Full-body level

The whole-body kinematics of the scaled HIII dummy model during a Car-to-Pedestrian Collision (CPC) with a mid-sized sedan vehicle was validated against the vehicle to cadaver test data[137] from seven different statured PMHS ((Postmortem Human Subject) as described in Table 3-3. Identical test conditions as in the PMHS test were reconstructed in FE simulation to assess the biofidelity of the Hybrid III dummy in CPCs.

**Table 3-3 Age, mass and pre-test stature of PMHS test specimen**

Specimen ID	Age/ Gender	Mass (kg)	Pre-test Stature (mm)
S1	67/F	63.5	1631
S2	57/F	88.8	1640
S3	71/F	82.5	1645
M4	32/F	90.6	1729
M5	49/F	92.9	1743
T6	70/M	87.0	1790
T7	74/M	91.6	1843

*S – Short, M –Medium, T- Tall, F – Female, M – Male*

**Development of test vehicle:** Toyota Camry (The model year 2010) mid-sedan FE model in LS-DYNA code (Ver. SMP s R9.2.0, LSTC), developed by CCSA, was used [96]. All the frontal structure and BIW (Body-In-White) parts up to the b-pillar were extracted. In order to match the geometry of the mid-sedan test vehicle used in the cadaver study[137], extracted vehicle front structures were scaled and morphed to corresponding geometric dimensions using Hypermesh (Altair, Troy, MI USA) (Figure 3-9). Table 3-4 describes the percentage difference of different geometric dimensions between the modified Camry

FE model and test vehicle used in the test. Extra nodal masses were created to obtain the actual vehicle mass.

**Table 3-4 Percentage difference in geometric measurement between the FE test vehicle and PMHS test vehicle**

Measurements	Mid sedan Test Vehicle (mm)	Modified Camry FE (mm)	% Difference
B	228	221.83	2.706
C	420	419.40	0.143
E	752	753.65	-0.219
F	107	111.211	-3.936
G	979	981.89	-0.295
J	123	119.228	3.067
K	7	7.086	-1.229
L	1061	1057.55	0.325
M	58	58.16	-0.276

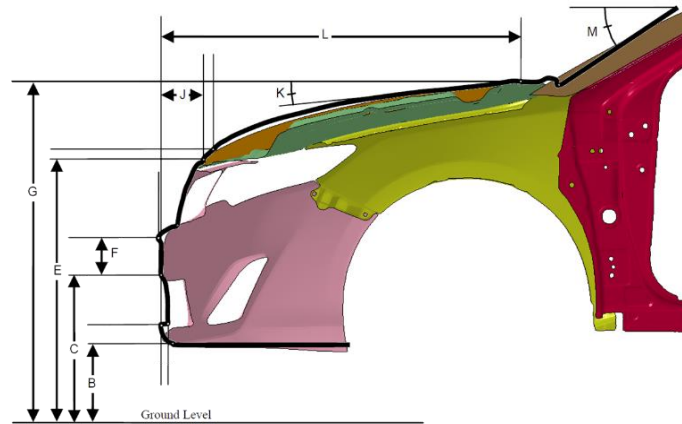


**Figure 3-9 Modified FE vehicle with reference to the test vehicle centerline contour dimension**

**Simulation setup:** As shown in Figure 3-10, the configuration setup was based on the pedestrian testing protocol of Euro-NCAP was adopted [85]. The Hybrid III dummy was laterally positioned at the center of the vehicle line in a mid-stance walking posture, with the rearward leg being impacted first by the vehicle. As defined in the cadaver test, two dummy arms were bound anteriorly at the wrists, with the left wrist closest to the abdomen. In the actual testing, PMHS was supported by a harness and released approximately 20-30ms before the collision. Markers were attached to the PMHS head, thoracic vertebra (T1), and pelvis to record the kinematics relative to the car. Before the impact at 5ms, the gravity acceleration was assigned to the simulation in the FE simulation. A force corresponding to the body mass of the dummy was applied upward to initiate the foot-ground contact. The appropriate contact was defined between the vehicle and dummy model (surface-to-surface) and between individual parts (single surface). Based on the average data reported in the literature[138], the contact coefficient of friction between the dummy and vehicle was 0.3 and 0.7 between the shoes and ground. History nodes corresponding to the location of markers were defined in the dummy model to quantitatively compare the pedestrian kinematics predicted by the dummy model to the corresponding test data.

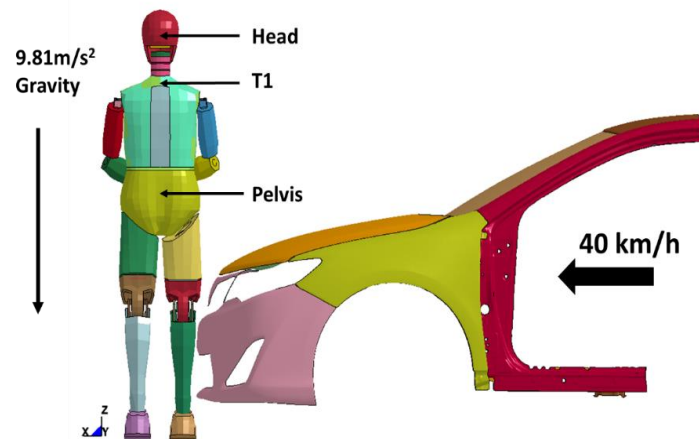


**Figure 3-10 Car to Pedestrian Collision – NCAP protocol used in PMHS test. The test vehicle was accelerated at 40 km/h to laterally hit the pedestrian at the vehicle centerline. A gravitational acceleration load of  $9.81\text{m/s}^2$  was applied to all nodes. Nodal displacement trajectories of the head, T1 and pelvis were recorded.**

## Vehicle FE model

The Toyota Camry passenger sedan (the model year 2012) FE model (Figure 3-11) developed by the Centre for Collision Safety and Analysis (CCSA) under contract with the Federal Highway Administration (FHWA) was chosen for this study [96]. This model has been developed through a reverse engineering approach and validated against the National Highway Safety Administration (NHTSA) frontal New Car Assessment Program (NCAP) test for the corresponding vehicle [99].

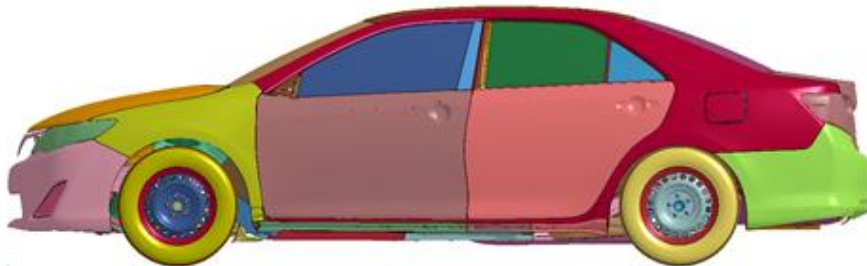


**Figure 3-11 Toyota Camry mid-size passenger sedan (Model year 2012)**

### 3.3.5 Development of simplified FE vehicle model

However, while the FE vehicle model was expected to aid current and future research on occupant risk and vehicle compatibility, a full-scale vehicle model in a pedestrian crash would incur higher computational costs. As a result, this model has to be modified to perform CPC simulations [80, 98]. All frontal structures up to the B pillar were extracted from the original model using Hypermesh (Altair, Troy, MI USA). Both doors were also removed. All the engine components below the hood remained in situ. All vehicle contact, material definitions were unchanged. Nodal mass elements from the original car model were not deleted, and mass values have remained unchanged. Trimmed edge of the FE nodes and nodal mass elements are constrained to the nodal mass element at the C.G location as in the original model. Extra masses were added to the C.G nodal mass to obtain the same mass as the original car model. Accelerometer definitions in the front

structure of the vehicle were not deleted. The modified trimmed vehicle model is shown in Figure 3-12.

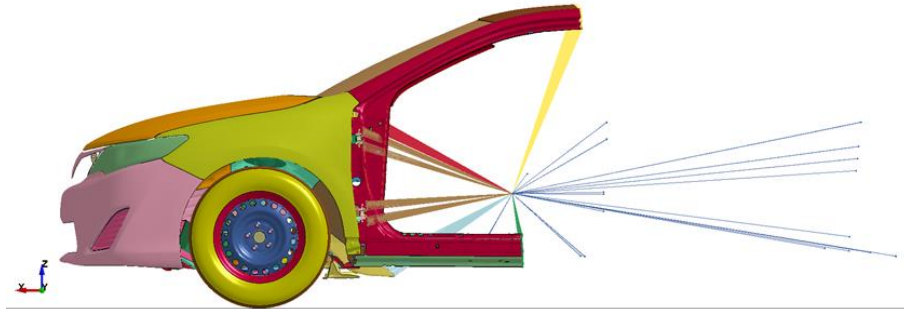


**Figure 3-12 Simplified vehicle FE model**

### 3.3.6 Validation of simplified FE vehicle model

NCAP (New Car Assessment Programme) full-frontal wall impact was simulated, and the results were compared to the baseline and actual crash test data from the NHTSA to validate the simplified model. Figure 3-13 shows the overall global deformation pattern, which was relatively similar to the actual crash test. In addition, the acceleration response from the engine top and bottom was compared against the test data and baseline simulation, as noted in Figures 3-14. Again, a reasonable agreement was found for the simplified car model.

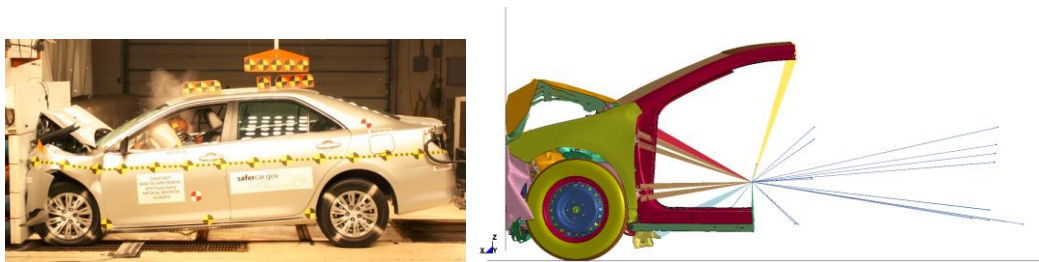


**Figure 3-13 Global deformation pattern of the simplified FE model during the full-frontal crash test**



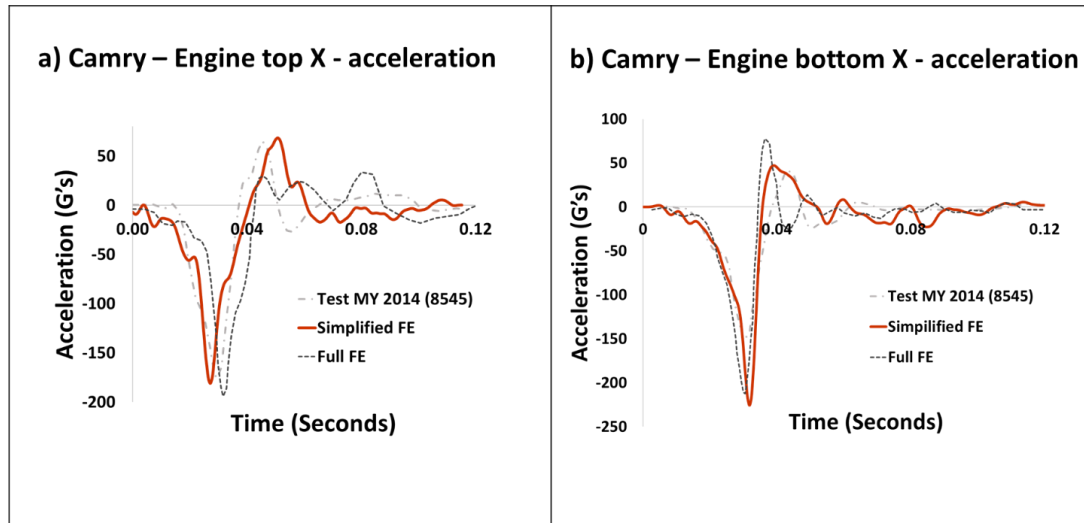


**Figure 3-14 a) Camry CPC head resultant acceleration b) Camry CPC head resultant velocity**

### 3.3.7 Validation of pedestrian head kinematics in CPC

The simplified vehicle model was validated by performing a Car to Pedestrian Collision (CPC), and the kinematic head responses were compared. Scaled Hybrid III 50th percentile male standing dummy was used. Initially, the dummy model (without posture/gait) was positioned laterally at the vehicle centerline. Simulation configuration set up defined in the pedestrian testing protocol of Euro NCAP [100] was employed as illustrated in Figure 3-15. Head acceleration and rotational velocity responses were measured from the C.G of the dummy head, as shown in the graph. There was good agreement between head responses between the Full FE and simplified vehicle model during the CPC. (Figures 3-16 and 3-17)

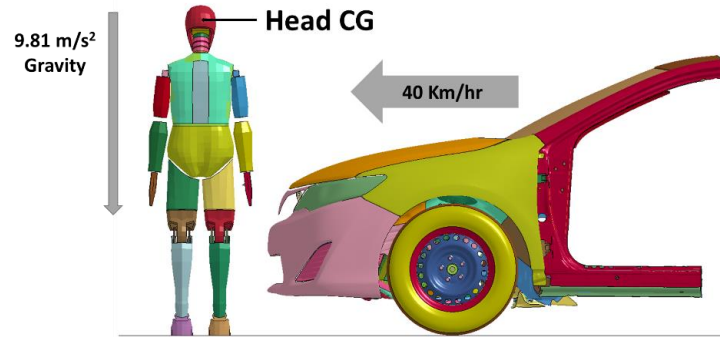


**Figure 3-15 Car-to-Pedestrian Collisions (CPCs) - Simplified mid-sedan car model was accelerated at 40 km/h and impacted the pedestrian FE model at the vehicle centerline (y-axis). A gravitational load of 9.81m/s<sup>2</sup> was applied to all nodes and a 6DOF accelerometer was defined at the CG of the pedestrian head.**

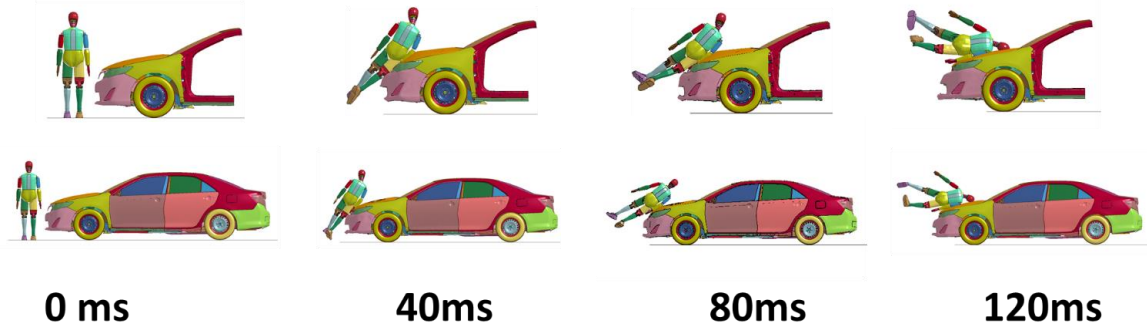


**Figure 3-16 Pedestrian kinematics of scaled HIII 50<sup>th</sup> percentile average male in CPC (Sedan, 40 km/h)**

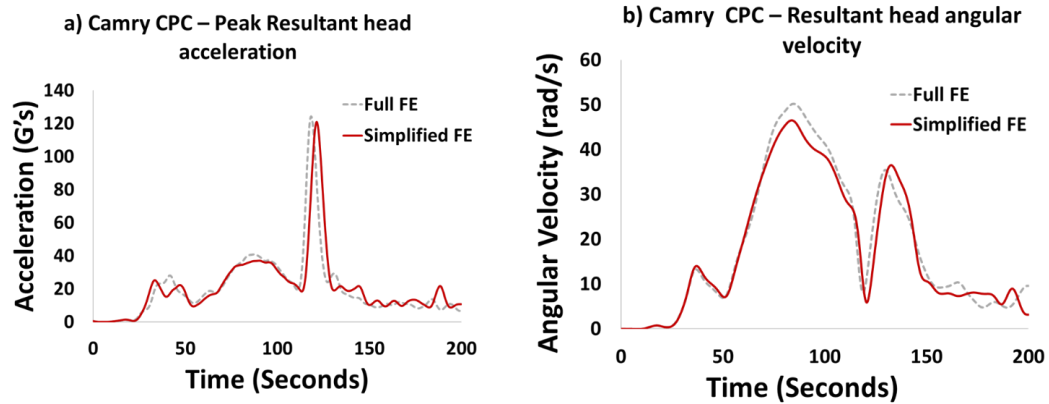


**Figure 3-17 a) Camry CPC – Peak Resultant head acceleration b) Camry CPC – Peak Resultant head angular velocity**

### 3.4 Accident Reconstruction

The accident reconstruction workflow involves four steps pipeline. (Figure 3-18)

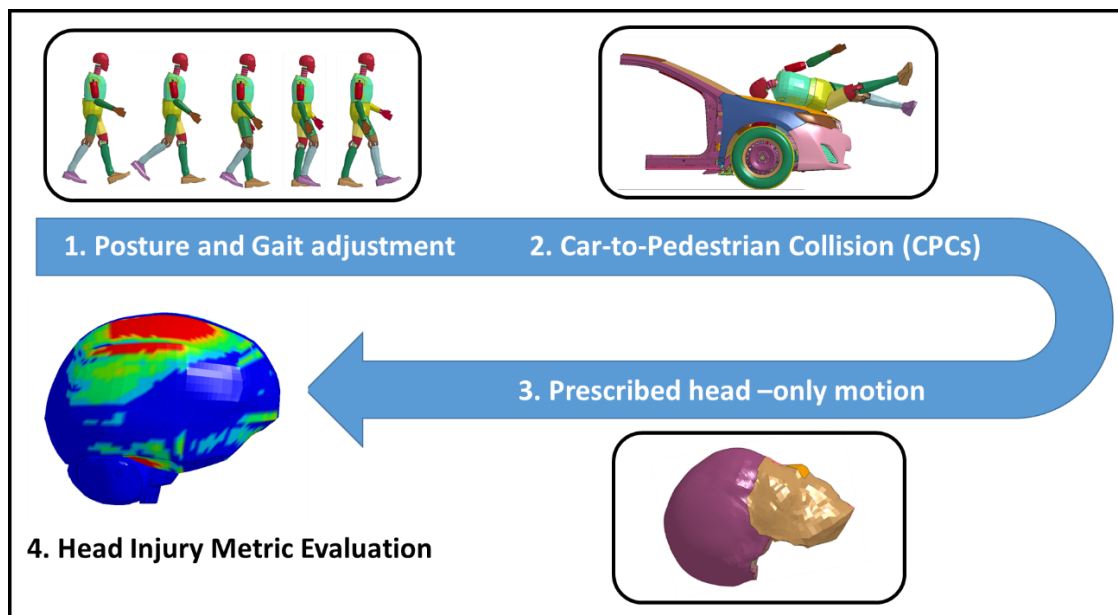


**Figure 3-18 Accident reconstruction – Four-step pipeline**

- 1. Posture and Gait Adjustment:** Three different pre-impact pedestrian gait serials such as walking (Figure 3-19), running (Figure 3-20), and emergency gaits

(Figure 3-21) based on the literature were considered in this study [13, 120, 121]. Position Tree file algorithm was defined for the scaled HIII dummy. A Dummy positioning tool in LS-pre post (Version 4.8) was used to adjust the body parts of the dummy to respective gait serial based on the orientation angle of all joints from a previous study [13]. We automated the entire 30 different gaits serial adjustment using the C-File command in the LS-Pre post.

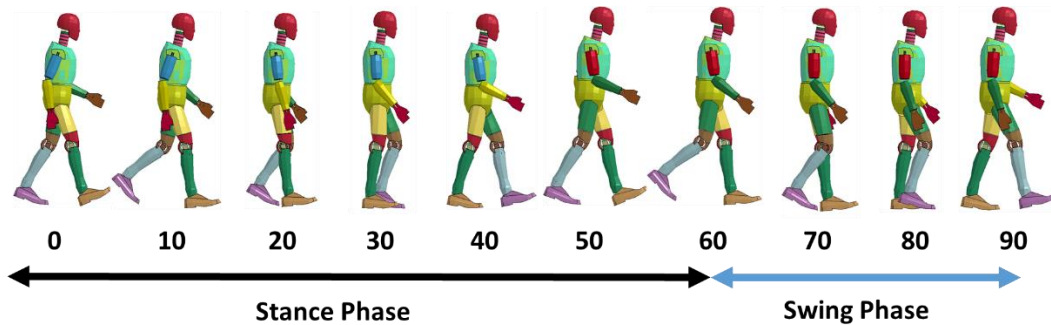


**Figure 3-19 Walking gaits**

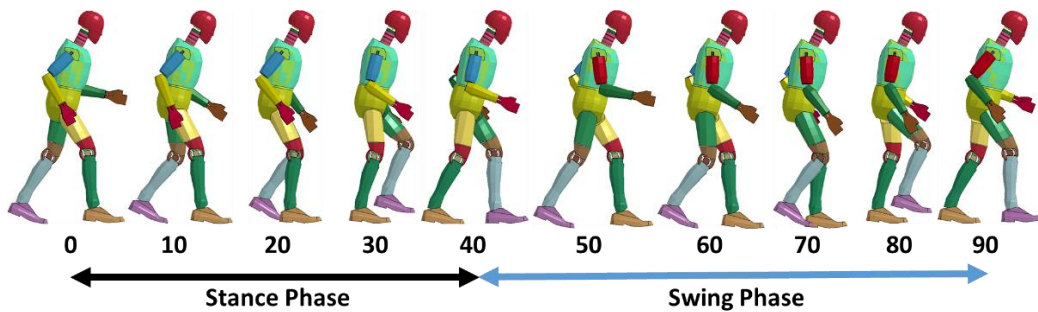


**Figure 3-20 Running gaits**

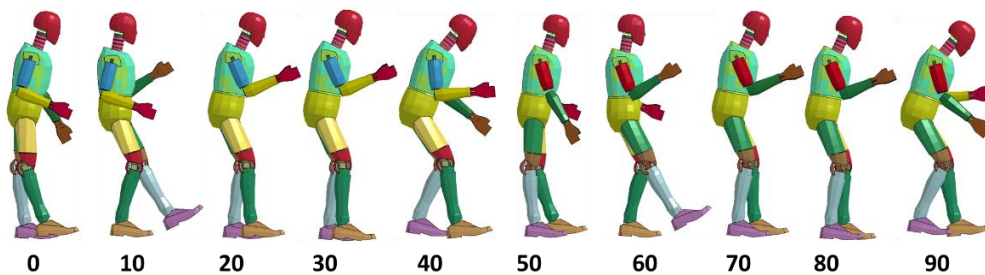


**Figure 3-21 Emergency gaits**

**Car-to-Pedestrian Collisions (CPC):** The configuration set up based on the pedestrian testing protocol of EuroNCAP was adopted [100]. The Hybrid III dummy was positioned laterally at the centerline of the vehicle. The simplified mid-sedan vehicle model was accelerated at collision speeds of 20, 30, 40, km/h and impacted the scaled HIII pedestrian dummy at the vehicle centerline. The head CG and H-point of the dummy were positioned in line with the vehicle centerline. An appropriate contact definition was defined between the vehicle model and the dummy model. The coefficient of contact friction between the pedestrian model and the vehicle was 0.3, the coefficient of contact friction between the shoes and the ground was 0.7 [80]. Accelerometers were defined at the CG of the dummy head to measure the linear and kinematic in head local coordinate system. All the linear and rotational acceleration curves were filtered by CFC 180 [85]. A total of 90 CPC's were simulated using 30 different gait serials.

**Prescribed head-only motion:** Head-to-car impact was reconstructed with an isolated THUMS 50th percentile average male (Figure 3-22) head validated [139-141] head model in LS-DYNA code by performing a prescribed head-only motion (Ver. SMP s R9.2.0, LSTC). Six Degree of Freedom (DOF) head kinematics (three linear and three rotational acceleration) from CPC simulation were prescribed to the isolated head model to obtain the head dynamic and intracranial response for all simulated cases.

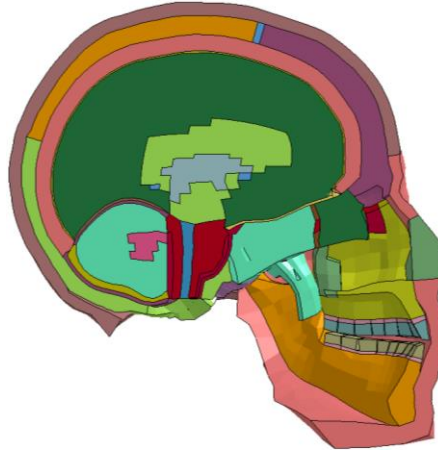


**Figure 3-22 Isolated THUMS FE head – Prescribed head only prescribed motion**

- 2. Head injury Metric Evaluation:** Six head injury criteria were calculated for all reconstructed 90 cases using MATLAB. Kinematic-based head injury metrics such as HIC15 (Head Injury Criterion), BrIC(Brain Injury Criteria), and DAMAGE ( Diffuse Axonal Multi-Axis General Evaluation ) were calculated from the head local coordinate system of the dummy and tissue-level strain-based metrics such as MPSmax (Maximum Principal Strain ), MPSmean (Average Maximum Principal strain ) was calculated from the intracranial response from THUMS isolated head model.

**Table 3-5 Head injury criteria considered in the study**

Head injury Criteria	
<b>Kinematic-based metrics</b>	Head Injury Criterion (HIC15)
	Brain Injury Criterion (BrIC)
	DAMAGE (Diffuse Axonal Multi-Axis General Evaluation)
<b>Intracranial strain-based metrics</b>	Maximum Principal Strain (MPSmax)
	Average strain (MPSmean)

	Cumulative Strain Damage Measure (CSDM15)
--	---

## 3.5 Results

### 3.5.1 Validation results of head drop test and whole-body kinematics

#### Head drop test

Peak resultant head acceleration should be in the range of 225 and 275g as per the test requirement. Figure 3-23 shows the unimodal head acceleration-time response with four different physical dummy head drop tests. Material parameters of the head skin (\*MAT\_VISCOELASTIC (MAT\_006)) were optimized to improve the simulation and certification test correlation.

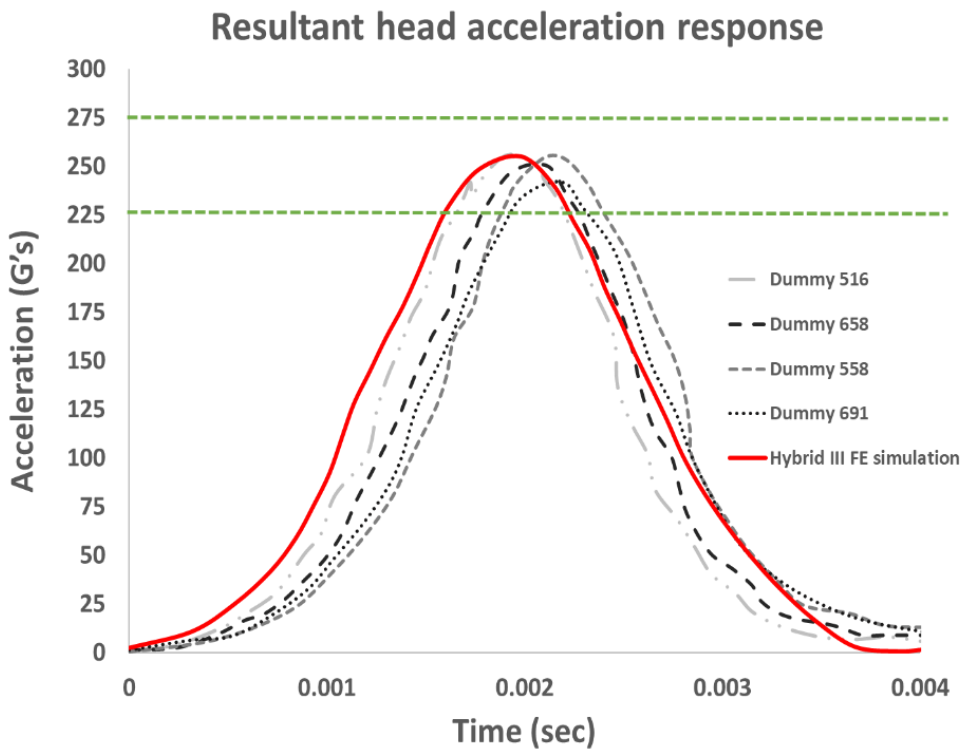


**Figure 3-23 Resultant head acceleration comparison**

## Validation at Full-body level

**Comparison of kinematic trajectories:** All upper body kinematic trajectories in the PMHS study were determined using a detailed photo target tracking analysis of high-speed video images from all tests. The HIII dummy trajectories were calculated using the filtered (CFC 180) FE nodal displacement of respective history nodes. To provide a basis for comparison, all dummy trajectories were converted to the PMHS vehicle coordinate system. Figure 3-24 shows the dummy head, vertebra T1, and pelvis trajectories in CPC plotted in the vehicle (YZ) coordinate system with the test vehicle as a reference.

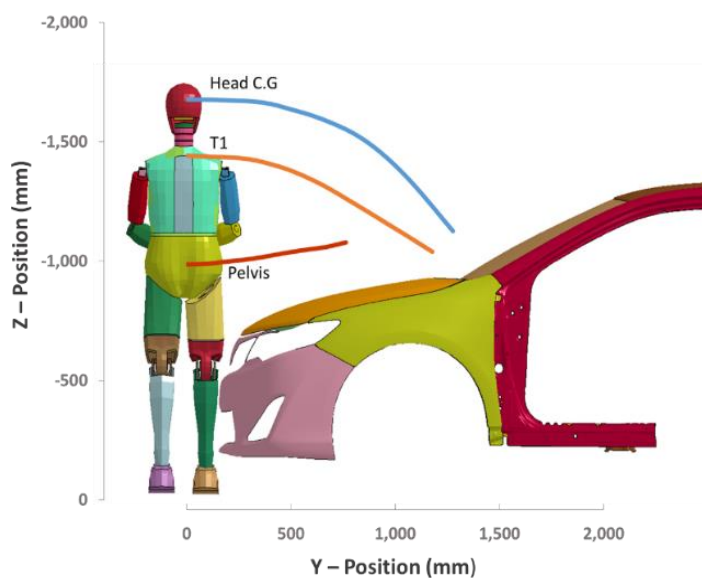
Comparing the HIII dummy's trajectories against PMHS subjects (Figure 3-25) revealed that, due to their similar stature, the dummy exhibited kinematics identical to those of medium-statured PMHS subjects M4 and M5. It was found that the dummy and PMHS trajectories were not similar in length because the PMHS slides further up the hood than the dummy before the head impact. The difference in the slide between PMHS and dummy was due to the lack of pelvis and lower extremities biofidelity. Unlike PMHS, the pelvis trajectory of the dummy was merely a straight line indicating no pinning or sliding with the hood contact. This can be visualized by comparing the dummy FE simulation to high-speed video images captured from three (S1, M5, T7) PMHS subjects in a 40ms time interval, as illustrated in Figure 3-27.

At 40ms, the leading edge of the hood made contact with the dummy's upper leg, and the feet lost contact with the ground. Since most of the dummy parts were modeled as rigid, the lower extremities of the dummy did not wrap around the vehicle as PMHS subjects. At 80ms, as the upper body began to rotate and arms come in contact with the hood, dragging the feet above the ground. This clearly showed the lack of biofidelity between the upper leg and pelvis. At 120 ms, the shoulder contacted the hood, and upper body rotation continues until the head collided with the windshield. However, there is a slight difference in the overall kinematics of HIII, the upper body rotational kinematics, head contact time, and area of contact matched well with the PMHS subject M5 of similar stature.

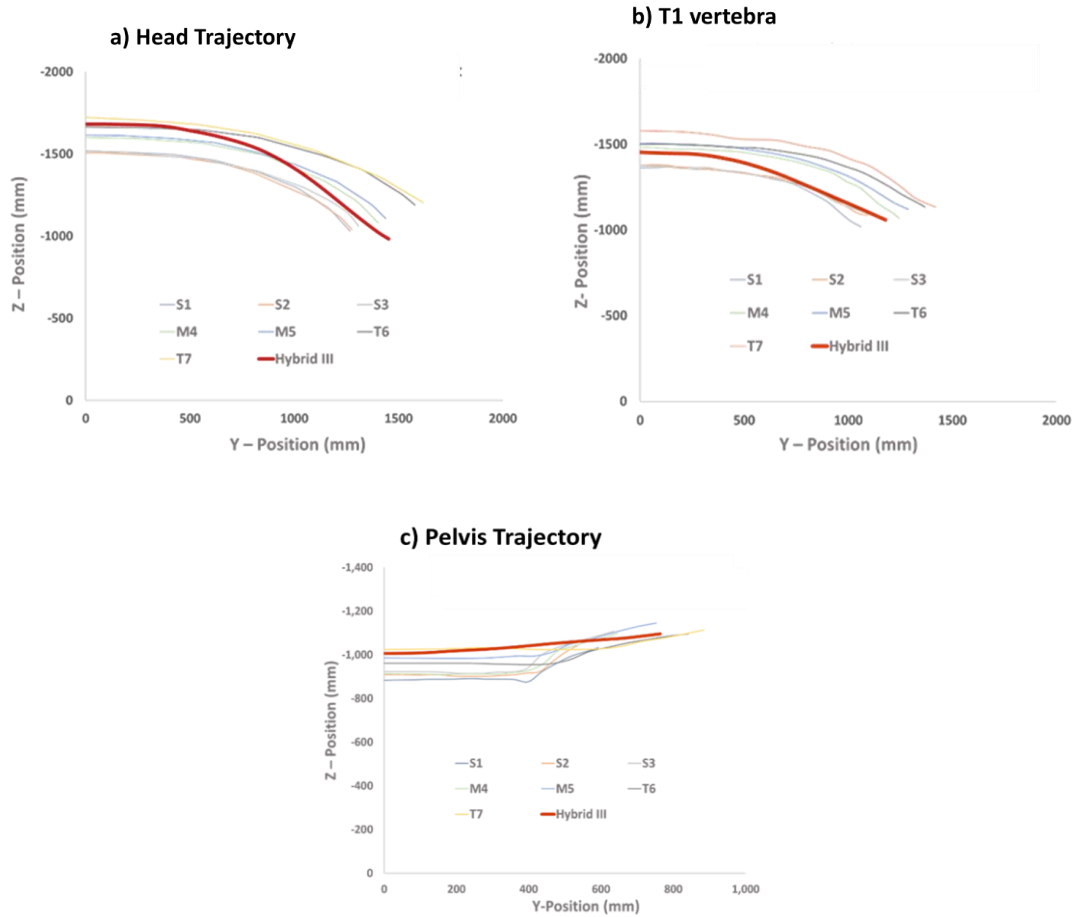


**Corridor development:** Based on previous research [142, 143], the dummy's overall kinematics were validated against the cadaver data by developing kinematic response corridors from average scaled trajectories and path length calculated from all PMHS subjects. Boxed – corridors were created by drawing a square around each data point in the average curve, aligning the edges with the coordinate axes, and setting the square length to  $2k$ . With  $k=10$ , upper and lower bound corridors with 10 percent of path length were developed.

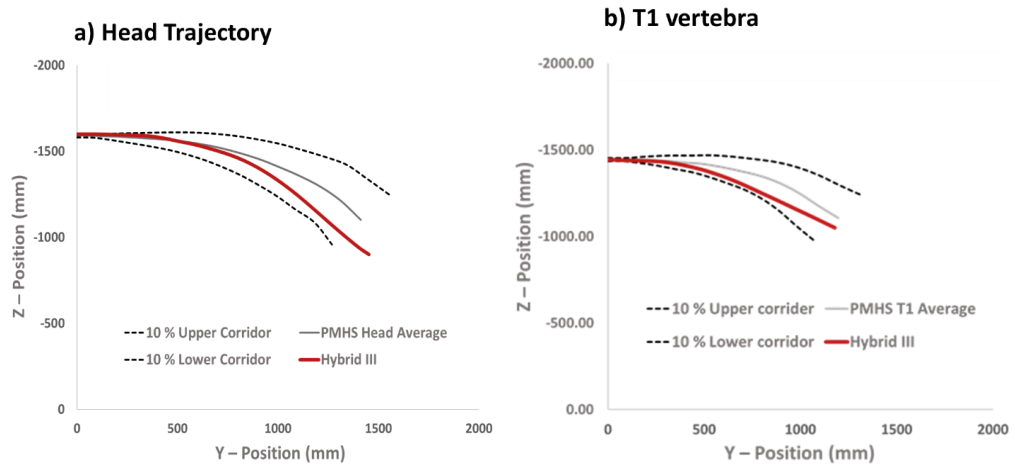
Average Head, T1, and pelvis trajectories from the PMHS were plotted against the dummy with 10% upper and lower corridors. (Figure 3-26). All the kinematic trajectories of the HIII lies within the 10 % path length corridors. Despite the lack of pelvis biofidelity, the pelvis trajectory was adjacent to the upper bound corridor but mostly within the 10 % corridor. More testing data were required to modify the joint definitions between the pelvis and upper legs to improve the biofidelity of lower extremities. Overall, the Hybrid III dummy mostly replicated the overall pedestrian kinematics of PMHS.

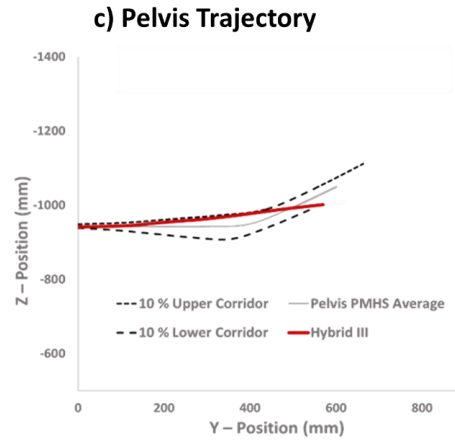


**Figure 3-24 Dummy head, vertebra T1, and pelvis trajectories in CPC plotted in the test vehicle (YZ) coordinate system**

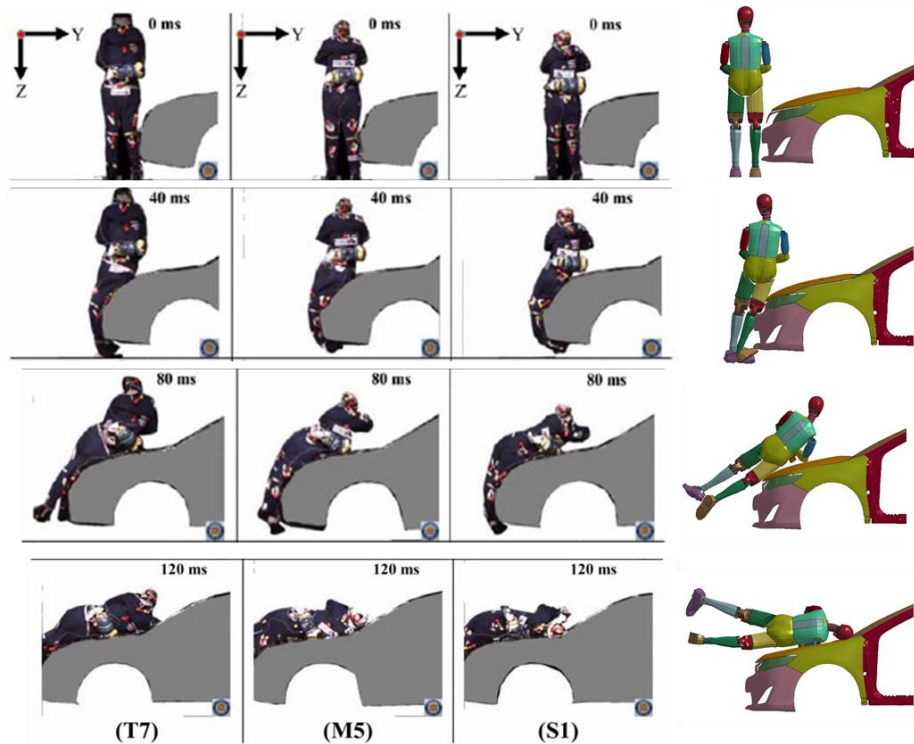


**Figure 3-25 HIII Trajectories compared to PMHS 10% corridor a) Head Trajectory b) T1 Vertebra c) Pelvis Trajectory**





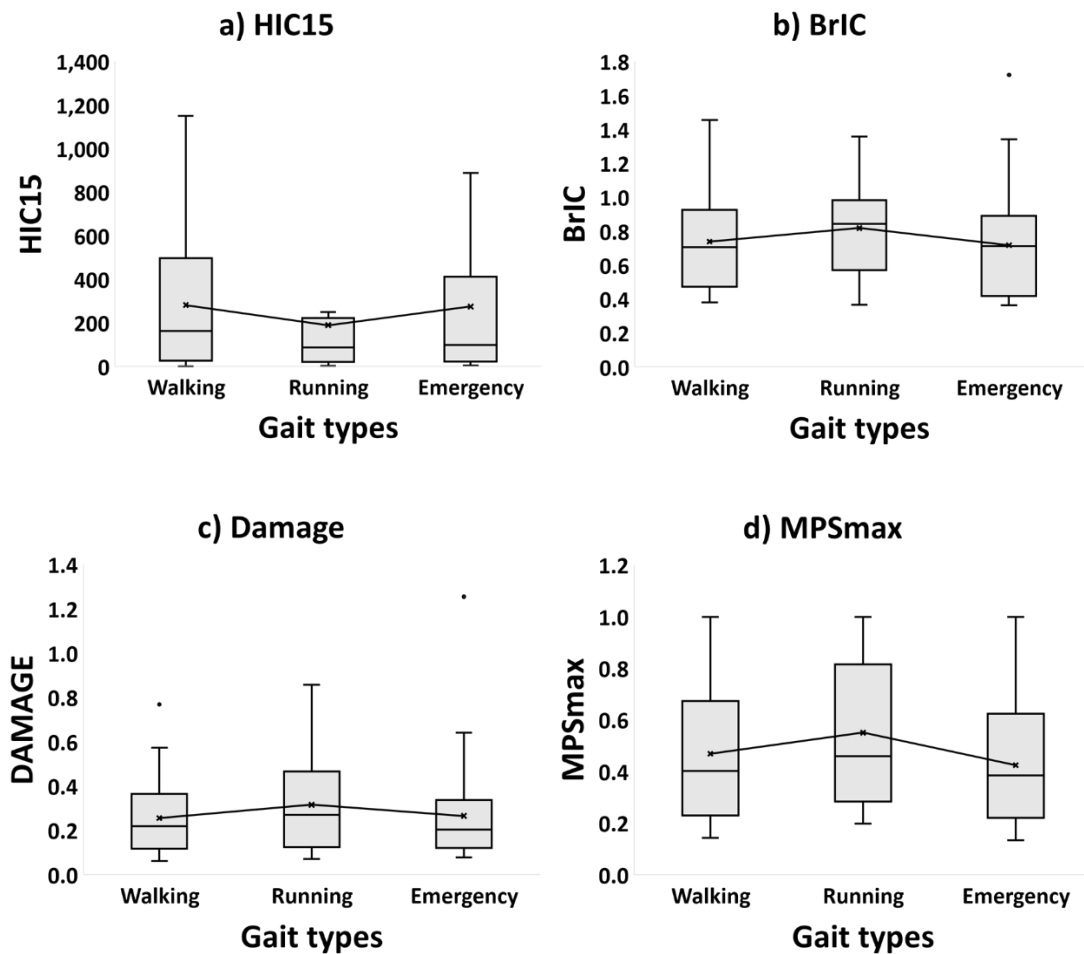
**Figure 3-26 Kinematic trajectories of the head, vertebra T1 and pelvis with reference to the test vehicle front structure**



**Figure 3-27 Pedestrian kinematics compared between the high-speed video images from PMHS test with tall, short, and medium statured specimens and HIII pedestrian simulation**

### 3.5.2 Effect of walking, running, emergency gait and posture on the head kinematics and intracranial strain response

Head injury metrics were calculated for all 90 cases. The distribution of all calculated metrics was compared based on the gait types (walking, running, and emergency) using box plots. (Figure 3-28) Walking has the highest average HIC15 score of 281, whereas running has the least score of 189. Running has the highest BrIC, DAMAGE, MPSmax, MPSmean, and CSDM15 than the other two gait types. Emergency and walking are almost equal for BrIC, DAMAGE, MPSmean, but emergency has slightly low MPS max and CSDM15 values.



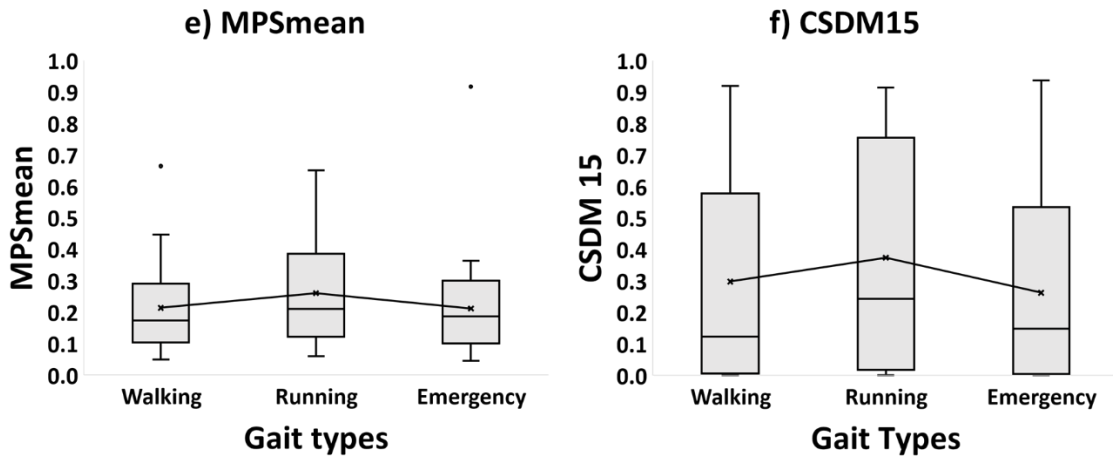


**Figure 3-28 a) HIC15 b) BrIC c) DAMAGE d) MPSmax e) MPSmean f) CSDM15**

### 3.5.3 Correlation between head kinematics and brain strains

The relationship between the head kinematics and intracranial brain strain was studied by conducting linear regression analysis (Figure 3-29) between the head kinematic such as RPLA (Resultant Peak Linear Acceleration), RPRV (Resultant Peak Rotational Velocity), RPRA (Resultant peak rotational Acceleration), and Strain metric such as MPSmean, MPSmean, CSDM15. We also studied the correlation between the kinematic-based metric such as HIC15, BrIC, and DAMAGE. RPRV ( $R^2 = 0.65 \pm 0.05$ ,  $P < 0.01$ ) correlated strongly with brain strains than RPRA ( $R^2 = 0.57 \pm 0.04$ ,  $P < 0.01$ ). RPLA correlated ( $R^2 = 0.53 \pm 0.05$ ,  $P < 0.01$ ) less with the brain strain when compared to other head kinematics. DAMAGE, a similar strain metric calculated from the second-order system, heavily correlated ( $R^2 = 0.76 \pm 0.05$ ,  $P < 0.01$ ). Interestingly, HIC15 has shown a middling correlation ( $R^2 = 0.43 \pm 0.05$ ,  $P < 0.01$ ) with brain strain.

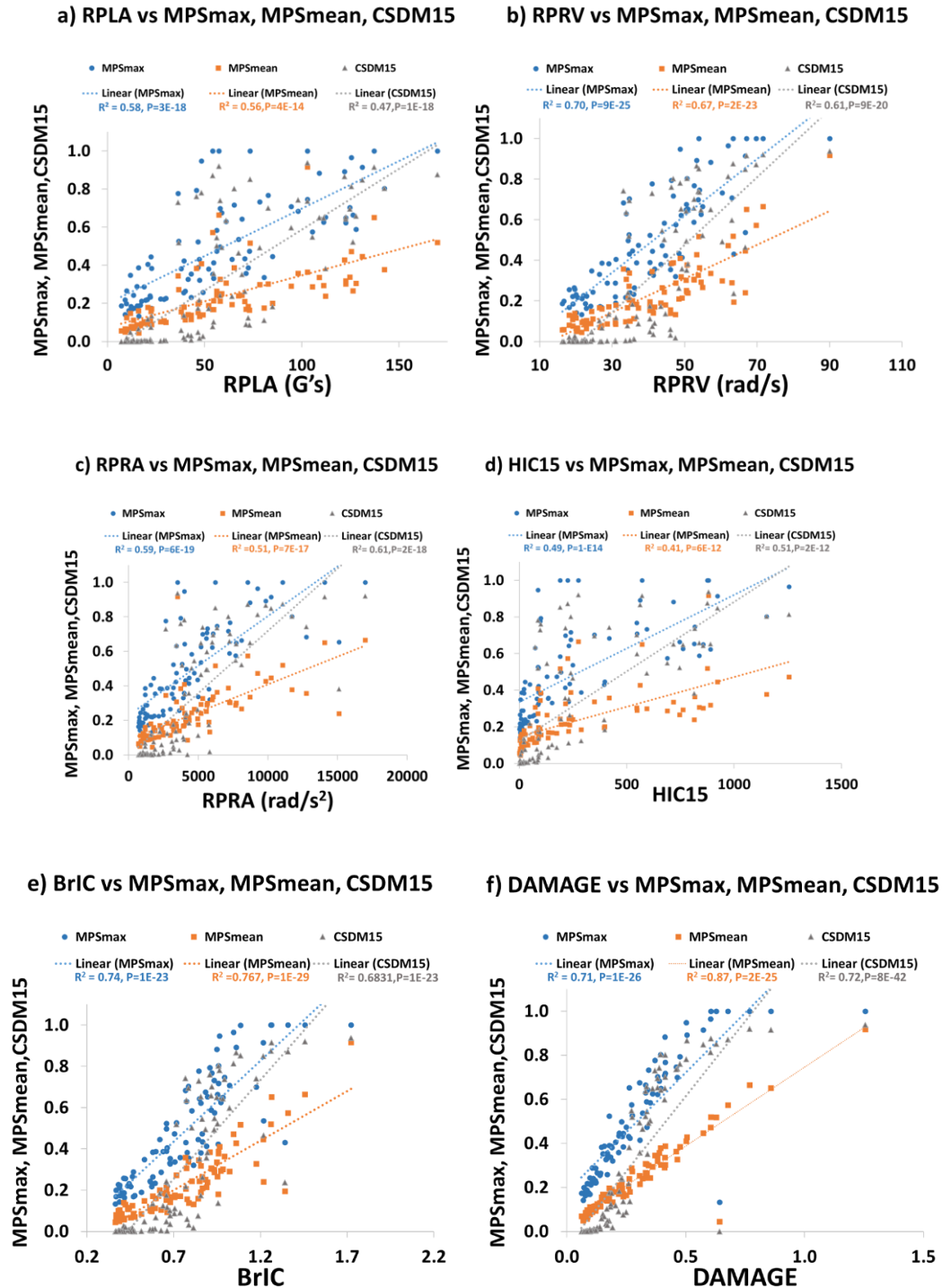
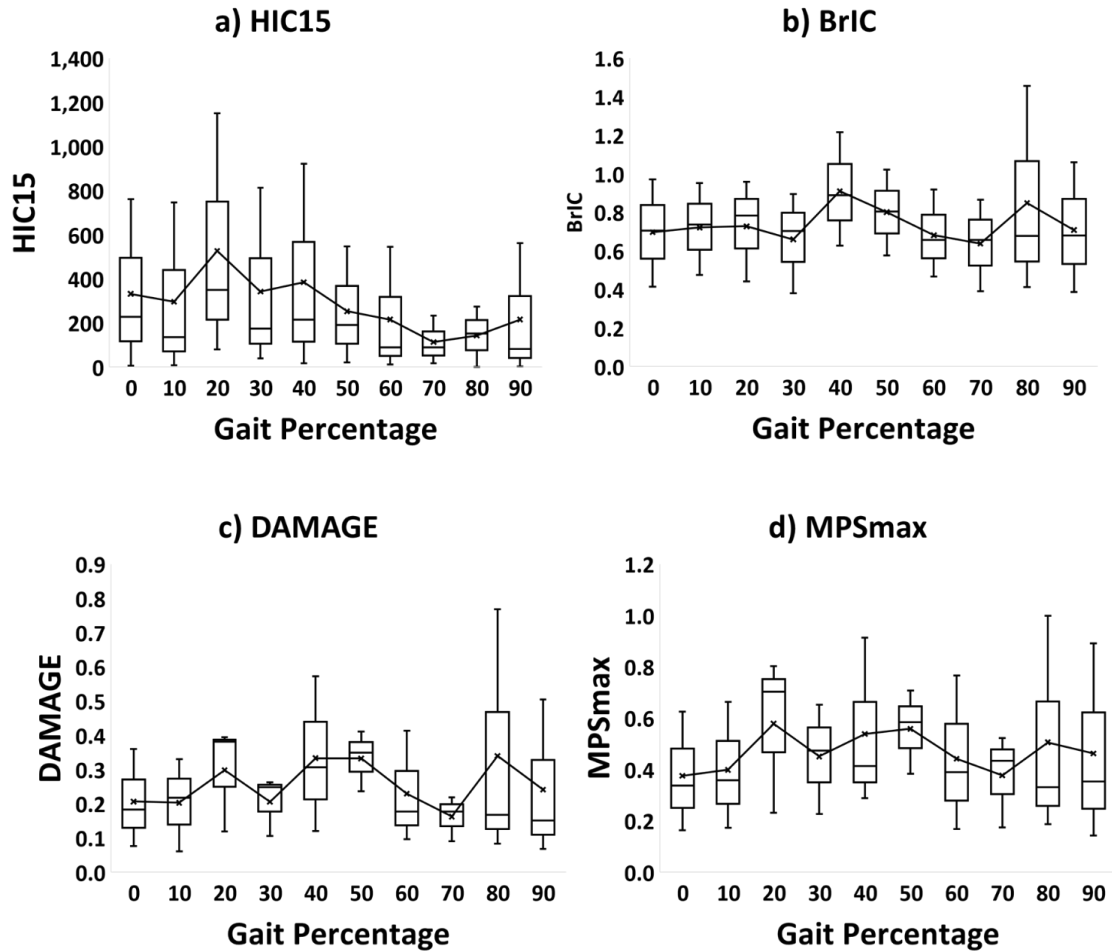


Figure 3-29 a) RPLA vs. MPSmax, MPSmean, and CSDM15 a) RPRV vs. MPSmax, MPSmean, and CSDM15 a) RPRA vs. MPSmax, MPSmean, and CSDM15 a) HIC15 vs. MPSmax, MPSmean, and CSDM15 a) BrIC vs. MPSmax, MPSmean, and CSDM15 a) DAMAGE vs. MPSmax, MPSmean, and CSDM15

### 3.5.4 Effect of gait percentage on the head kinematics and intracranial strain response

Figures 3-30, 3-31, and 3-32 show the distribution of all calculated head injury criteria based on gait percentage for walking, running, and emergency gaits using box plots.



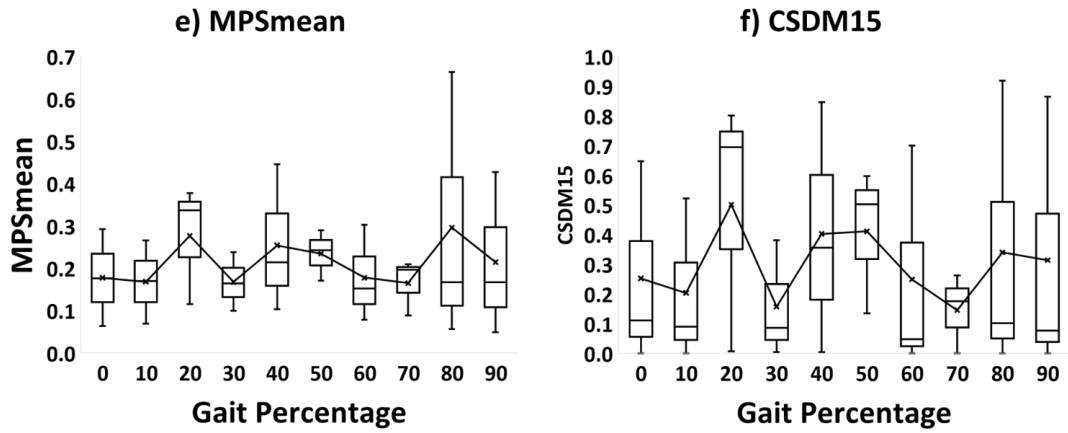
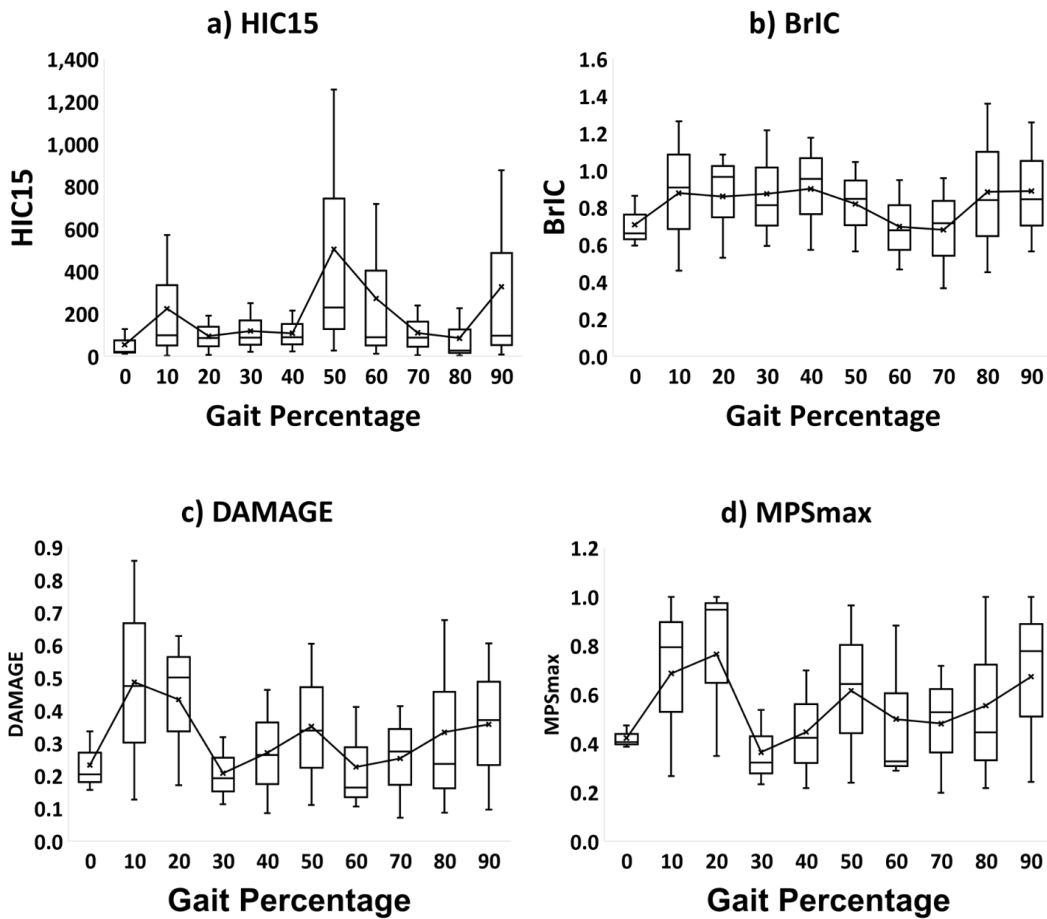
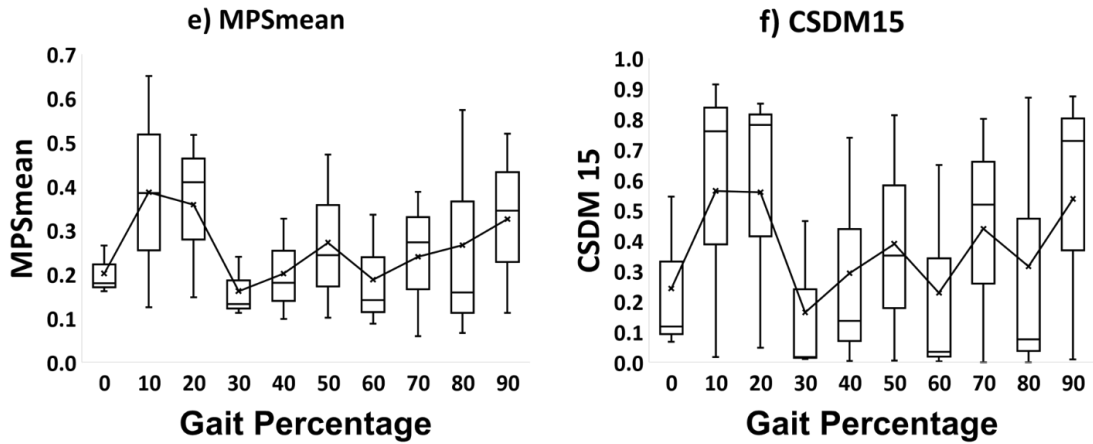


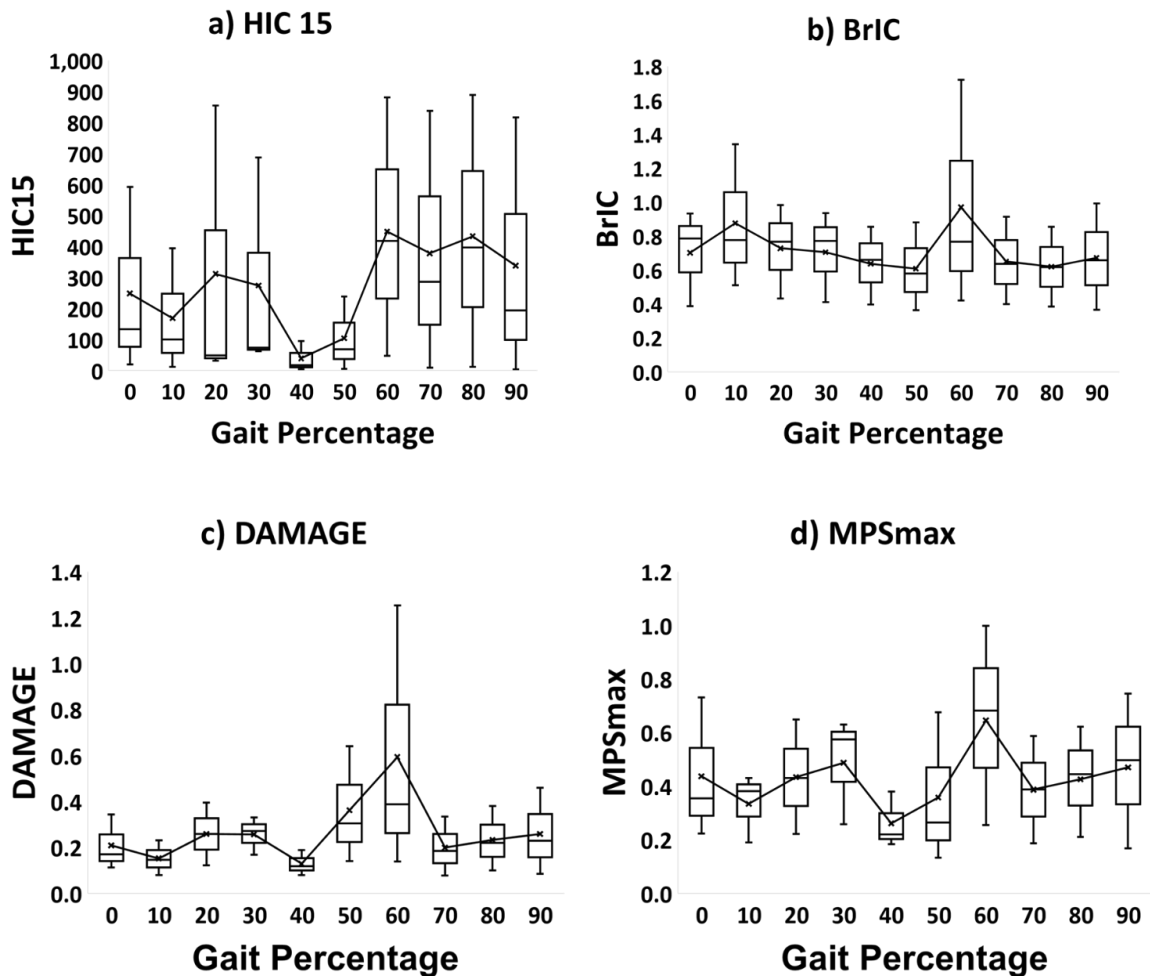
Figure 3-30 Walking gaits a) HIC15 b)BrIC c)DAMAGE d)MPSmax e)MPSmean f) CSDM15







**Figure 3-31 Running gaits a) HIC15 b) BrIC c) DAMAGE d) MPSmax e) MPSmean f) CSDM15**



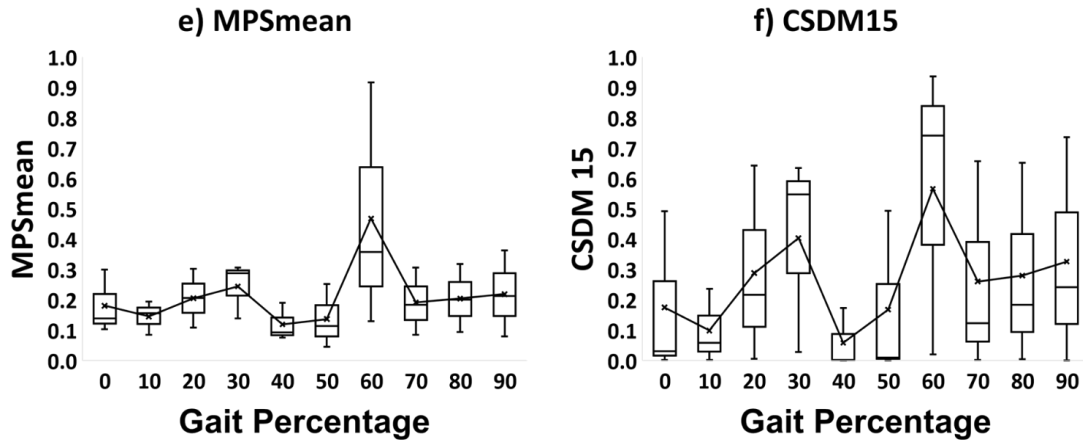


**Figure 3-32 Emergency gaits a) HIC15 b) BrIC c) DAMAGE d) MPSmax e) MPSmean f) CSDM15**

## 3.6 Discussion

### 3.6.1 Scaling and validation of Hybrid III standing FE dummy for pedestrian pre-impact posture study

Due to the numerical complexity of adjusting postures and gaits using human body models, this study uses a partially validated Hybrid III pedestrian dummy. Upon examining the anthropometry of the dummy against literature and ANSUR databases, we found that the original HIII dummy model was shorter than the stature of 50<sup>th</sup> percentile average males. As a result, a global scaling technique (Section 3.3.3) was adopted to scale the height of the dummy.

The head drop test was used to validate the scaled dummy's head acceleration. The scaled dummy's upper-body kinematics in CPC with a mid-size sedan vehicle were validated using seven PMHS test data. As a result of the findings in Section 3.3.4, we determined that the dummy lacks pelvic biofidelity due to the joint properties of the pelvis and upper legs. However, all of the scaled dummy's kinematic trajectories were within the 10% corridor of the cadaver data (Figure 3-25), and the dummy replicated the majority of the PMHS kinematics in CPC using a mid-sized sedan vehicle. Thus, this scaled dummy was justified as acceptable to be used for studying pedestrian posture and gait prior to impact.

One major limitation of using Hybrid III is that the dummy is not designed for pedestrian impacts. Modifications such as at the knee region are needed and have been explored in-house to test various configurations. In the end, it was found that head trajectories predicted by the modified Hybrid III model fell into a reasonable range, and the modified Hybrid III model was used to conveniently investigate various gaits and gait percentages.

### 3.6.2 Effect of pedestrian gaits and posture on head and brain response.

Based on the results from Section 3.5.2, walking and emergency gaits both dominate linear head kinematics, whereas running gaits dominate rotational head kinematics, resulting in increased brain strain. As a result, different head kinematics for different pedestrian gait types were observed. Previous studies have shown that pedestrian stance at the impact significantly influences head rotation [67, 112]. The center of gravity of the pedestrian changes with pedestrian gait serials, thus resulting in different stress point on the pedestrian's head leading to different linear and angular acceleration [116]. Pak et al. revealed that pedestrian pre-impact postures influenced head impact regions and post-impact pedestrian upper body rotation using full-scale the Global Human Body Models Consortium (GHBMC) male (AM50) pedestrian model [14]. Our findings were consistent with theirs. As a result, the risk of head injuries such as diffuse brain injuries is higher in the running gait posture than in the walking and emergency gait postures, which are more vulnerable to head injuries such as skull fractures and focal brain injuries.

The relationship between head kinematics and intracranial brain strains was also investigated. Our findings in Section 3.5.3 show that peak head rotational velocity is more strongly associated with brain strain than peak rotational acceleration during CPC-related head impacts. Though HIC15 scores are not linearly related to strain, they do have a moderate correlation.

Our findings show that the risk of pedestrian head injury varies depending on the gait percentage in the same and different gait types. Previous study has also revealed that pedestrian injury risks differ for gait serials in the same gaits [13]. In walking gaits, the HIC score increases during the stance phase and decreases during the swing phase,

whereas in the running, the HIC score decreases during the stance phase and begins to rise during the swing phase. Due to the symmetry of pedestrian gaits [120], the majority of rotational and strain injury metric values vary cyclically. These detailed characteristics of pedestrian gaits and postures on head dynamic and brain strain response provide a basis for future pedestrian head injury prevention strategies, with pedestrian gaits and posture as a critical parameter in determining the risk of pedestrian head injury.

### 3.7 Conclusion

This study quantified the influence of pedestrian pre-impact gait and posture on head dynamic and brain response of average 50<sup>th</sup> male percentile during CPC with the mid-sedan vehicle. We modified and validated the Hybrid III pedestrian dummy model against the cadaver test for pedestrian pre-impact posture and gait analysis. We found that running pedestrian gaits are susceptible to diffuse brain injuries while walking, and emergency gaits are susceptible to skull fractures and focal brain injuries. Peak rotational velocity correlated strongly with brain strains than peak rotational acceleration. In walking and running gaits, linear head kinematics differs significantly between the stance and swing phases, whereas rotational head kinematics and brain stresses differ cyclically across gait percentages in all three gaits. Head injury risks are different for different gait percentages in the same and different pedestrian gaits. Thus pre-impact pedestrian gait should be an essential factor in studying the pedestrian head injury risks in CPC.

## Chapter 4

### 4 Conclusion and Future Work

#### 4.1 Brief Overview

To mitigate the increasing prevalence of pedestrian TBIs in RTAs, a computational approach was used to quantify the effect of vehicle front shape parameters, and pre-impact pedestrian gait postures on pedestrian TBI risks during CPCs. This concluding chapter summarizes the research's major findings, limitations, novelty, and potential future research directions.

#### 4.2 Summary

##### 4.2.1 Effect of vehicle front shape parameters

The second chapter of this thesis was primarily concerned with investigating the relationship between vehicle shape parameters and TBI risks during vehicle impact among four different pedestrian body sizes. The findings of this chapter provided unique evidence indicating the importance of bonnet leading edge height (BLEH) in concussion risk. The influence of BLEH on mild TBI odds from head-to-windshield impacts in the sedan was different from head-to-hood impacts in high leading edged vehicles. In addition, we observed that vehicles with high BLEH and low bonnet angle (BA) were most susceptible to causing AIS4+ focal and diffuse brain injuries. Furthermore, BLEH and BA influence the effect of pedestrian height and weight on pedestrian head rotation indirectly. As a result, BLEH is a dominant parameter for pedestrian TBI risk, while BA is the second most important parameter, and both should be meticulously optimized in future vehicle design safety for pedestrian head injury protection.

##### 4.2.2 Effect of pedestrian pre-impact gait postures

The third chapter of this thesis investigated the effect of pedestrian pre-impact gait posture on dynamic head response and brain strain during CPCs. Our findings indicate that pedestrian TBI risks varied significantly according to gait postures in both the same and different gait types. Walking and emergency gaits dominate linear head kinematics,

resulting in skull fractures and focal brain injuries. Running gaits dominate pedestrian head rotation, resulting in increased brain strains and diffuse brain injuries. Additionally, head injury severity varies significantly between the stance and swing phases of the walking and running gait postures. These findings revealed the importance of pre-impact gait posture in determining the pedestrian TBI risks during CPC. Thus, pedestrian pre-impact gait posture should be a significant factor when optimizing vehicles' front shapes for pedestrian injury protection.

### 4.3 Limitations

There are several limitations in this thesis.

1. The vehicle impact location was limited to the vehicle centerline and laterally struck by the pedestrian; however, lateral pedestrian impact accounted for more than 80% of cases in GIDAS data [93].
2. The gait posture of the THUMS models was limited to mid-stance walking gait posture. (Chapter 2)
3. Effect of vehicle braking and steering maneuver was not considered in this study
4. There are no venous vessels in the THUMS head model and the brain-skull interface were modelled as shared nodes.
5. Although the THUMS pedestrian model and car model were considered as well-validated (Chapter 2), the THUMS brain model could be further improved by incorporating axonal modeling to better understand diffuse axonal injuries
6. Although the dummy model (Chapter 3) was scaled and verified against cadaveric data, ideally, a model that can better represent knee response or even a human body model are preferred. New techniques such as PIPER that allow human body posture to change are recommended.

## 4.4 Future work, Novelty, and Significance

### 4.4.1 Future work

#### Effect BLEH on mild TBI

Our findings indicate that the BLEH has a significant effect on the risk of mild TBIs during CPCs. A more in-depth analysis of BLEH should be conducted in future studies, taking into account a wide variety of impact scenarios and impact speeds.

#### Shoulder contact force

Previous studies have hypothesized that shoulder contact significantly influences brain strains in collision with high BLEH vehicles [48]. Thus in the future, the relationship between intracranial strain response and shoulder contact force will be investigated in SUV and pickup truck impacts

#### Regional brain strain prediction using a deep learning model

We will develop a deep neural network model that uses 148 CPC reconstruction data to predict regional brain strain values (CSDM and MPS) from head kinematic data, which can replace conventional prescribed head-only FE simulation for brain strain estimation in CPC-related impacts and considerably save computation cost.

#### Posture study with Human body model

Pak et al. used GHBM full-scale HBM and adjusted five different walking gait serials and examined the influence of pedestrian gait posture and vehicle front shape [112]. In future, we will also use the PIPER platform to adjust the gait postures of the THUMS model and conduct pedestrian posture studies.

#### 4.4.2 Novelty and Significance

1. To our knowledge, this is the first study to quantify the influence of pre-impact pedestrian gait postures on head dynamic response and intracranial brain strains in CPC-related impacts. (Chapter 3)
2. Unlike previous studies using multibody models and retrospective analyses of accident data, this study comprehensively quantified the relationship between vehicle front shape parameters and pedestrian TBI risk using four full-scale human body models and four distinct front shapes at three impact speeds. (Chapter 2)
3. This study also assessed the risk of child pedestrians suffering a TBI or a skull fracture in CPC and included impact scenarios involving pickup trucks, which are increasingly common on the road nowadays. (Chapter 2)
4. HIC was primarily used to quantify the relationship between vehicle front structure and pedestrian head injury risk in previous reconstruction studies using multi-body simulations. However, we used a variety of head injury criteria in this study, including kinematic and intracranial tissue level strain-based metrics.



## References

- [1] W. H. Organization, *Global status report on road safety 2015*. World Health Organization, 2015.
- [2] C. Neal-Sturgess, E. Carter, R. Hardy, R. Cuerden, L. Guerra, and J. Yang, "APROSYS European in-depth pedestrian database," *Age*, vol. 91, p. 95, 2007.
- [3] D. Otte, M. Jansch, and C. Haasper, "Injury protection and accident causation parameters for vulnerable road users based on German In-Depth Accident Study GIDAS," *Accident Analysis & Prevention*, vol. 44, no. 1, pp. 149-153, 2012.
- [4] D. Otte, "Severity and mechanism of head impacts in car to pedestrian accidents," in *Proc. Int. IRCOBI Conf. Biomechanics of Impact*, 1999, pp. 329-341.
- [5] J. Yang, "Review of injury biomechanics in car-pedestrian collisions," *International journal of vehicle safety*, vol. 1, no. 1-3, pp. 100-117, 2005.
- [6] K.-U. Schmitt, P. F. Niederer, M. H. Muser, and F. Walz, *Trauma Biomechanics: Accidental injury in traffic and sports*. Springer Science & Business Media, 2009.
- [7] B. Fildes, H. C. Gabler, D. Otte, A. Linder, and L. Sparke, "Pedestrian impact priorities using real-world crash data and harm," in *IRCOBI conference, Graz*, 2004.
- [8] P. H. A. o. Canada, "Injury in review, 2020 edition: spotlight on traumatic brain injuries across the life course," ed: Public Health Agency of Canada, 2020.
- [9] G. Li, M. Lyons, B. Wang, J. Yang, D. Otte, and C. Simms, "The influence of passenger car front shape on pedestrian injury risk observed from German in-depth accident data," *Accident Analysis & Prevention*, vol. 101, pp. 11-21, 2017.
- [10] Y. Peng, C. Deck, J. Yang, and R. Willinger, "Effects of pedestrian gait, vehicle-front geometry and impact velocity on kinematics of adult and child pedestrian head," *International journal of crashworthiness*, vol. 17, no. 5, pp. 553-561, 2012.
- [11] G. Li, J. Yang, and C. Simms, "Safer passenger car front shapes for pedestrians: A computational approach to reduce overall pedestrian injury risk in realistic impact scenarios," *Accident Analysis & Prevention*, vol. 100, pp. 97-110, 2017.
- [12] G. Li, F. Wang, D. Otte, and C. Simms, "Characteristics of pedestrian head injuries observed from real world collision data," *Accident Analysis & Prevention*, vol. 129, pp. 362-366, 2019.
- [13] T. Zou, A. Zha, Q. Liu, and C. Simms, "Pedestrian gaits observed from actual pedestrian-vehicle collisions," *International Journal of Crashworthiness*, pp. 1-23, 2020.

- [14] W. Pak, D. Grindle, and C. Untaroiu, "The Influence of Gait Stance and Vehicle Type on Pedestrian Kinematics and Injury Risk," in *ASME 2020 International Design Engineering Technical Conferences and Computers and Information in Engineering Conference*, 2020: American Society of Mechanical Engineers Digital Collection.
- [15] !!! INVALID CITATION !!! {}.
- [16] R. Retting, "Pedestrian traffic fatalities by state: 2019 preliminary data," 2020.
- [17] C. Huipeng, F. Lianxue, and Z. Heyue, "A comparative study between China and IHRA for the vehicle-pedestrian impact," *SAE International Journal of Passenger Cars-Mechanical Systems*, vol. 2, no. 2009-01-1205, pp. 1108-1115, 2009.
- [18] G. Li, D. Otte, J. Yang, and C. Simms, "Pedestrian injury trends evaluated by comparison of the PCDS and GIDAS databases," in *Proc. Int. Research Council on Biomechanics of Injury (IRCOBI) Conf., Seoul, Korea*, 2016.
- [19] C. Simms and D. Wood, *Pedestrian and cyclist impact: a biomechanical perspective*. Springer Science & Business Media, 2009.
- [20] H. Chelly *et al.*, "Clinical characteristics and prognosis of traumatic head injury following road traffic accidents admitted in ICU "analysis of 694 cases"," *European journal of trauma and emergency surgery*, vol. 45, no. 2, pp. 245-253, 2019.
- [21] J. Dunne *et al.*, "The epidemiology of traumatic brain injury due to traffic accidents in Latin America: a narrative review," *Journal of neurosciences in rural practice*, vol. 11, no. 02, pp. 287-290, 2020.
- [22] A. Kumar, S. Lalwani, D. Agrawal, R. Rautji, and T. Dogra, "Fatal road traffic accidents and their relationship with head injuries: An epidemiological survey of five years," *Indian journal of neurotrauma*, vol. 5, no. 02, pp. 63-67, 2008.
- [23] M. Majdan *et al.*, "Traumatic brain injuries caused by traffic accidents in five European countries: outcome and public health consequences," *The European Journal of Public Health*, vol. 23, no. 4, pp. 682-687, 2013.
- [24] T. Gennarelli, "Comparsion of Translational and Rotational Motions in Experimental Cerebral Concussion," in *the 15th Stapp Car Crash Conference*, 1971.
- [25] T. A. Gennarelli, L. Thibault, and A. Ommaya, "Pathophysiologic responses to rotational and translational accelerations of the head," in *Proceedings: Stapp Car Crash Conference*, 1972, vol. 16: Society of Automotive Engineers SAE.
- [26] T. A. Gennarelli, L. E. Thibault, J. H. Adams, D. I. Graham, C. J. Thompson, and R. P. Marcincin, "Diffuse axonal injury and traumatic coma in the primate," *Annals*

*of Neurology: Official Journal of the American Neurological Association and the Child Neurology Society*, vol. 12, no. 6, pp. 564-574, 1982.

- [27] S. S. Margulies, L. E. Thibault, and T. A. Gennarelli, "Physical model simulations of brain injury in the primate," *Journal of biomechanics*, vol. 23, no. 8, pp. 823-836, 1990.
- [28] A. K. Ommaya and T. Gennarelli, "Cerebral concussion and traumatic unconsciousness: correlation of experimental and clinical observations on blunt head injuries," *Brain*, vol. 97, no. 4, pp. 633-654, 1974.
- [29] B. Yang *et al.*, "Development of a finite element head model for the study of impact head injury," *BioMed research international*, vol. 2014, 2014.
- [30] J. S. Ruan, T. B. Khalil, and A. I. King, "Finite element modeling of direct head impact," SAE Technical Paper, 0148-7191, 1993.
- [31] C. Zhou, T. B. Khalil, and A. I. King, "A new model comparing impact responses of the homogeneous and inhomogeneous human brain," *SAE transactions*, pp. 2999-3015, 1995.
- [32] H. Mao, H. Gao, L. Cao, V. V. Genthikatti, and K. H. Yang, "Development of high-quality hexahedral human brain meshes using feature-based multi-block approach," *Computer methods in biomechanics and biomedical engineering*, vol. 16, no. 3, pp. 271-279, 2013.
- [33] H. Mao *et al.*, "Development of a finite element human head model partially validated with thirty five experimental cases," *Journal of biomechanical engineering*, vol. 135, no. 11, p. 111002, 2013.
- [34] E. G. Takhounts, R. H. Eppinger, J. Q. Campbell, R. E. Tannous, E. D. Power, and L. S. Shook, "On the development of the SIMon finite element head model," SAE Technical Paper, 2003.
- [35] T. J. Horgan and M. D. Gilchrist, "The creation of three-dimensional finite element models for simulating head impact biomechanics," *International Journal of Crashworthiness*, vol. 8, no. 4, pp. 353-366, 2003.
- [36] S. Kleiven and H. von Holst, "Consequences of head size following trauma to the human head," *Journal of biomechanics*, vol. 35, no. 2, pp. 153-160, 2002.
- [37] S. Ji, W. Zhao, Z. Li, and T. W. McAllister, "Head impact accelerations for brain strain-related responses in contact sports: a model-based investigation," *Biomechanics and modeling in mechanobiology*, vol. 13, no. 5, pp. 1121-1136, 2014.

- [38] H. Lissner, M. Lebow, and F. Evans, "Experimental studies on the relation between acceleration and intracranial pressure changes in man," *Surgery, gynecology & obstetrics*, vol. 111, pp. 329-338, 1960.
- [39] E. Gurdjian, A. Ostrowski, W. Hardy, D. Lindner, and L. Thomas, "Results of operative treatment of protruded and ruptured lumbar discs: based on 1176 operative cases with 82 per cent follow-up of 3 to 13 years," *Journal of neurosurgery*, vol. 18, no. 6, pp. 783-791, 1961.
- [40] C. W. Gadd, "Use of a weighted-impulse criterion for estimating injury hazard," SAE technical paper, 0148-7191, 1966.
- [41] E. Lewis, "Head injury and protection," *Ernsting's aviation medicine. Boca Ratoa, FL: CRC Press, Taylor & Francis Groupo*, pp. 179-88, 2006.
- [42] A. Bartsch, E. Benzel, V. Miele, and V. Prakash, "Impact test comparisons of 20th and 21st century American football helmets," *Journal of neurosurgery*, vol. 116, no. 1, pp. 222-233, 2012.
- [43] A. McLean and R. W. Anderson, "Biomechanics of closed head injury," *Head injury*, pp. 25-37, 1997.
- [44] J. Versace, "A review of the severity index," 1971.
- [45] M. Kleinberger, E. Sun, R. Eppinger, S. Kuppa, and R. Saul, "Development of improved injury criteria for the assessment of advanced automotive restraint systems," *NHTSA Docket*, vol. 4405, no. 9, pp. 12-17, 1998.
- [46] L. Zhang, K. Yang, and A. King, "A Proposed Injury Threshold for Mild Traumatic Brain Injury," *Journal of biomechanical engineering*, vol. 126, pp. 226-36, 05/01 2004, doi: 10.1115/1.1691446.
- [47] J. A. Newman, "A generalized acceleration model for brain injury threshold (GAMBIT)," in *Proceedings of International IRCOBI Conference, 1986*, 1986.
- [48] E. G. Takhounts, M. J. Craig, K. Moorhouse, J. McFadden, and V. Hasija, "Development of brain injury criteria (BrIC)," SAE Technical Paper, 2013.
- [49] E. Lee, A. Shrivatri, and S. Ohara, "NHTSA Oblique Test Data Analysis Method by LS-DYNA Modeling," 2020.
- [50] J. A. Newman and N. Shewchenko, "A proposed new biomechanical head injury assessment function-the maximum power index," SAE Technical Paper, 2000.
- [51] R. M. Greenwald, J. T. Gwin, J. J. Chu, and J. J. Crisco, "Head impact severity measures for evaluating mild traumatic brain injury risk exposure," *Neurosurgery*, vol. 62, no. 4, pp. 789-798, 2008.

- [52] E. J. Sanchez *et al.*, "Evaluation of head and brain injury risk functions using sub-injurious human volunteer data," *Journal of neurotrauma*, vol. 34, no. 16, pp. 2410-2424, 2017.
- [53] E. G. Takhounts *et al.*, "Investigation of traumatic brain injuries using the next generation of simulated injury monitor (SIMon) finite element head model," *Stapp car crash journal*, vol. 52, p. 1, 2008.
- [54] L. F. Gabler, J. R. Crandall, and M. B. Panzer, "Development of a metric for predicting brain strain responses using head kinematics," *Annals of biomedical engineering*, vol. 46, no. 7, pp. 972-985, 2018.
- [55] L. F. Gabler, J. R. Crandall, and M. B. Panzer, "Development of a second-order system for rapid estimation of maximum brain strain," *Annals of biomedical engineering*, vol. 47, no. 9, pp. 1971-1981, 2019.
- [56] S. S. Margulies and L. E. Thibault, "A proposed tolerance criterion for diffuse axonal injury in man," *Journal of biomechanics*, vol. 25, no. 8, pp. 917-923, 1992.
- [57] J. Yao, J. Yang, and D. Otte, "Investigation of head injuries by reconstructions of real-world vehicle-versus-adult-pedestrian accidents," *Safety science*, vol. 46, no. 7, pp. 1103-1114, 2008.
- [58] T. A. Gennarelli and E. Wodzin, "The abbreviated injury scale 2005," *Update*, vol. 20082008, 2008.
- [59] J. D. States, "The abbreviated and the comprehensive research injury scales," *SAE Transactions*, pp. 2625-2634, 1969.
- [60] K. L. Loftis, J. Price, and P. J. Gillich, "Evolution of the abbreviated injury scale: 1990–2015," *Traffic injury prevention*, vol. 19, no. sup2, pp. S109-S113, 2018.
- [61] S. T. Dawodu, "Traumatic Brain Injury: Definition, Epidemiology, Pathophysiology.," vol. Retrieved 1st March 2011, ed, 2003
- [62] C. Arregui-Dalmases, F. J. Lopez-Valdes, and M. Segui-Gomez, "Pedestrian injuries in eight European countries: an analysis of hospital discharge data," *Accident Analysis & Prevention*, vol. 42, no. 4, pp. 1164-1171, 2010.
- [63] R. Watanabe, H. Miyazaki, Y. Kitagawa, and T. Yasuki, "Research of collision speed dependency of pedestrian head and chest injuries using human FE model (THUMS version 4)," in *22nd international technical conference on the enhanced safety of vehicles (ESV)*, WA, 2011, pp. 11-0043.

- [64] B. S. Roudsari, C. N. Mock, and R. Kaufman, "An evaluation of the association between vehicle type and the source and severity of pedestrian injuries," *Traffic injury prevention*, vol. 6, no. 2, pp. 185-192, 2005.
- [65] R. Kendall, M. Meissner, and J. Crandall, "The causes of head injury in vehicle-pedestrian impacts: comparing the relative danger of vehicle and road surface," SAE Technical paper, 0148-7191, 2006.
- [66] J. Yao, J. Yang, and D. Otte, "Head injuries in child pedestrian accidents—in-depth case analysis and reconstructions," *Traffic Injury Prevention*, vol. 8, no. 1, pp. 94-100, 2007.
- [67] C. K. Simms and D. P. Wood, "Effects of pre-impact pedestrian position and motion on kinematics and injuries from vehicle and ground contact," *International Journal of Crashworthiness*, vol. 11, no. 4, pp. 345-355, 2006.
- [68] A. Badea-Romero and J. Lenard, "Source of head injury for pedestrians and pedal cyclists: Striking vehicle or road?," *Accident Analysis & Prevention*, vol. 50, pp. 1140-1150, 2013.
- [69] N. Andelic, S. Sigurdardottir, C. Brunborg, and C. Roe, "Incidence of hospital-treated traumatic brain injury in the Oslo population," *Neuroepidemiology*, vol. 30, no. 2, pp. 120-128, 2008.
- [70] G. Bauzá, W. W. LaMorte, P. A. Burke, and E. F. Hirsch, "High mortality in elderly drivers is associated with distinct injury patterns: analysis of 187,869 injured drivers," *Journal of Trauma and Acute Care Surgery*, vol. 64, no. 2, pp. 304-310, 2008.
- [71] A. Mallory, "Head injury and aging: the importance of bleeding injuries," in *Annals of Advances in Automotive Medicine/Annual Scientific Conference*, 2010, vol. 54: Association for the Advancement of Automotive Medicine, p. 51.
- [72] D. Richards and J. Carroll, "Relationship between types of head injury and age of pedestrian," *Accident Analysis & Prevention*, vol. 47, pp. 16-23, 2012.
- [73] R. C. Harruff, A. Avery, and A. S. Alter-Pandya, "Analysis of circumstances and injuries in 217 pedestrian traffic fatalities," *Accident Analysis & Prevention*, vol. 30, no. 1, pp. 11-20, 1998.
- [74] C. D. Smith, H. Chebrolu, D. R. Wekstein, F. A. Schmitt, and W. R. Markesbery, "Age and gender effects on human brain anatomy: a voxel-based morphometric study in healthy elderly," *Neurobiology of aging*, vol. 28, no. 7, pp. 1075-1087, 2007.
- [75] D. Viano, H. von Holst, and E. Gordon, "Serious brain injury from traffic-related causes: priorities for primary prevention," *Accident Analysis & Prevention*, vol. 29, no. 6, pp. 811-816, 1997.

- [76] L. Zhen, "Study on the method of vehicle speed calculation in pedestrian-vehicle crash," *Chengdu, China: Xihua University*, 2016.
- [77] W. Liu, S. Su, J. Qiu, Y. Zhang, and Z. Yin, "Exploration of pedestrian head injuries—collision parameter relationships through a combination of retrospective analysis and finite element method," *International journal of environmental research and public health*, vol. 13, no. 12, p. 1250, 2016.
- [78] S. Liangliang, H. Yong, B. Bingyu, H. Hongwu, Z. Dayong, and Y. Zhen, "Analysis of Vehicle Front-end Structure Parameters Based on Pedestrian Landing Impacts," *Journal of Hunan University Natural Sciences*, vol. 46, no. 2, 2019.
- [79] K. Ito, M. Tokuyama, H. Miyazaki, S. Hayashi, Y. Kitagawa, and T. Yasuki, "Development of child finite element (FE) models and vehicle-to-pedestrian collision simulations," in *25th International Technical Conference on the Enhanced Safety of Vehicles (ESV)*, Detroit Michigan, United State, 2017, pp. 6-5.
- [80] Y. Han, J. Yang, K. Mizuno, and Y. Matsui, "Effects of vehicle impact velocity, vehicle front-end shapes on pedestrian injury risk," *Traffic injury prevention*, vol. 13, no. 5, pp. 507-518, 2012.
- [81] R. Fredriksson, L. Zhang, O. Boström, and K. Yang, "Influence of impact speed on head and brain injury outcome in vulnerable road user impacts to the car hood," SAE Technical Paper, 2007.
- [82] D. Longhitano, B. Henary, K. Bhalla, J. Ivarsson, and J. Crandall, "Influence of vehicle body type on pedestrian injury distribution," *SAE transactions*, pp. 2283-2288, 2005.
- [83] J. Kerrigan, C. Arregui, and J. Crandall, "Pedestrian head impact dynamics: comparison of dummy and PMHS in small sedan and large SUV impacts," in *21st international conference on the enhanced safety of vehicles (ESV)*, 2009, no. 09-0127.
- [84] S. Shang, D. Otte, G. Li, and C. Simms, "Detailed assessment of pedestrian ground contact injuries observed from in-depth accident data," *Accident Analysis & Prevention*, vol. 110, pp. 9-17, 2018.
- [85] R. Watanabe, T. Katsuhara, H. Miyazaki, Y. Kitagawa, and T. Yasuki, "Research of the relationship of pedestrian injury to collision speed, car-type, impact location and pedestrian sizes using human FE model (THUMS Version 4)," SAE Technical Paper, 2012.
- [86] M. F. Ballesteros, P. C. Dischinger, and P. Langenberg, "Pedestrian injuries and vehicle type in Maryland, 1995–1999," *Accident Analysis & Prevention*, vol. 36, no. 1, pp. 73-81, 2004.

- [87] C. DiMaggio, M. Durkin, and L. D. Richardson, "The association of light trucks and vans with paediatric pedestrian deaths," *International journal of injury control and safety promotion*, vol. 13, no. 2, pp. 95-99, 2006.
- [88] B. Y. Henary, J. Crandall, K. Bhalla, C. N. Mock, and B. S. Roudsari, "Child and adult pedestrian impact: the influence of vehicle type on injury severity," in *Annual Proceedings/Association for the Advancement of Automotive Medicine*, 2003, vol. 47: Association for the Advancement of Automotive Medicine, p. 105.
- [89] D. Longhitano, J. Ivarsson, B. Henary, and J. Crandall, "Torso injury trends for pedestrians struck by cars and LTVs," in *Experimental Safety Vehicles Conference*, 2005, pp. 107-109.
- [90] L. J. Paulozzi, "United States pedestrian fatality rates by vehicle type," *Injury prevention*, vol. 11, no. 4, pp. 232-236, 2005.
- [91] D. Otte, "Influence of the fronthood length for the safety of pedestrians in car accidents and demands to the safety of small vehicles," *SAE transactions*, pp. 1923-1933, 1994.
- [92] C. Klug, F. Feist, B. Schneider, W. Sinz, J. Ellway, and M. van Ratingen, "Development Of A Certification Procedure For Numerical Pedestrian Models," in *26th International Technical Conference on the Enhanced Safety of Vehicles (ESV): Technology: Enabling a Safer Tomorrow National Highway Traffic Safety Administration*, 2019, no. 19-0310.
- [93] H. Li *et al.*, "Validation of a finite element model with six-year-old child anatomical characteristics as specified in Euro NCAP Pedestrian Human Model Certification (TB024)," *Computer Methods in Biomechanics and Biomedical Engineering*, pp. 1-15, 2020.
- [94] D. Marzougui, R. Samaha, C. Cui, and C. Kan, "Development & Validation of a Finite Element Model for the 2010 Toyota Yaris Passenger Sedan. prepared for FHWA," NCAC, 2011.
- [95] N. 2008-T-004, "NCAC, "Development and Validation of a Finite Element Model for a 2002 Ford Explorer"," ed, Dec 2008.
- [96] D. Marzougui, D. Brown, H. Park, C. Kan, and K. Opiela, "Development & Validation of a Finite Element Model for a Mid-Sized Passenger Sedan," in *Proceedings of the 13th international LS-DYNA users conference, Dearborn, MI, USA*, 2014, pp. 8-10.
- [97] E. E. V.-s. Committee, "Improved test methods to evaluate pedestrian protection afforded by passenger cars," *EEVC Working Group 17 Report*, 1998.



- [98] K. Wachirut, C. Julaluk, and C. Sujeepapha, "FINITE ELEMENT STUDY OF EFFECTIVENESS OF MODIFIED FRONT-END STRUCTURE WITH ALUMINIUM FOAM IN REDUCING PEDESTRIAN INJURY."
- [99] R. Reichert, P. Mohan, D. Marzougui, C.-D. Kan, and D. Brown, "Validation of a toyota camry finite element model for multiple impact configurations," SAE Technical Paper, 0148-7191, 2016.
- [100] "EuroNCAP Pedestrian Testing Protocol Version 9.0.2," ed, 2018.
- [101] C. Normalisation, "Head and neck impact, burn and noise injury criteria—a guide for cen helmet standards committees. CEN," TR 16148. Comite Europeen de Normalisation, 2011.
- [102] B. Chinn *et al.*, "COST 327 Motorcycle safety helmets," *European Commission, Directorate General for Energy and Transport*, 2001.
- [103] L.-B. Cao, Z. Zhou, B.-H. Jiang, and G. Zhang, "Development and validation of the FE model for a 10-year-old child head," *Chin J Biomed Eng*, vol. 33, no. 1, pp. 63-70, 2014.
- [104] J. H. McElhaney, J. L. Fogle, J. W. Melvin, R. R. Haynes, V. L. Roberts, and N. M. Alem, "Mechanical properties of cranial bone," *Journal of biomechanics*, vol. 3, no. 5, pp. 495-511, 1970.
- [105] J. Liu, Z. Feng, and H. Chen, "Simulation research on pedestrian injury severity in traffic accident of human-vehicle collisions," *Road Traff Technol*, vol. 11, pp. 1-4, 2012.
- [106] C. K. Simms and D. P. Wood, "Pedestrian risk from cars and sport utility vehicles—a comparative analytical study," *Proceedings of the Institution of Mechanical Engineers, Part D: Journal of automobile engineering*, vol. 220, no. 8, pp. 1085-1100, 2006.
- [107] R. W. Anderson and S. Doecke, "An analysis of head impact severity in simulations of collisions between pedestrians and SUVs/work utility vehicles, and sedans," *Traffic injury prevention*, vol. 12, no. 4, pp. 388-397, 2011.
- [108] P. Hoekstra, "Bicycle and light-powered two-wheeler accidents-report of eevc-wg8," in *Proceedings of the International Research Council on the Biomechanics of Injury conference*, 1984, vol. 12: International Research Council on Biomechanics of Injury, pp. 23-36.
- [109] J.-W. Lee, K.-H. Yoon, Y.-S. Kang, and G.-J. Park, "Vehicle hood and bumper structure design to mitigate casualties of pedestrian accidents," *SAE paper*, no. 05-0105, 2004.

- [110] C. Kerkeling, J. Schäfer, and G.-M. Thompson, "Structural hood and hinge concepts for pedestrian protection," in *Proc. 17th Int. Tech. Conf. ESV*, 2005, pp. 4-7.
- [111] L. Ren, D. Wang, X. Liu, H. Yu, C. Jiang, and Y. Hu, "Influence of skull fracture on traumatic brain injury risk induced by blunt impact," *International journal of environmental research and public health*, vol. 17, no. 7, p. 2392, 2020.
- [112] D. P. Wood, C. Simms, and D. Walsh, "Vehicle-pedestrian collisions: Validated models for pedestrian impact and projection," *Proceedings of the Institution of Mechanical Engineers, Part D: Journal of Automobile Engineering*, vol. 219, no. 2, pp. 183-195, 2005.
- [113] J. Yao, J. Yang, and R. Fredriksson, "Reconstruction of head-to-hood impact in an automobile-to-child-pedestrian collision," *International journal of crashworthiness*, vol. 11, no. 4, pp. 387-395, 2006.
- [114] R. Anderson, A. McLean, and Y. Dokko, "Determining accurate contact definitions in multi-body simulations for DOE-type reconstruction of head impacts in pedestrian accidents," in *Proc. 19th International Conference on the Enhanced Safety of Vehicles, Paper*, 2005, pp. 05-0175.
- [115] L. Li, X. Yang, and L. Yin, "Exploration of pedestrian refuge effect on safety crossing at signalized intersection," *Transportation research record*, vol. 2193, no. 1, pp. 44-50, 2010.
- [116] Y. Peng, Y. Chen, J. Yang, D. Otte, and R. Willinger, "A study of pedestrian and bicyclist exposure to head injury in passenger car collisions based on accident data and simulations," *Safety science*, vol. 50, no. 9, pp. 1749-1759, 2012.
- [117] J. Elliott, C. K. Simms, and D. P. Wood, "Pedestrian head translation, rotation and impact velocity: The influence of vehicle speed, pedestrian speed and pedestrian gait," *Accident Analysis & Prevention*, vol. 45, pp. 342-353, 2012.
- [118] G. Li, J. Yang, and C. Simms, "The influence of gait stance on pedestrian lower limb injury risk," *Accident Analysis & Prevention*, vol. 85, pp. 83-92, 2015.
- [119] G. Crocetta, S. Piantini, M. Pierini, and C. Simms, "The influence of vehicle front-end design on pedestrian ground impact," *Accident Analysis & Prevention*, vol. 79, pp. 56-69, 2015.
- [120] C. D. Untaroiu, M. U. Meissner, J. R. Crandall, Y. Takahashi, M. Okamoto, and O. Ito, "Crash reconstruction of pedestrian accidents using optimization techniques," *International Journal of Impact Engineering*, vol. 36, no. 2, pp. 210-219, 2009.
- [121] C. D. Untaroiu, J. R. Crandall, Y. Takahashi, M. Okamoto, O. Ito, and R. Fredriksson, "Analysis of running child pedestrians impacted by a vehicle using

- rigid-body models and optimization techniques," *Safety science*, vol. 48, no. 2, pp. 259-267, 2010.
- [122] P. Mohan *et al.*, "LSTC/NCAC dummy model development," in *11th International LS-Dyna Users Conference*, 2010.
- [123] C. Maurath and S. Guha, "Updates to LSTC's LS-DYNA® Anthropomorphic Models," in *12th International LS-DYNA Users Conference*, 2012.
- [124] C. C. Gordon, "1988 Anthropometric survey of US army personnel: methods and summary statistics," *Technical Report Natick/TR-89/044*, 1989.
- [125] C. C. Gordon *et al.*, "2012 anthropometric survey of us army personnel: Methods and summary statistics," Army Natick Soldier Research Development and Engineering Center MA, 2014.
- [126] C. D. Untaroiu *et al.*, "A study of the pedestrian impact kinematics using finite element dummy models: the corridors and dimensional analysis scaling of upper-body trajectories," *International journal of crashworthiness*, vol. 13, no. 5, pp. 469-478, 2008.
- [127] J. Shin *et al.*, "Development and validation of a finite element model for the Polar-II upper body," SAE Technical Paper, 0148-7191, 2006.
- [128] T.-C. Chen, J. D. Parker, J. Clark, H.-C. Shin, J. R. Rammon, and V. L. Burt, "National health and nutrition examination survey: estimation procedures, 2011–2014," 2018.
- [129] L. B. Mirel *et al.*, "National Health and Nutrition Examination Survey: estimation procedures, 2007-2010," *Vital and health statistics. Series 2, Data evaluation and methods research*, no. 159, pp. 1-17, 2013.
- [130] M. P. Reed, "Development of anthropometric specifications for the warrior injury assessment manikin (WIAMan)," University of Michigan, Ann Arbor, Transportation Research Institute, 2013.
- [131] I. Kaleps, R. P. White Jr, R. M. Beecher, J. Whitestone, and L. A. Obergefell, "Measurement of Hybrid III dummy properties and analytical simulation data base development," HARRY G ARMSTRONG AEROSPACE MEDICAL RESEARCH LAB WRIGHT-PATTERSON AFB OH, 1988.
- [132] A. H. LY and T. D. HOANG, "Scaling the 50th Percentile Hybrid III dummy model to the height and the weight of a typical Vietnamese."
- [133] H. L. Langhaar, "Dimensional analysis and theory of models," 1962.

- [134] B. J. Ivarsson, J. R. Crandall, D. Longhitano, and M. Okamoto, "Lateral injury criteria for the 6-year-old pedestrian-part II: criteria for the upper and lower extremities," SAE Technical Paper, 0148-7191, 2004.
- [135] H. J. Mertz, "Injury risk assessments based on dummy responses," in *Accidental Injury*: Springer, 2002, pp. 89-102.
- [136] H. J. Mertz and A. L. Irwin, "Anthropomorphic test devices and injury risk assessments," in *Accidental Injury*: Springer, 2015, pp. 83-112.
- [137] J. R. Kerrigan, J. R. Crandall, and B. Deng, "Pedestrian kinematic response to mid-sized vehicle impact," *International journal of vehicle safety*, vol. 2, no. 3, pp. 221-240, 2007.
- [138] V. Kothari and M. Gangal, "Assessment of frictional properties of some woven fabrics," 1994.
- [139] A. M. Nahum, R. Smith, and C. C. Ward, "Intracranial pressure dynamics during head impact," SAE Technical Paper, 0148-7191, 1977.
- [140] N. Yoganandan *et al.*, "Biomechanics of skull fracture," *Journal of neurotrauma*, vol. 12, no. 4, pp. 659-668, 1995.
- [141] W. N. Hardy, C. D. Foster, M. J. Mason, K. H. Yang, A. I. King, and S. Tashman, "Investigation of head injury mechanisms using neutral density technology and high-speed biplanar X-ray," *Stapp car crash journal*, vol. 45, pp. 337-368, 2001.
- [142] J. R. Kerrigan, D. B. Murphy, D. C. Drinkwater, C. Y. Kam, D. Bose, and J. R. Crandall, "Kinematic corridors for PMHS tested in full-scale pedestrian impact tests," in *Experimental Safety Vehicles Conference*, 2005.
- [143] J. Kerrigan *et al.*, "Kinematic comparison of the Polar-II and PMHS in pedestrian impact tests with a sport-utility vehicle," *Proceedings of the 2005 International Research Council on the Biomechanics of Impact (IRCOBI), Prague, Czech Republic*, 2005.

## Curriculum Vitae

**Name:** Thava Kalishwara Kumar Gunasekaran

**Post-secondary Education and** SASTRA University  
Tanjore, India

**Degrees:** 2013-2017 B.Tech Mechanical Engineering

The University of Western Ontario  
London, Ontario, Canada  
2019-2021 M.E.Sc.

**Related Work Experience** Teaching Assistant  
The University of Western Ontario  
2020-2021

Research Assistant  
The University of Western Ontario  
2020-2021

CAE Software Engineer  
Future CAE Technologies (UK) Limited  
2017 -2018

### **Publications:**

1. Weng Y, Bian K, Gunasekaran K, Gholipour J, Vidal C and Mao H. 2021. Small Remotely Piloted Aircraft System to Head Impact – Computational Model Development and Head Response Analysis. Journal of Biomechanics. BM-D-21-00435. Under review.
2. Weng Y, Gunasekaran K, Bian, Ruella C, Spanos M, Vidal C and Mao H. 2020. Investigating Head Injury Criteria and Gender Difference during Small Unmanned Aircraft to Human Collision. 2020. Biomedical Engineering Society. Online poster presentation.
3. Vivek CM, Aravind S, Gunasekaran K, Vignesh H May 2016 Enhancement Of Mechanical Properties Of 16mncr5 Low Alloy Steel Through Carbonitriding Process. International Journal of Science and Innovative Engineering & Technology. May 2016 Issue Volume 1